Advances in Condensed Matter Physics

Active Metamaterials and Metadevices: Enabling Functionalities with Novel Strategies and Materials

Lead Guest Editor: Shuyuan Xiao
Guest Editors: Arash Ahmadivand, Jinbo Pang, and Shengxuan Xia

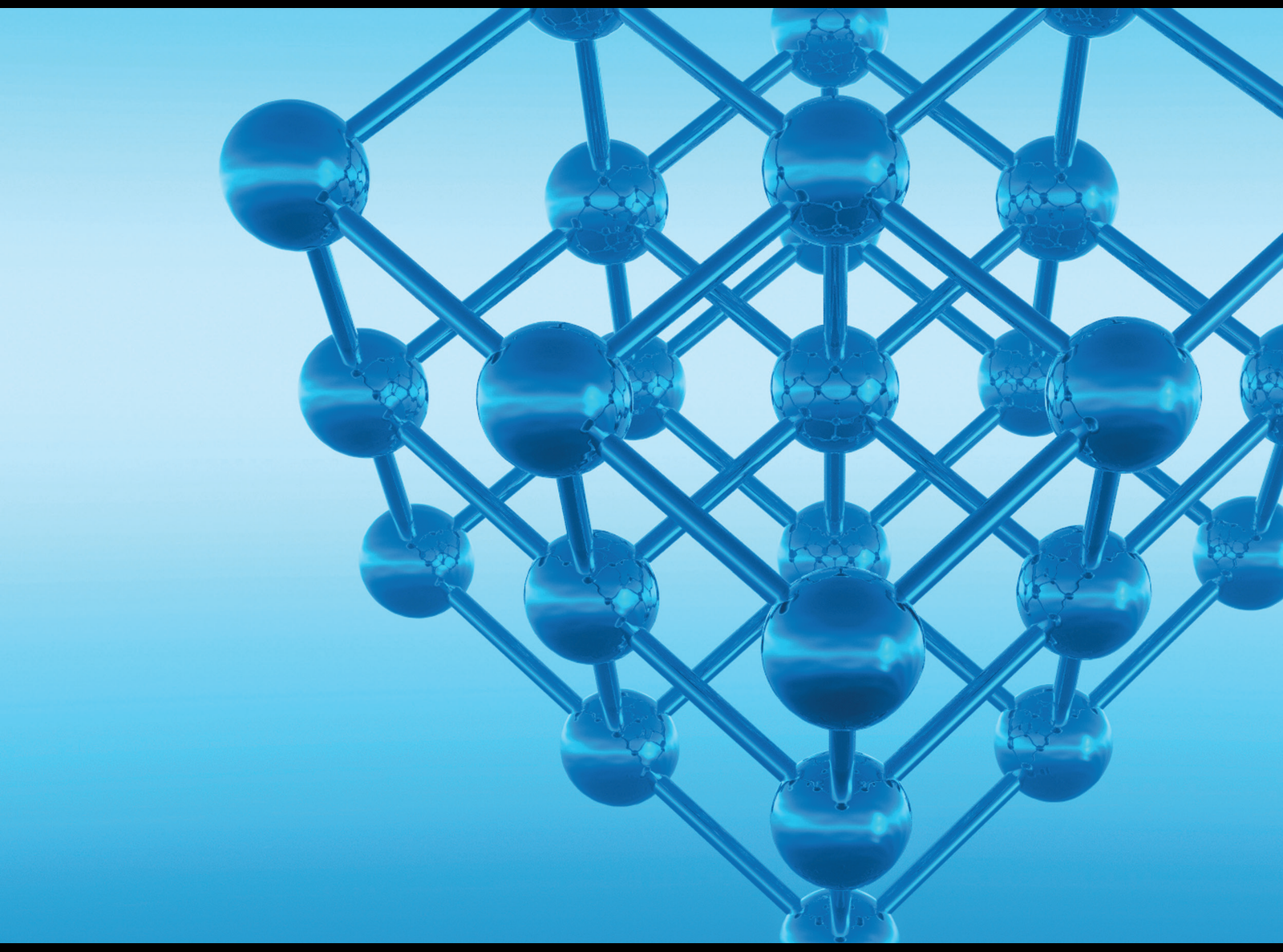

Active Metamaterials and Metadevices: Enabling Functionalities with Novel Strategies and Materials

Advances in Condensed Matter Physics

Active Metamaterials and Metadevices: Enabling Functionalities with Novel Strategies and Materials

Lead Guest Editor: Shuyuan Xiao
Guest Editors: Arash Ahmadivand, Jinbo Pang, and Shengxuan Xia

Contents

Hindawi
Advances in Condensed Matter Physics
Volume 2022, Article ID 5885992, 7 pages
https://doi.org/10.1155/2022/5885992

Research Article

AlGaN/GaN Heterostructure Schottky Barrier Diodes with Graded Barrier Layer

Honghui Liu,[1] **Zhiwen Liang**,[1] **Chaokun Yan**,[1] **Yuebo Liu**,[2] **Fengge Wang**,[1] **Yanyan Xu**,[1] **Junyu Shen**,[1] **Zhengwen Xiao**,[1] **Zhisheng Wu**,[1] **Yang Liu**,[1] **Qi Wang**,[3] **Xinqiang Wang**,[3,4] **and Baijun Zhang**[1]

[1]*State Key Laboratory of Optoelectronic Materials and Technologies, School of Electronics and Information Technology, Sun Yat-Sen University, Guangzhou 510275, China*
[2]*Science and Technology on Reliability Physics and Application of Electronic Component Laboratory, China Electronic Product Reliability and Environmental Testing Research Institute, Guangzhou 510640, China*
[3]*Dongguan Institue of Opto-Electronics, Peking University, Dongguan 523808, China*
[4]*State Key Laboratory for Mesoscopic Physics and Frontiers Science Center for Nano-Optoelectronics, School of Physics, Peking University, Beijing 100871, China*

Correspondence should be addressed to Baijun Zhang; zhbaij@mail.sysu.edu.cn

Received 29 August 2021; Accepted 21 March 2022; Published 6 April 2022

Academic Editor: Maheswar Nayak

The AlGaN/GaN Schottky barrier diodes (SBDs) working as high-power mixer and multiplier show great potential in millimeter wave (MMW) field owing to their high breakdown voltage. Nevertheless, its further application is severely limited by large reverse leakage current (J_r) since the two-dimensional electron gas (2DEG) channel is hard to be pinched off at low voltage. To address this limitation, a graded AlGaN/GaN heterostructure is introduced to extend the 2DEG channel into a quasi-three-dimensional electron slab. By comparing the fixed Al composition AlGaN/GaN SBD, J_r of the graded AlGaN/GaN SBD is significantly reduced due to the extension of channel carriers, confirming the effective J_r suppression effect of this structure. Furthermore, on this basis, a recessed anode structure is utilized to expect a smaller J_r. The results indicated that the graded AlGaN/GaN SBDs with air-bridge structure have achieved a pretty low J_r value (1.6×10^{-13} A at -15 V), and its cutoff frequency is as high as 60.6 GHz. It is expected that such SBDs with low J_r have significant advantages in future applications.

1. Introduction

The Schottky barrier diodes (SBDs) can be used as mixer and multiplier elements in millimeter wave (MMW) imaging [1, 2], nondestructive testing [3], automotive sensors [4, 5], and communication [6] regions due to their nonlinear effect and mature manufacturing technology [7–11]. To date, the planar GaAs-based SBD is still the most commonly used element, but it always exhibits large reverse leakage currents (J_r) and low breakdown voltage, which seriously limits its applications in the high-power field [9]. By contrast, GaN-based SBDs have a higher breakdown voltage and show greater application advantages in the MMW field. Specifically, some researchers have achieved high breakdown voltage and high cutoff frequency (f_c) with the n^--GaN/n^+-GaN structure [12, 13]. In our previous studies, we also have reported the breakdown voltage of -20 V at 0.1 μA and a f_c of 114 GHz based on AlGaN/GaN heterostructure [14]. Compared to bulk doping, the two-dimensional electron gas (2DEG) with high electron mobility and high carrier concentration can be acquired at AlGaN/GaN interface due to its spontaneous polarization and piezoelectric polarization [15–17]. However, according to related reports, the SBDs based on the AlGaN/GaN heterostructure exhibit large J_r because the 2DEG channel is hard to be pinched off at low voltage [18–21]. To solve this problem, an extended 2DEG structure was designed by the graded AlGaN/GaN heterostructure [22–25]. The graded AlGaN/GaN exhibits high

mobility compared with bulk doping due to the removal of ionized impurity scattering, especially in low-temperature environments [22]. Furthermore, the graded AlGaN/GaN can realize better stability due to the robustness of surface states [24]. However, the characteristics of the graded AlGaN/GaN SBDs are rarely reported, and investigations about leakage properties are still lacking.

In this work, the planar SBDs based on the fixed Al component AlGaN/GaN and the graded AlGaN/GaN heterostructures were fabricated, and their current-voltage (I-V) and capacitance-voltage (C-V) characteristics were evaluated and compared. The carrier distribution of the graded AlGaN/GaN heterostructures was analyzed according to the simulated and experimental results, which supported the extension of the carrier distribution. The forward and reverse currents of SBDs were also studied through the structures with and without recessed anode. As a result, the SBDs with the air-bridge structure have achieved a pretty low J_r value using graded AlGaN/GaN; meanwhile, the f_c is as high as 60.6 GHz.

2. Experiments

The samples of graded AlGaN/GaN heterostructures were grown on a c-plane sapphire substrate by metal-organic chemical vapor deposition (MOCVD). The sample structures consist of a 20 nm AlN nucleation layer, a 2.5 μm C-doped (4×10^{19} cm^{-3}) GaN buffer layer, a 200 nm unintentionally doped (UID) GaN, and a 35 nm graded $Al_{0\sim x}GaN$ barrier layer. C-doped GaN buffer layer is semi-insulating, which avoids the leakage current of the buffer layer and reduces the parasitic capacitance. Si concentration of UID GaN is lower than 10^{16} cm^{-3}. The Al component x of graded $Al_{0\sim x}GaN$ barrier layer from UID GaN to the surface is changed from 0 to 0.27 (S1) and from 0 to 0.35 (S2), as shown in Figure 1(a). In order to compare with the conventional AlGaN/GaN SBDs, a 35 nm fixed Al component $Al_{0.35}Ga_{0.65}N$/GaN heterostructure (S3) was designed, as shown in Figure 1(b). The distribution of Ga and Al composition in the S2 was measured by secondary ion mass spectroscopy (SIMS), as shown in Figure 1(c). It can be seen that the Al composition is graded from UID GaN to $Al_{0.35}Ga_{0.65}N$ surface, which extends the carrier distribution in the channel.

In order to verify the carrier distribution in the graded AlGaN barrier layer, the ring SBDs were fabricated with three steps. (1) The device mesa isolation of 300 nm was performed by dry etching using inductively coupled plasma (ICP). (2) The cathode ohmic metals of Ti/Al/Ni/Au (15/80/20/60 nm) were deposited by E-beam and thermal evaporator followed by rapid thermal annealing (RTA) at 850°C for 30 s in N_2. (3) The metals of Ni/Au (20/80 nm) were deposited in an anode. The schematics of their structures are illustrated in Figures 2(a) and 2(b). In conventional ring SBD, the anode radius (R) is 100 μm, and the space (L_{ac}) between the cathode and anode electrode is 20 μm. In recessed ring SBD, the recess radius (r) is 99 μm, which effectively reduces the capacitance of the ring SBD. Parts of anode metals were designed to be overlapped on the sample surface because the radius of the recess is less than the anode metal. The parallel connection of overlapped planar and recessed sidewall Schottky diode is formed in SBD with the recessed anode. Figure 2(c) shows an optical microscope photograph of ring SBD. The SBD with air-bridge structure was designed to improve f_c. The gold air-bridge which connected the small anode and electrode pad was fabricated using the electroplating technique. The structural parameters of the SBD with air-bridge structure are as follows: $R = 4\,\mu$m, $r = 3.95\,\mu$m, and $L_{ac} = 2\,\mu$m. The reduction of anode size can effectively increase the f_c. Figures 2(d) and 2(e) show the schematic structure and SEM image of the SBD with air-bridge structure, respectively.

The C-V characteristics were measured with alternating voltage of 30 mV amplitude and 1 MHz frequency by Keysight E4980 A LCR meter. The I-V characteristics were tested by Keithley 4200-SCS semiconductor parameter analyzer. All tests were performed at room temperature.

3. Results and Discussion

In order to obtain the characteristics of carrier concentration vs. depth in the graded AlGaN/GaN heterostructure, the C-V characteristics of the conventional ring SBDs and the recessed ring SBDs were measured, as shown in Figures 3(a) and 3(b). It is observed that the capacitance of recessed ring SBDs is reduced by two orders of magnitude compared with the conventional ring SBDs, which is attributed to the sharp reduction of the effective area of the parallel plate capacitor. Theoretically, the capacitance of conventional ring SBD can be described as a parallel plate capacitor with a depletion depth ($W = \varepsilon_0\varepsilon_s A/C$), where ε_0, ε_s, A, and C represent the vacuum dielectric constant, the dielectric constant of AlGaN, the anode area, and the capacitance of reverse-bias junction, respectively. The function of carrier concentration (N_A) vs. depth is described by the following equation [26]:

$$N_A(W) = \frac{1}{d\left(1/C^2\right)/dV} \cdot \frac{2}{q\varepsilon_0\varepsilon_s A^2}, \tag{1}$$

where q is the elementary charge. Based on this, the carrier distributions of S1, S2, and S3 were calculated and plotted in Figure 3(c). For S3, its carrier distribution width is the smallest and is quantified as 1.1 nm, which is much narrower than S1 (5.8 nm) and S2 (6.0 nm). Furthermore, it also has the largest carrier concentration (1.04×10^{20} cm^{-3}) compared to S1 (8×10^{18} cm^{-3}) and S2 (1.37×10^{19} cm^{-3}). As for S1and S2, it can be concluded that their carrier distribution is significantly extended to quasi 3-D electron slab in the graded AlGaN barrier layer. Additionally, the capacitance of S3 is smaller than those of S1 and S2 because the channel carriers are farther away from the anode metal. Consequently, S3 (V_{S3} = -6.5 V) shows a higher pinch-off voltage of depleted channel carriers compared with S1 (V_{S1} = -2.8 V) and S2 (V_{S2} = -3.2 V) owing to the higher carrier concentration and deeper carrier position.

Figure 3(d) shows the band structure versus the depth based on simulation results. The potential well is extended

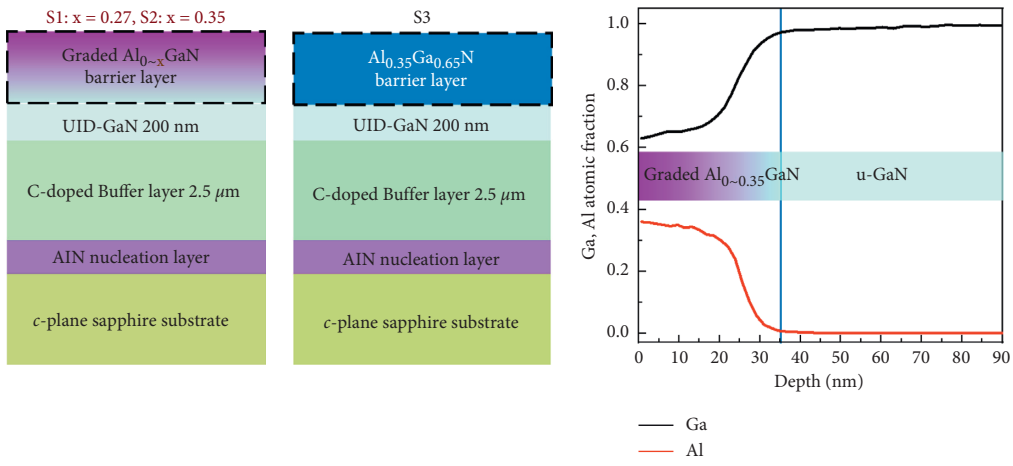

Figure 1: Schematic illustrations of (a) S1 and S2, and (b) S3. (c) Composition of Al and Ga in S2 by SIMS measurement.

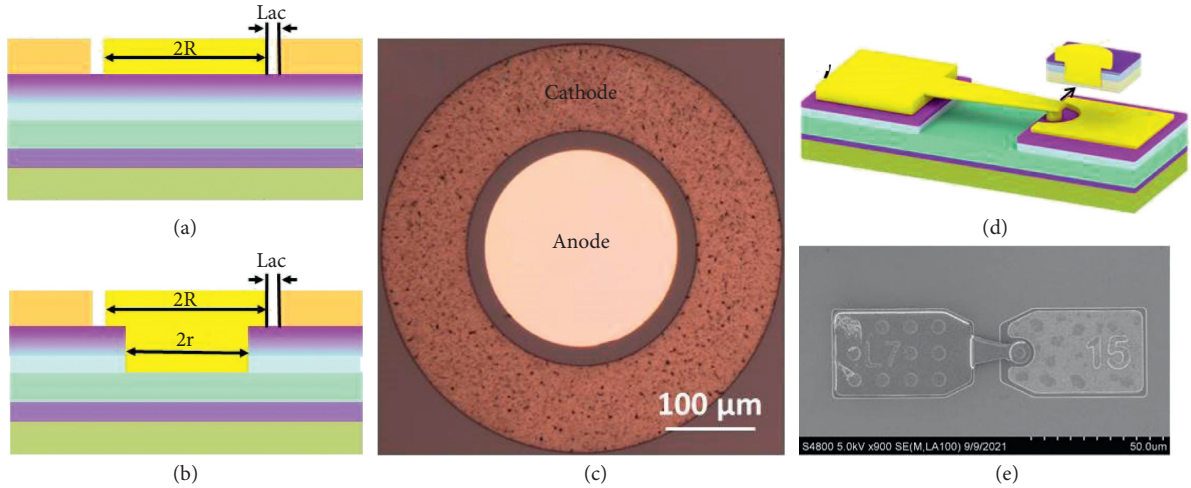

Figure 2: Schematic illustration of (a) conventional and (b) recessed ring SBDs. (c) Optical microscope photograph of ring SBDs. (d) Schematic illustration of the SBD with air-bridge structure. (e) The SEM image of the SBD with air-bridge structure.

from AlGaN/GaN interface to the graded AlGaN barrier layer. Figure 3(c)showsthe carrier distribution versus the depth, which is similar to the carrier distribution by C-V calculation. In order to investigate the extension of the carrier distribution, the distribution of polarization charge along the [0001] direction was calculated by the Poisson equation [27].

$$\nabla \cdot \left[\left(\varepsilon_z + \frac{e_z^2}{c_z} \right) \nabla \varphi \right] = -\rho + \nabla \cdot P_z, \tag{2}$$

where ε_z is permittivity, e_z is the piezoelectric coefficient, c_z is elastic constant, P_z is the total polarization in the material, φ is the electrostatic potential, and ρ is the charge distribution. The parameters of ε_z, e_z, c_z, and P_z are all in [0001] direction. The polarization charge density of the S1 and S2 is significantly reduced by two orders of magnitude compared with S3, demonstrating the extension effect of the graded AlGaN barrier layer on the positive polarization sheet charge at the AlGaN/GaN interface, as shown in Figures 3(e) and 3(f).

Figures 4(a) and 4(b) exhibit good Schottky diode properties of conventional and recessed ring SBDs. When the voltage is lower than the pinch-off voltage ($V_S < V_r < 0$ V), the currents gradually increase as the voltage increases due to the Frenkel-Poole (FP) emission mechanism [21, 28–30], and the channel carriers are not pinch-off at this time. In comparison with the S2 and S3, the S1 increases more slowly due to the thicker barrier width. When the voltage is higher than the pinch-off voltage ($V_r < V_S$), the currents reach saturation thanks to the pinch-off of channel carriers, and in this range, J_r is mainly due to the emission mechanism based on trap-assisted tunneling (TAT). Compared with the fixed Al composition AlGaN/GaN SBD, the saturated J_r of the graded AlGaN/GaN SBD is reduced due to the lower carrier concentration, wider depletion width, and lower tunneling probability. Moreover, the channel is more likely to be pinched off at lower reverse-bias

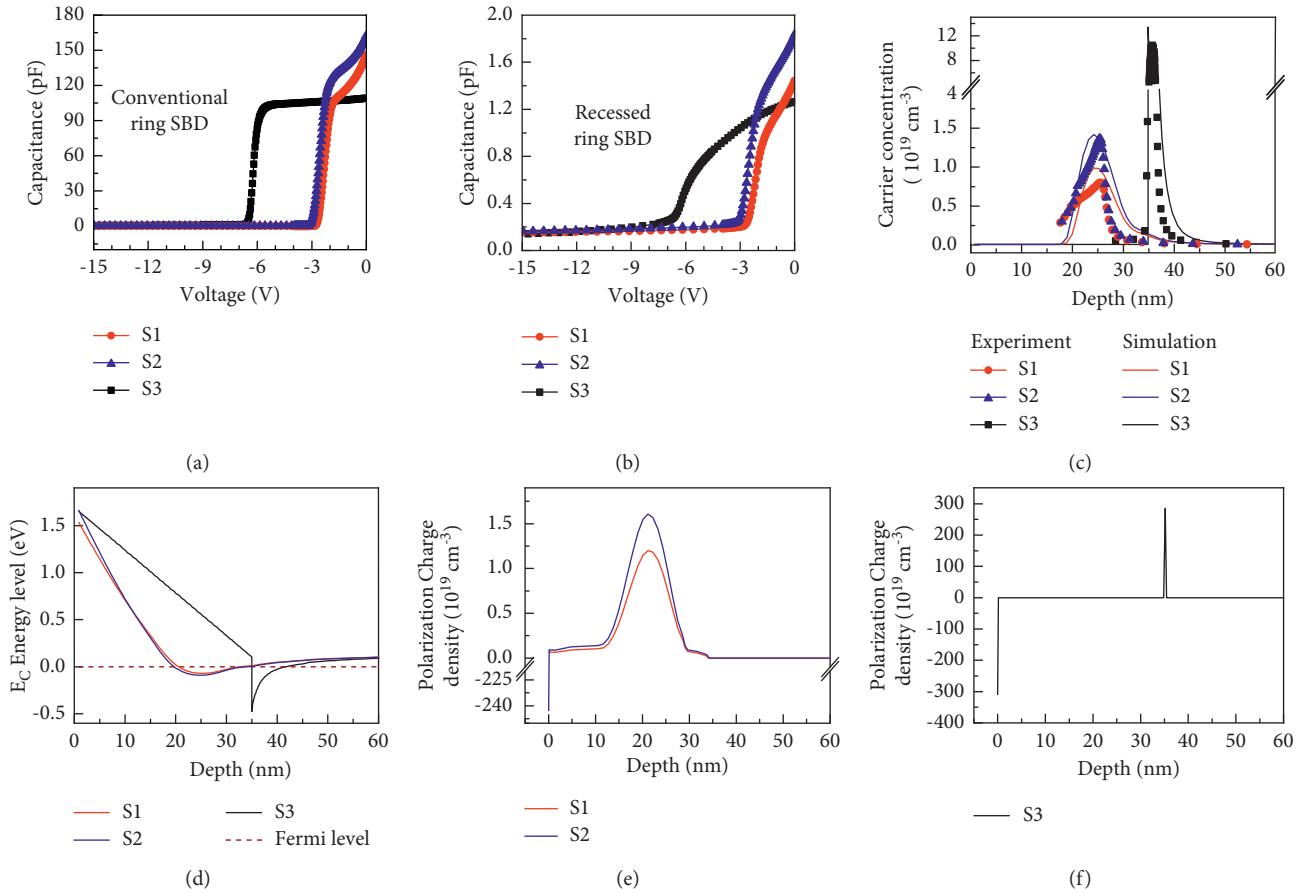

FIGURE 3: The C-V characteristics of (a) conventional and (b) recessed ring SBDs. (c) The carrier concentration vs. depths of S1, S2, and S3 by experiment and simulation. (d) The E_C energy level vs. depths of S1, S2, and S3. The distribution of polarization charge of (e) S1 and S2, and (f) S3.

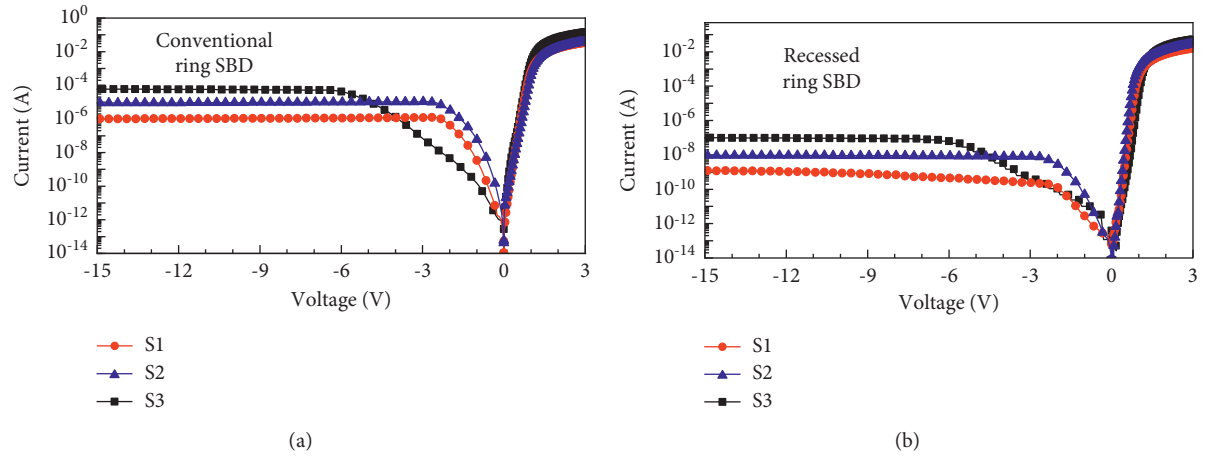

FIGURE 4: The I-V characteristics of (a) conventional and (b) recessed ring SBDs.

voltage due to shallow carrier distribution. In addition, we found that the saturated J_r values are a linear relationship with the effective anode area and are related to the trap concentration on the AlGaN surface [21]. In comparison with conventional rings SBDs, the saturated J_r values of recessed rings SBDs are reduced by about three orders of magnitude, which is contributed to the smaller effective anode area.

The electrical characteristics are summarized in Table 1. The ideality factor of SBDs is larger than 1, which indicates that the transport mechanisms include TAT, recombination, and thermionic emission (TE) under the forward voltage

Table 1: Electrical characteristics of SBDs.

Size (μm)	Sample	Ideality factor	Series resistance (Ω)	Saturated J_r at -15V (A)	Capacitance at 0 V	Cutoff frequency (GHz)
$R = 100$, $r = 0$	S1	1.64	51.5	1.0×10^{-6}	146 pF	0.021
	S2	1.68	39.4	8.8×10^{-6}	163 pF	0.025
	S3	1.53	21.5	5.9×10^{-5}	109 pF	0.067
$R = 100$, $r = 99$	S1	1.34	105.8	1.2×10^{-9}	1.44 pF	1.04
	S2	1.33	52.7	2.0×10^{-8}	1.84 pF	1.66
	S3	1.95	20.5	9.9×10^{-8}	1.25 pF	6.26
$R = 4$, $r = 3.95$	S1	1.89	368	1.6×10^{-13}	10.4 fF	41.7
	S2	1.94	210	1.9×10^{-12}	12.5 fF	60.6
	S3	2.19	151	3.4×10^{-10}	11.5 fF	91.6

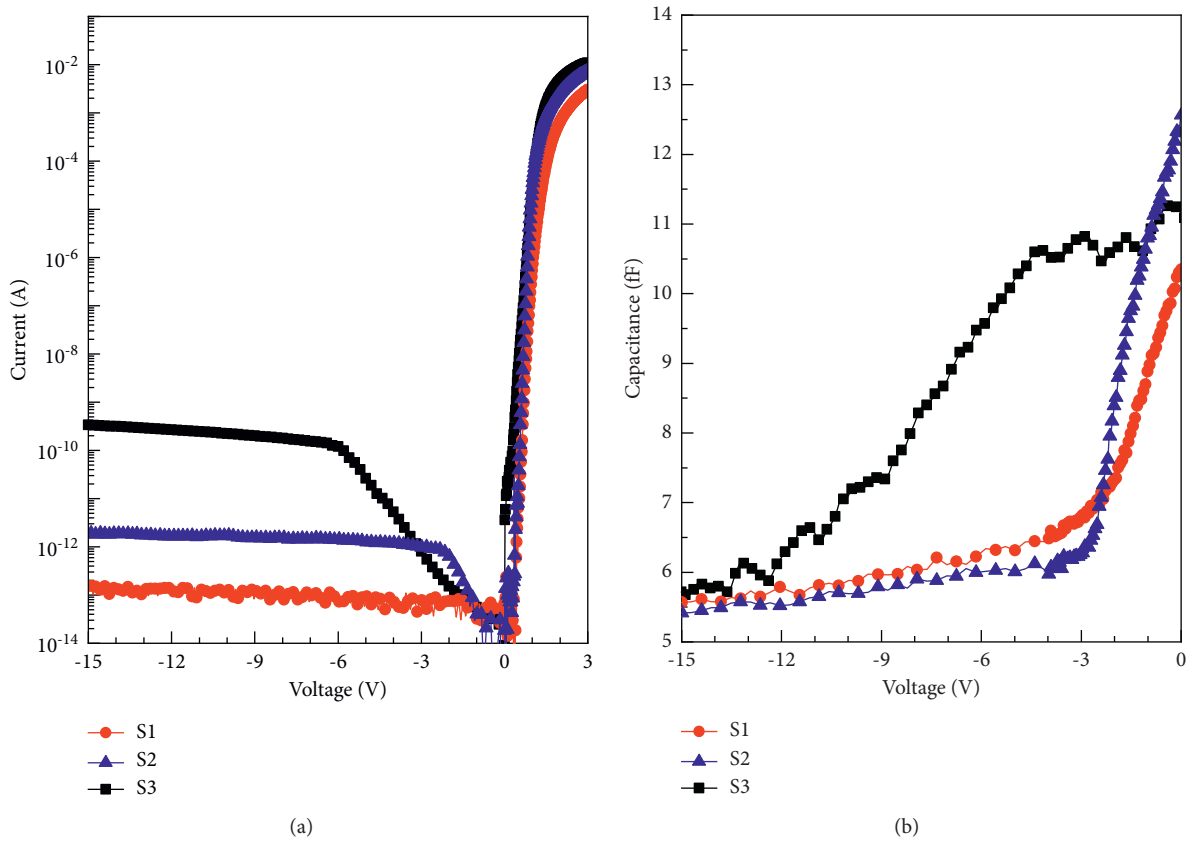

Figure 5: The (a) I-V and (b) C-V characteristics of the air-bridge structure planar SBDs.

[31–33]. The series resistance (R_s) of recessed ring SBDs is larger than conventional ring SBDs because the electrons laterally flow to the anode metal of the recessed sidewall. In comparison with conventional rings SBDs, the f_c of the recessed rings SBDs is improved by two orders of magnitude, as shown in Table 1.

The f_c of SBD is a very important parameter in MMW regions, which is defined as $f_c = 1/(2\pi R_s C_0)$ [34]. The reduction of R_s or C_0 is the only way to improve the f_c. In order to obtain a higher f_c, the SBD with an air-bridge structure is designed. The C-V and I-V characteristics are shown in Figures 5(a) and 5(b), respectively, which exhibit good Schottky diode properties. The value of the J_r between the two pads is about 2.8×10^{-14} A. The electrical characteristics are described in Table 1. In comparison with the SBD of S3, the J_r value of S2 is reduced by two orders of magnitude due to the extension of carriers in the channel. The capacitance of S3 is slowly decreased due to the sidewall capacitance of the recessed SBD device, as shown in Figure 5(b). The S2-based SBD with air-bridge structure shows R_s of 210 Ω, C_0 of 12.5 fF, f_c of 60.6 GHz, and J_r of 1.9×10^{-12} A at -15 V.

The J_r of the air-bridge structure planar SBDs is summarized in Figure 6. Compared with traditional GaAs-based SBDs, the GaN-based SBDs show a much higher breakdown voltage. What's more, the AlGaN/GaN SBDs show lower J_r values. In this work, the graded AlGaN/GaN SBDs with the air-bridge structure have achieved the lowest J_r values of 1.6×10^{-13} A at -15 V, which can effectively reduce the heating of the device in mixer and multiplier.

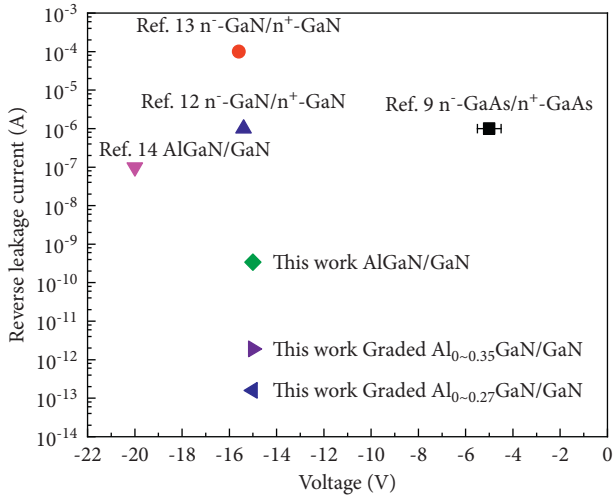

FIGURE 6: The J_r values of the air-bridge structure planar SBDs.

4. Conclusions

In summary, the characteristics of the graded AlGaN/GaN SBDs with and without recessed anode have been evaluated by the I-V and C-V. The carrier distribution of the graded AlGaN/GaN heterostructures was analyzed using the Poisson equation, which reveals the reasons for the extension of the carrier distribution. Compared with the fixed Al component AlGaN/GaN SBD, the J_r is reduced by two orders of magnitude due to the extension of the carrier distribution. The graded AlGaN/GaN SBDs with air-bridge structure have achieved a pretty low J_r value (1.6×10^{-13} A at -15 V). The f_c of graded $Al_{0\sim0.35}GaN/GaN$ SBD with air-bridge structure is 60.6 GHz, and the J_r is as small as 1.9×10^{-12} A at -15 V. These are beneficial to the applications of MMW in the future.

Data Availability

The data that were used to support this study are included within the article.

Conflicts of Interest

The authors declare that there are no conflicts of interest to disclose.

Acknowledgments

This work was partially supported by the Science and Technology Plan of Guangdong Province, China (Grant nos. 2019B010132003 and 2019B010132001), the joint funding of the Nature Science Foundation of China and the Macao Science and Technology Development Fund of China (Grant no. 62061160368), the National Key Research and Development Program (Grant nos. 2016YFB0400105 and 2017YFB0403001), and the Zhuhai Key Technology Laboratory of Wide Bandgap Semiconductor Power Electronics, Sun Yat-sen University, China (Grant no. 20167612042080001).

References

[1] L. Yujiri, M. Shoucri, and P. Moffa, "Passive millimeter-wave imaging," *IEEE Microwave Magazine*, vol. 4, no. 3, pp. 39–50, 2003.

[2] D. M. Sheen, D. L. McMakin, and T. E. Hall, "Three-dimensional millimeter-wave imaging for concealed weapon detection," *IEEE Transactions on Microwave Theory and Techniques*, vol. 49, no. 9, pp. 1581–1592, 2001.

[3] S. Kharkovsky and R. Zoughi, "Microwave and millimeter wave nondestructive testing and evaluation - overview and recent advances," *IEEE Instrumentation and Measurement Magazine*, vol. 10, no. 2, pp. 26–38, 2007.

[4] J. Hasch, E. Topak, R. Schnabel, T. Zwick, R. Weigel, and C. Waldschmidt, "Millimeter-wave technology for automotive radar sensors in the 77 GHz frequency band," *IEEE Transactions on Microwave Theory and Techniques*, vol. 60, no. 3, pp. 845–860, 2012.

[5] J. Choi, V. Va, N. Gonzalez-Prelcic, R. Daniels, C. R. Bhat, and R. W. Heath, "Millimeter-wave vehicular communication to support massive automotive sensing," *IEEE Communications Magazine*, vol. 54, no. 12, pp. 160–167, 2016.

[6] W. Roh, J.-Y. Seol, J. Park et al., "Millimeter-wave beamforming as an enabling technology for 5G cellular communications: theoretical feasibility and prototype results," *IEEE Communications Magazine*, vol. 52, no. 2, pp. 106–113, 2014.

[7] U. R. Pfeiffer, C. Mishra, R. M. Rassel, S. Pinkett, and S. K. Reynolds, "Schottky barrier diode circuits in silicon for future millimeter-wave and terahertz applications," *IEEE Transactions on Microwave Theory and Techniques*, vol. 56, no. 2, pp. 364–371, 2008.

[8] T. W. Crowe, J. L. Hesler, R. M. Weikle, and S. H. Jones, "GaAs devices and circuits for terahertz applications," *Infrared Physics & Technology*, vol. 40, no. 3, pp. 175–189, 1999.

[9] W. L. Bishop, K. Mckiney, R. J. Mattauch, T. W. Crowe, and G. Green, "A novel whiskerless Schottky diode for millimeter and submillimeter wave application," *IEEE MTT-S International Microwave Symposium Digest (Cat. No.87CH2395-2)*, vol. 2, pp. 607–610, 1987.

[10] S. Xiao, T. Wang, T. Liu, C. Zhou, X. Jiang, and J. Zhang, "Active metamaterials and metadevices: a review," *Journal of Physics D-Applied Physics*, vol. 53, no. 50, Article ID 503002, 2020.

[11] Y. Liu, W. Yao, and H. Liu, "Multi-channel AlGaN/GaN Schottky barrier diodes with a half through-hole," *Materials Science in Semiconductor Processing*, vol. 133, Article ID 105934, 2021.

[12] S. Liang, X. Zhang, Y. Lv et al., "A 177-183 GHz high-power GaN-based frequency doubler with over 200 mW output power," *IEEE Electron Device Letters*, vol. 41, no. 5, pp. 669–672, 2020.

[13] B. Zhang, D. Ji, D. Fang, S. Liang, Y. Fan, and X. Chen, "A novel 220-GHz GaN diode on-chip tripler with high driven power," *IEEE Electron Device Letters*, vol. 40, no. 5, pp. 780–783, 2019.

[14] L. Yang, W. Yao, and Y. Liu, "Low capacitance AlGaN/GaN based air-bridge structure planar Schottky diode with a half through-hole," *AIP Advances*, vol. 10, no. 4, Article ID 045219, 2020.

[15] L. Hsu and W. Walukiewicz, "Electron scattering mechanisms at polar GaN/AlGaN interfaces," *Ultrafast Phenomena in Semiconductors Vi*, vol. 4643, pp. 148–162, 2002.

[16] E. T. Yu, X. Z. Dang, P. M. Asbeck, S. S. Lau, and G. J. Sullivan, "Spontaneous and piezoelectric polarization effects in III-V

nitride heterostructures," *Journal of Vacuum Science & Technology B: Microelectronics and Nanometer Structures*, vol. 17, no. 4, pp. 1742–1749, 1999.

[17] O. Ambacher, J. Smart, J. R. Shealy et al., "Two-dimensional electron gases induced by spontaneous and piezoelectric polarization charges in N- and Ga-face AlGaN/GaN heterostructures," *Journal of Applied Physics*, vol. 85, no. 6, pp. 3222–3233, 1999.

[18] W. J. Ha, S. Chhajed, and S. J. Oh, "Analysis of the reverse leakage current in AlGaN/GaN Schottky barrier diodes treated with fluorine plasma," *Applied Physics Letters*, vol. 100, no. 13, Article ID 132104, 2012.

[19] X. Y. Liu, S. X. Zhao, and L. Q. Zhang, "AlGaN/GaN MIS-HEMTs with AlN gate dielectric grown by thermal ALD technique," *Nanoscale Research Letters*, vol. 10, Article ID 109, 2015.

[20] T. Sun, X. Luo, J. Wei, C. Yang, and B. Zhang, "Theoretical and experimental study on AlGaN/GaN Schottky barrier diode on Si substrate with double-heterojunction," *Nanoscale Research Letters*, vol. 15, no. 1, Article ID 149, 2020.

[21] Y. Yao, J. Zhang, and Y. Zheng, "Current transport mechanism of AlGaN/GaN Schottky barrier diode with fully recessed Schottky anode," *Japanese Journal of Applied Physics*, vol. 54, no. 1, Article ID 011001, 2015.

[22] D. Jena, S. Heikman, D. Green et al., "Realization of wide electron slabs by polarization bulk doping in graded III-V nitride semiconductor alloys," *Applied Physics Letters*, vol. 81, no. 23, pp. 4395–4397, 2002.

[23] Y. Fang, Z. Feng, C. Li et al., "Trap behaviors in AlGaN/GaN based polarization-doped field effect transistors by frequency-dependent conductance-voltage characterizations," *Superlattices and Microstructures*, vol. 82, pp. 201–206, 2015.

[24] Y. Fang, Z. Feng, J. Yin et al., "AlGaN/GaN polarization-doped field-effect transistors with graded heterostructure," *IEEE Transactions on Electron Devices*, vol. 61, no. 12, pp. 4084–4089, 2014.

[25] S. Rajan, H. Xing, S. DenBaars, U. K. Mishra, and D. Jena, "AlGaN/GaN polarization-doped field-effect transistor for microwave power applications," *Applied Physics Letters*, vol. 84, no. 9, pp. 1591–1593, 2004.

[26] J. Hilibrand and R. D. Gold, "Determination of the impurity distribution in junction diodes from capacitance-voltage measurements," *RCA Review*, vol. 21, pp. 245–252, 1960.

[27] B. Jogai, J. D. Albrecht, and E. Pan, "Effect of electromechanical coupling on the strain in AlGaN/GaN heterojunction field effect transistors," *Journal of Applied Physics*, vol. 94, no. 6, pp. 3984–3989, 2003.

[28] H. Zhang, E. J. Miller, and E. T. Yu, "Analysis of leakage current mechanisms in Schottky contacts to GaN and Al0.25Ga0.75N/GaN grown by molecular-beam epitaxy," *Journal of Applied Physics*, vol. 99, no. 2, Article ID 023703, 2006.

[29] J. H. Shin, J. Park, S. Jang, T. H. Jang, and K. S. Kim, "Gate metal dependent reverse leakage mechanisms in AlGaN/GaN Schottky diode," *Japanese Journal of Applied Physics*, vol. 52, no. 7, Article ID 70203, 2013.

[30] E. Arslan, S. Butun, and E. Ozbay, "Leakage current by Frenkel-Poole emission in Ni/Au Schottky contacts on Al0.83In0.17N/AlN/GaN heterostructures," *Applied Physics Letters*, vol. 94, no. 14, Article ID 142106, 2009.

[31] M. Grundmann, R. Karsthof, and H. von Wenckstern, "Interface recombination current in type II heterostructure bipolar diodes," *ACS Applied Materials & Interfaces*, vol. 6, no. 17, pp. 14785–14789, 2014.

[32] D. Yan, J. Jiao, J. Ren, G. Yang, and X. Gu, "Forward current transport mechanisms in Ni/Au-AlGaN/GaN Schottky diodes," *Journal of Applied Physics*, vol. 114, Article ID 144511, 2013.

[33] S. Kotzea, A. Debald, M. Heuken, H. Kalisch, and A. Vescan, "High-mobility GaN-on-sapphire p-n diodes with near-unity ideality factor and large breakdown voltage," *Journal of Physics D: Applied Physics*, vol. 52, Article ID 285101, 2014.

[34] K. S. Champlin and G. Eisenstein, "Cutoff frequency of submillimeter Schottky-barrier diodes," *IEEE Transactions on Microwave Theory and Techniques*, vol. 26, no. 1, pp. 31–34, 1978.

Hindawi
Advances in Condensed Matter Physics
Volume 2021, Article ID 7188175, 6 pages
https://doi.org/10.1155/2021/7188175

Research Article

Thermal Conductivity of Graphitic Carbon Nitride Nanotubes: A Molecular Dynamics Study

Hui Guo,[1] **Chunqing Huo**,[2] **Liang Yang**,[2] **and Shiwei Lin**[2]

[1]*College of Science, Hainan University, Haikou 570228, China*
[2]*School of Materials Science and Engineering, Hainan University, Haikou 570228, China*

Correspondence should be addressed to Liang Yang; yl5923@hainanu.edu.cn and Shiwei Lin; linsw@hainanu.edu.cn

Received 20 October 2021; Revised 22 November 2021; Accepted 26 November 2021; Published 15 December 2021

Academic Editor: Shuyuan Xiao

Graphitic carbon nitride (g-C_3N_4) nanotubes are recently gaining increasing interest due to their extraordinary physicochemical properties. In the following, we report on simulations using a method of nonequilibrium molecular dynamics and focus on the thermal conductivity variation of g-C_3N_4 nanotubes with respect to different temperatures, diameters, and chiral angles. In spite of the variation of diameters and chiral angles, the structure of nanotubes possesses high stability in the temperature range from 200 K to 600 K. Although there is little change of the thermal conductivity per unit arc length for nanotubes with the same diameter at different temperatures, it decreases significantly with increasing diameters at the same temperature. The thermal conductivity at different chiral angles has little to do with how temperature changes. Simulation results show that the vibrational density of states of nanotubes distributed, respectively, at ~11 THz and ~32 THz, indicating that heat in nanotubes is mostly carried by phonons with frequencies lower than 10 THz.

1. Introduction

Graphitic carbon nitride (g-C_3N_4) is a two-dimensional semiconductor material with graphene-like single-layer structure [1]. It has attracted tremendous attention and has been widely applied in many fields because of the stable physicochemical and excellent electro-optical properties, such as the production of hydrogen from water photolysis [2], battery production [3], photocatalysis [4, 5], and electrochemistry [6] processes. Recently, one-dimensional nanotube structural g-C_3N_4 analogous materials have been successfully prepared [7], and enormous progress has been made in both experimental research and theoretical explorations. On the one hand, g-C_3N_4 nanotubes have been successfully prepared on porous Al_2O_3 anode plates via the sol-gel process. Bian et al. [8] further improved their hydrogen evolution ability by depositing Pt nanoparticles on the tube wall. g-C_3N_4 nanotubes synthesized by the two-step method displayed 12 times higher photocatalytic efficiency than that of bulk materials when decomposing rhodamine B [9]. On the other hand, first-principle calculation was used to predict the structural stability and electronic properties of g-C_3N_4 tubular composite materials, which indeed verified the stable existence of nanotube structural materials [10]. Pan et al. further discovered that electronic structures of g-C_3N_4 nanotubes have adjustable band gaps and predicted that they could be used in the conversion of solar energy [11]. However, most of these research studies on g-C_3N_4 nanotubes are focused on their photoelectric properties; very few discussed their thermodynamic properties, especially thermal conductivity. In many applications, g-C_3N_4 is often used to make composites, and thus, its thermal conductivity may significantly affect the nature of the composites and the catalysis process. The lack of cognition of the thermal conductivity of g-C_3N_4 greatly prevents the in-depth understanding of g-C_3N_4 nanotubes and their applications.

Here, we have employed molecular dynamics (MD) simulation method to investigate the relation between the thermal conductivity of g-C_3N_4 nanotubes and temperature, nanotube diameters, and chiral angles. It will be shown that the thermal mechanism of nanotubes is closely related with vibrational density of state, the nanotubes process high

stability at a wide temperature range, thermal conductivity is closely related to diameters, and heat in nanotubes is mostly carried by phonons with certain frequencies.

2. Computational Model and Method

2.1. Computational Model. A model from Momma and Izumi is used in this study, as shown in Figure 1 [12].

At present, the most widely applied two-dimensional CN compound should be the g-C_3N_4 structure. Then, it is also applied here to construct nanotubes with the axial length of about 120 nm. Based on the structural symmetry, the chiral angles at different chiral directions of the constructed nanotube cells were $m1 = 0^\circ$, $m2 = 6^\circ$, $m3 = 20^\circ$, $m4 = 30^\circ$, $m5 = 40^\circ$, $m6 = 54^\circ$, and $m7 = 60^\circ$, respectively, as shown in Figure 1. In addition, different inner diameters (0.71 nm, 1.18 nm, 1.72 nm, 2.13 nm, 2.35 nm, and 2.59 nm) of nanotubes were also constructed at chiral angle $m1 = 0^\circ$. The information of the constructed nanotubes and the computational parameters are shown in Table 1. The computation is implemented by Device Studio software.

2.2. Computational Method. Large-scale Atomic/Molecular Massively Parallel Simulator (LAMMPS) package, an open-source MD code, was applied in the MD simulation [13]. The accuracy of the MD simulation strongly depends on the classical force fields utilized to describe the interatomic forces. Potential proposed by Tersoff (Tersoff potential) [14] was used to calculate the interaction between carbon and nitrogen atoms. Nonequilibrium molecular dynamics method was employed for the computation of thermal conductivity. For a single nanotube, heat transferred directly from every hot end (0.5 nm from the bottom end) to every cold end (0.5 nm away from the center of the length). Therefore, the thermal conductivity (κ) can be directly obtained from the temperature gradient (ΔT) and the heat flux of the system (J) through Fourier's formula [1]:

$$\kappa = -\frac{J}{\Delta T}. \tag{1}$$

In order to keep the constant energy and momentum of the system, 0.2 eV energy (Q) was added into the hot end per ps, while the same energy Q was subtracted from the cold end. Then, heat flow and a stable temperature gradient can be formed between the two ends in such a stable system. The heat flux can be determined by $J = Q/S$, where S is the cross-sectional area of the system. The temperature gradient is expressed as $\Delta T = \mathrm{d}T/\mathrm{d}L$, which is the derivative of the linear temperature change.

As shown in Figure 2, the temperature changes linearly in the axial direction in a stable system. Therefore, the thermal conductivity (κ) can be calculated by

$$\kappa = -\frac{Q/S}{\mathrm{d}T/\mathrm{d}L}. \tag{2}$$

The phonon density of states is obtained by calculating the fast Fourier transform of the phonon spectrum from the velocity autocorrelation function (VACF) of the system and is responsible for the change of thermal conductivity with nanotube diameters and temperature. Here, VACF is calculated by the following formula:

$$\mathrm{VACF}(t) = \frac{\langle \sum_{i=1}^{N} \vec{v}_i\,(t_0)\vec{v}_i\,(t_0 + t)\rangle}{\langle \sum_{i=1}^{N} \vec{v}_i\,(t_0)\vec{v}_i\,(t_0)\rangle}, \tag{3}$$

where N is the total atomic number of the system, $\vec{v}_i\,(t_0)$ is the velocity of the ith atom at time t_0, and $\langle\cdot\rangle$ is the ensemble average. Vibrational density of states (VDOS) of the phonon with frequency v can be obtained:

$$\mathrm{VDOS}(\nu) = \int_{-\infty}^{+\infty} \mathrm{VACF}(t) e^{-2\pi i \nu t}\,\mathrm{d}t. \tag{4}$$

Periodic boundary conditions were used in this simulation. First, the energy of the system was minimized. In order to ensure the stability of the calculation system, the time step was 0.2 fs. Then, NPT ensemble and NVT ensemble were implemented, respectively, and the structure was optimized at constant temperature for 0.4 ns. Then, the system was switched to constant energy (NVE) simulations for 20 ns. During this period, the temperature distribution curve (as shown in Figure 3) was obtained once per 1 ns, and the average temperature difference was output. According to the formula [2], the thermal conductivity and VACF can be calculated by using the data after 1 ns.

The simulated thermal conductivity of single-layer g-C_3N_4 ($14.76 \times 12.78 \times 0.5$ nm) is about 2.93 W/(K•m), which is comparable to the result calculated by equilibrium MD based on the Green–Kubo formula (3.5 ± 0.3 W/K•m) [15]. This proves the reliability of the methodology adopted here in describing the thermal properties of g-C_3N_4 systems.

3. Results and Discussion

3.1. Stability of the Nanotubes. The maximum diameter of the nanotubes (2.5 nm) studied here is limited mainly by the computation cost, which results in a strong internal stress. It is then easy to cause nanotube collapse and deformation with increasing temperature, leading to a meaningless calculation. However, nanotubes with different diameters can approximately retain their structure if the temperature is lower than 600 K, as shown in Figure 4. Although there still exists tiny deformation, the simulated result of the thermal conductivity is quite reliable.

The corresponding relation between the (m, n) vector and diameters can be referred to Table 1, and it is clear in Figure 4 that the basic orientation of the tube can significantly affect the shape of the tube. When the diameter is small, the tube shows a distorted shape. When the diameter increases, the tube wall becomes smoother, and the tube becomes straighter. And when the value of m and n is small, the atom distribution is generally sparse. The structure of the tubes may further influence the thermal properties of the tubes, which will be discussed later.

3.2. Size Effects on the Thermal Conductivity of the Nanotube. Surface stress exists while rolling the two-dimensional g-C_3N_4 layers along different chiral angles. The stress is the

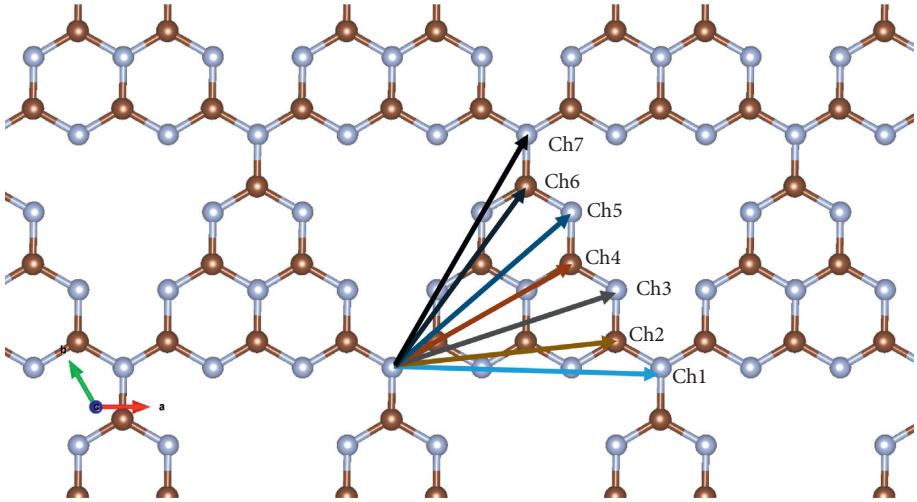

Figure 1: Nanotube cells defined by the chiral vector Ch = (n, m), where n and m are vector components in two different directions.

Table 1: The information of the constructed nanotubes and the computational parameters.

Chiral vector	(n, m)	Chiral angle (°)	Diameter (nm)	Length of the nanotube (nm)	Number of atoms
Ch1	(3, 0)	0	0.71	11.50	756
Ch1	(5, 0)	0	1.18	11.50	1260
Ch1	(7, 0)	0	1.72	11.50	1764
Ch1	(9, 0)	0	2.13	11.50	2268
Ch1	(10, 0)	0	2.35	11.50	2520
Ch1	(11, 0)	0	2.59	11.50	2772
Ch2	(10, 1)	6	2.24	12.19	2548
Ch3	(12, 4)	20	2.49	13.53	3136
Ch4	(10, 5)	30	2.05	11.81	2240
Ch5	(12, 8)	40	2.09	12.55	2380
Ch6	(10, 9)	54	2.27	12.19	2548
Ch7	(10, 10)	60	2.35	11.50	2520

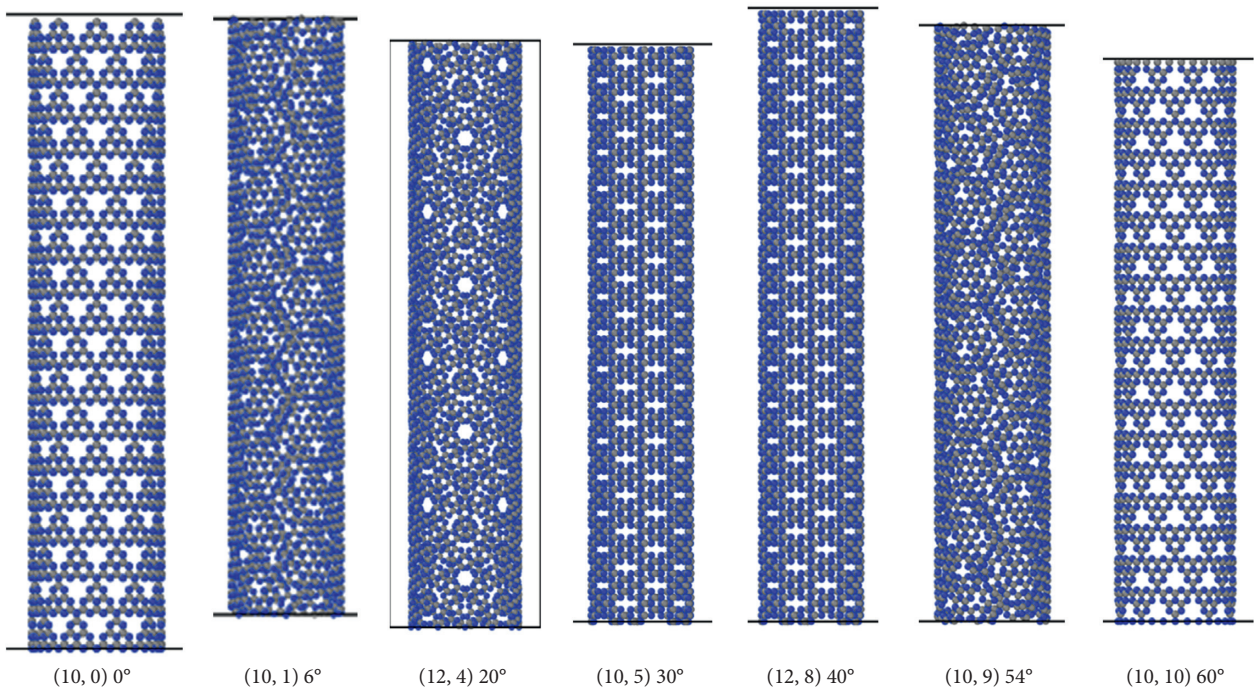

Figure 2: Side view of nanotubes at different chiral angles.

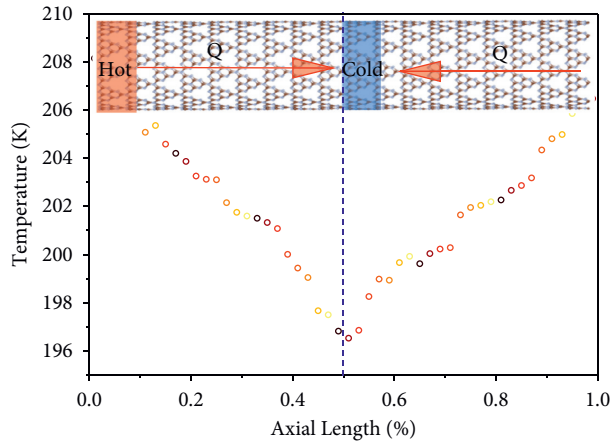

Figure 3: Schematic diagram of the thermal conductivity calculation of g-C_3N_4.

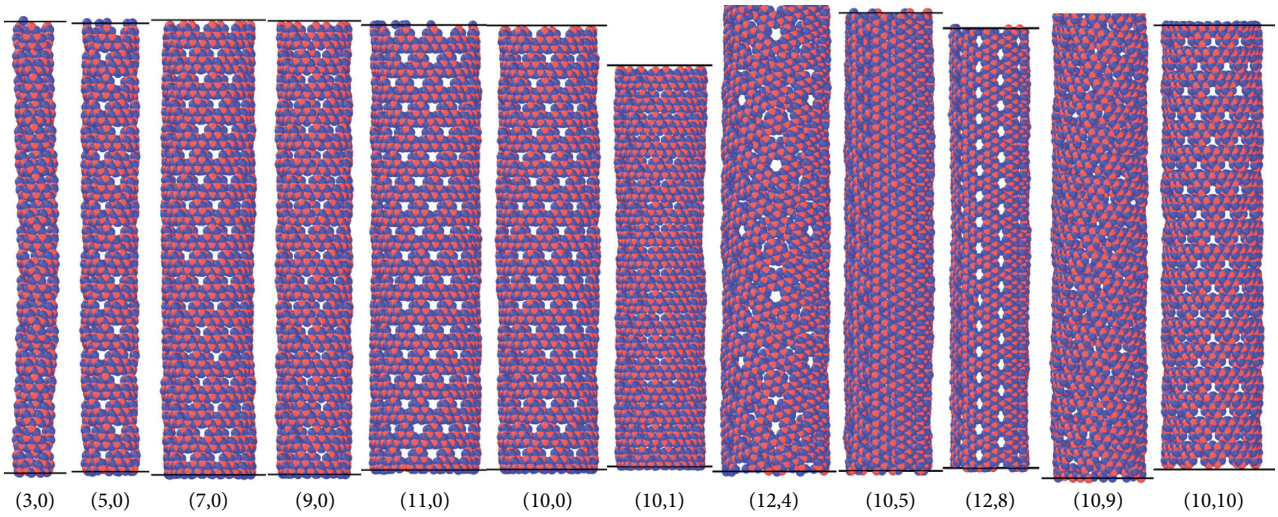

Figure 4: Nanotubes with different diameters at temperature less than 600 K.

change of phonon density of states caused by the atomic force in the microscopic scale, while the macroscopic performance is quite different. For nanotubes with different diameters, the number of atoms in the same plane is different. To figure out the intrinsic size effects of the thermal conductivity of nanotubes, the thermal conductivity per unit arc length is introduced [16]:

$$\kappa_s = \frac{\kappa}{\pi d}, \tag{5}$$

where d is the nanotube diameter.

The thermal conductivity per unit arc length of g-C_3N_4 with outer diameter from 3 to 17 nm varies little with temperature in the range of 200–600 K (as shown in Figure 5), which is very different from that of other carbon nanotubes [16].

As shown in Figure 6, the thermal conductivity per unit arc length of nanotubes decreases significantly with increasing diameters. This indicates that the internal tension between the atoms of nanotubes becomes weaker with larger diameter, which makes it difficult for the thermal vibration

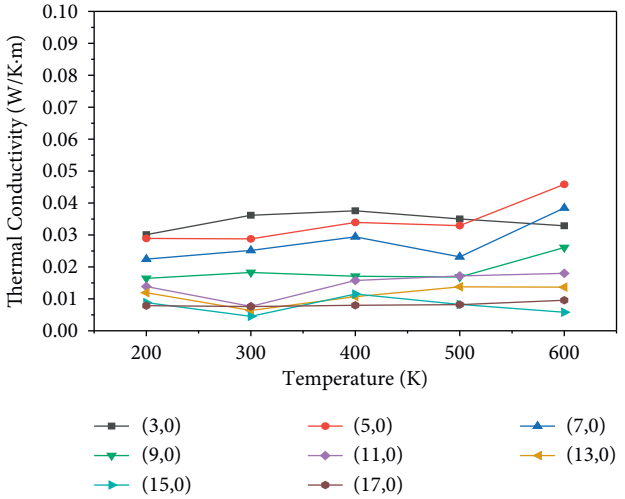

Figure 5: The temperature dependence of the thermal conductivity of unit arc length of g-C_3N_4 with outer diameters from 3 to 17 nm.

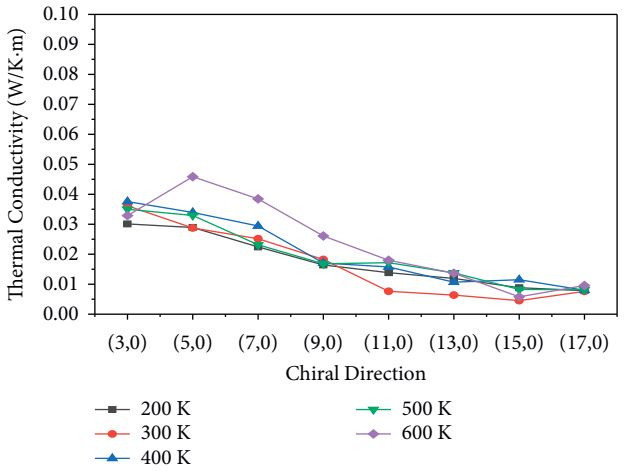

Figure 6: The diameter dependence of the thermal conductivity of unit arc length of g-C_3N_4 nanotubes.

between adjacent atoms to propagate smoothly along the axial direction.

3.3. Chirality Effects on the Thermal Conductivity of the Nanotube. Rolling two-dimensional materials along different chiral angles can form nanotube structures with different chiral angles, leading to different atomic arrangements with different physicochemical properties. Therefore, it is meaningful to study the influence of chiral angles on the thermal conductivity of nanotubes. As shown in Figure 7, the thermal conductivity of a single chiral nanotube varies little with the temperature in the range of 200–600 K. For nanotubes with different chiral angles, the atomic thermal vibration of the nanotubes is intensified, but the contribution to heat conduction is limited.

The thermal conductivity of nanotubes varies little with the chiral angles under the same temperature, as shown in Figure 8, which indicates that it is impossible to adjust the thermal conductivity by changing only the chiral angles of nanotubes. We have shown in Figure 4 that the chiral angles can influence both diameter and atom distribution of the nanotubes. Generally speaking, a dense atom distribution on the tube walls is apt to increase the thermal conductivity. On the contrary, smaller diameter will increase the atom density in the 3D space, which is likely to increase the thermal conductivity. The two factors are contradictory. Thus, when m and n are small, the atom distribution on the tube wall is sparse, yet the diameter is small, compensating the decrease of thermal conductivity. Thus, the final thermal conductivity may be decided by the relation of the two factors.

3.4. Vibrational Density of States (VDOS). In order to gain more insight into the chirality effects on the thermal conductivity of nanotubes, the VDOS of nanotubes was calculated since vibrational properties at low frequency are corresponding to the thermal conductivity property. As shown in Figure 9, the VDOS of nanotubes at different chiral angles calculated at low temperature (300 K) was mainly

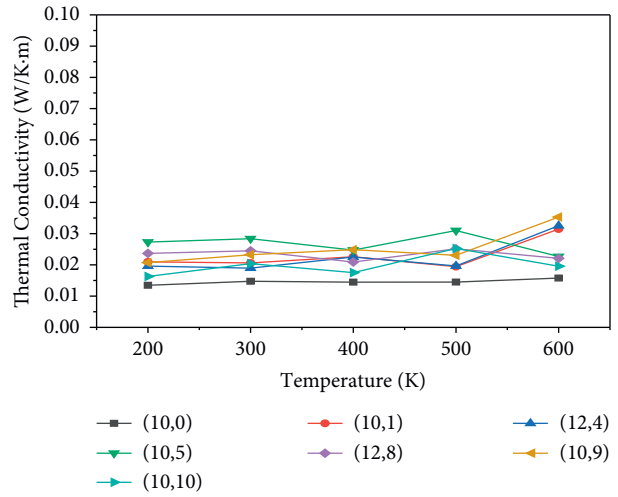

Figure 7: The temperature dependence of the thermal conductivity of different chiral nanotubes.

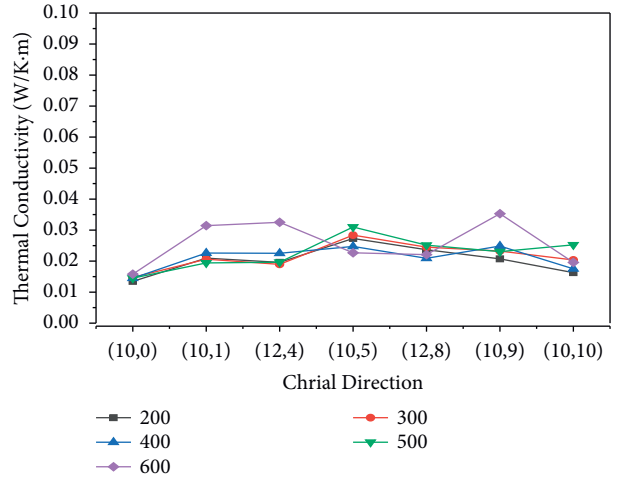

Figure 8: The chiral angles' dependence of the thermal conductivity at single temperature.

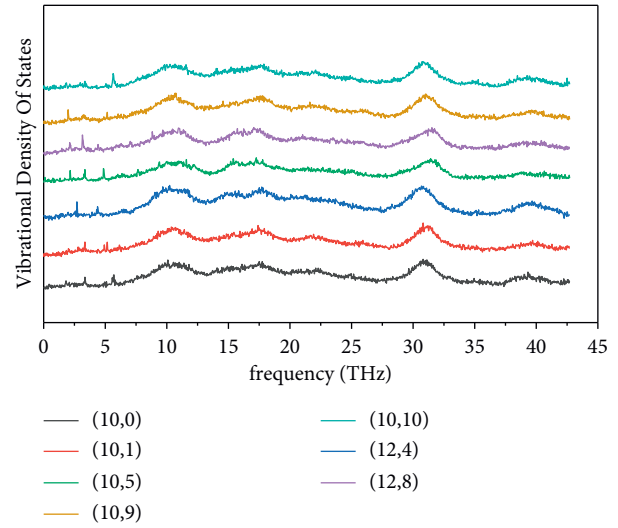

Figure 9: Vibrational density of states (VODS) of nanotubes with different chiral angles at temperature 300 K.

concentrated in frequencies ~11 THz and ~32 THz. There are few vibrational modes at frequencies lower than 10 THz, which respond mainly to effective heat conduction. Therefore, the thermal conductivity of nanotubes with different chiral angles was very low. This is also true for the VDOS at different temperatures with the same diameter or chiral angle. In general, it can be seen that the vibrational modes of g-C_3N_4 at low frequency are quite few, and heating or changing chiral angles plays a minor role in adjusting the thermal conductivity.

4. Conclusions

In summary, the dependence of the thermal conductivity of g-C_3N_4 nanotubes on temperature, diameters, and chiral angles of the nanotubes was characterized by molecular dynamics study. The simulation results suggest that, for a single nanotube, the thermal conductivity is not sensitive to temperature and chiral angles, while under the same temperature, the thermal conductivity decreases significantly with increasing nanotube diameters. These results provide useful thermal information in guiding the design and application of g-C_3N_4 nanotubes in the future devices.

Data Availability

The data used to support the findings of this study are included within the article.

Conflicts of Interest

The authors declare no conflicts of interest.

Acknowledgments

This work was supported by the Hainan Provincial Natural Science Foundation of China (Grant no. 519MS025) and the Education and Teaching Research Project Funding of Hainan University (Grant no. hdjy2160).

References

[1] J. Gao, Y. Zhou, Z. Li, S. Yan, N. Wang, and Z. Zou, "High-yield synthesis of millimetre-long, semiconducting carbon nitride nanotubes with intense photoluminescence emission and reproducible photoconductivity," *Nanoscale*, vol. 4, no. 12, pp. 3687–3692, 2012.

[2] C. Han, Y. Wang, Y. Lei et al., "In situ synthesis of graphitic-C_3N_4 nanosheet hybridized N-doped TiO2 nanofibers for efficient photocatalytic H_2 production and degradation," *Nano Research*, vol. 8, no. 4, pp. 1199–1209, 2015.

[3] Y. Zheng, J. Liu, J. Liang, M. Jaroniec, and S. Z. Qiao, "Graphitic carbon nitride materials: controllable synthesis and applications in fuel cells and photocatalysis," *Energy & Environmental Science*, vol. 5, no. 5, pp. 6717–6731, 2012.

[4] T. N. Yan, E. H. Liu, Z. Y. Chu, and X. D. Li, "Scalable synthesis of ultrathin g-C_3N_4 nanosheets with enhanced photocatalytic activities via high shear exfoliation," *Journal of Nano Research*, vol. 45, pp. 49–54, 2017.

[5] S. Sun, E. Fan, H. Xu et al., "Enhancement of photocatalytic activity of g-C_3N_4 by hydrochloric acid treatment of melamine," *Nanotechnology*, vol. 30, no. 31, Article ID 315601, 2019.

[6] F. K. Kessler, Y. Zheng, D. Schwarz et al., "Functional carbon nitride materials-design strategies for electrochemical devices," *Nature Reviews Materials*, vol. 2, no. 6, pp. 1–17, 2017.

[7] X. Li, K. Pan, Y. Qu, and G. Wang, "One-dimension carbon self-doping g-C_3N_4 nanotubes: synthesis and application in dye-sensitized solar cells," *Nano Research*, vol. 11, no. 3, pp. 1322–1330, 2018.

[8] S.-W. Bian, Z. Ma, and W.-G. Song, "Preparation and characterization of carbon nitride nanotubes and their applications as catalyst supporter," *Journal of Physical Chemistry C*, vol. 113, no. 20, pp. 8668–8672, 2009.

[9] Z. Jin, Q. Zhang, S. Yuan, and T. Ohno, "Synthesis high specific surface area nanotube g-C_3N_4 with two-step condensation treatment of melamine to enhance photocatalysis properties," *RSC Advances*, vol. 5, no. 6, pp. 4026–4029, 2015.

[10] Y. Miyamoto, M. L. Cohen, and S. G. Louie, "Theoretical investigation of graphitic carbon nitride and possible tubule forms," *Solid State Communications*, vol. 102, no. 8, pp. 605–608, 1997.

[11] H. Pan, Y. Zhang, V. B. Shenoy, and H. Gao, "Ab initio study on a novel photocatalyst: functionalized graphitic carbon nitride nanotube," *ACS Catalysis*, vol. 1, no. 1, pp. 99–104, 2011.

[12] K. Momma and F. Izumi, "VESTA 3 for three-dimensional visualization of crystal, volumetric and morphology data," *Journal of Applied Crystallography*, vol. 44, no. 6, pp. 1272–1276, 2011.

[13] S. Plimpton, "Fast parallel algorithms for short-range molecular dynamics," *Journal of Computational Physics*, vol. 117, no. 1, pp. 1–19, 1995.

[14] A. Kinaci, J. B. Haskins, C. Sevik, and T. Cagin, "Thermal conductivity of BN-C nanostructures," *Physical Review B*, vol. 86, no. 11, pp. 1–8, 2012.

[15] B. Mortazavi, G. Cuniberti, and T. Rabczuk, "Mechanical properties and thermal conductivity of graphitic carbon nitride: a molecular dynamics study," *Computational Materials Science*, vol. 99, pp. 285–289, 2015.

[16] L. Yang, C.-Z. Wang, S. Lin et al., "Thermal conductivity of TiO_2 nanotube: a molecular dynamics study," *Journal of Physics: Condensed Matter*, vol. 31, no. 5, Article ID 055302, 2019.

Hindawi
Advances in Condensed Matter Physics
Volume 2021, Article ID 2370816, 9 pages
https://doi.org/10.1155/2021/2370816

Research Article

Density Functional Theory Study on the Effect of Isomorphic Substitution of FAU Molecular Sieve on N_2 Adsorption Performance

Mengya Wang,[1,2,3] Rong Cao,[1,2,3] Jiezhen Xia,[1,2,3] Luchao Zhao,[1,2,3] Yong Li,[1,2] Qimi Ciren,[4] Dongye Zhao,[1,2] Shifeng Wang,[1,2,3] Chun Du ,[1,3] and Qi Wu [1,2,3]

[1]*Department of Physics, School of Science, Tibet University, Lhasa 850000, China*
[2]*Institute of Oxygen Supply, Center of Tibetan Studies (Everest Research Institute), Tibet University, Lhasa 850000, China*
[3]*Key Laboratory of Cosmic Rays (Tibet University), Ministry of Education, Lhasa 850000, China*
[4]*Tibet Autonomous Region Energy Research Demonstration Center, Lhasa 850000, China*

Correspondence should be addressed to Chun Du; duchun@utibet.edu.cn and Qi Wu; wuqi_zangda@163.com

Received 8 September 2021; Accepted 7 October 2021; Published 22 October 2021

Academic Editor: Shuyuan Xiao

Low pressure and anoxia are the main characteristics of the environment in the Tibetan Plateau, which means people living there have a large demand for oxygen to reduce the symptoms of altitude sickness. Pressure swing adsorption (PSA) is a competitive oxygen production technology in plateau areas, which relies on the molecular sieves for the separation of N_2 and O_2 in industry and portable medical equipment. The adsorption characteristics of the Faujasite-type (FAU) molecular sieves, as one kind of the most widely used adsorbents for O_2 production, depend on the properties, amount, and distribution of the skeleton cations and atoms. In this paper, we explore the isomorphic substitution effect on the adsorption properties of N_2 in FAU molecular sieves using the computational approaches based on the density functional theory (DFT). The structural analysis and adsorption energy calculated for the Zn, Ca, and Ga substitutions at the Si/Al skeleton sites in the β-cage structure, the basic unit of FAU molecular sieves, prove that the isomorphic substitution effect can strengthen the adsorption of N_2. The Bader charge and density of states analysis validate the formation of electron-deficient holes near the Fermi level and hence strengthen the local polarity of the pore structure and enhance the adsorption of N_2 molecules. The work about isomorphic substitution on the FAU molecular sieves might provide an insight into heteroatom isomorphic modification mechanisms and designing excellent air separation materials.

1. Introduction

The plateau area of China accounts for more than one quarter of the total area of country and has an important strategic military affairs status [1]. The air pressure in Qinghai Tibet Plateau is low (i.e., the air pressure at 5500 m is half less than that in plain area) and the temperature difference between day and night is large. Hypobaric hypoxia has become the main characteristic of plateau environment [1]. According to the relevant research of neuroimaging, high-altitude environment will have a significant impact on the human brain [1]. Hypoxia can cause vomiting, fever, dizziness, and other different symptoms [2]. Therefore, in order to ensure the survival of people in these areas, there is a great requirement for oxygen (O_2) [3]. Research shows that, in oxygen-enriched environment, it can significantly reduce altitude reaction and sleep difficulty [4]. Therefore, it is very important to create an oxygen-enriched environment to effectively improve cognitive function [5].

The method of separating oxygen (O_2) and nitrogen (N_2) from air has aroused widespread interest in the pharmaceutical and chemical industries. Conventionally, the oxygen production technologies can be classified into physical oxygen production and chemical oxygen production methods. The physical methods of oxygen production are mainly air

separation, distillation, and compression (including pressure swing adsorption, membrane separation, and low-temperature distillation). Chemical oxygen production methods include water electrolysis, superoxide, and sodium chlorate oxygen candles. Pressure swing adsorption (PSA) technology using specific adsorbents is very competitive in the realization of air oxygen enrichment [6–8]. This method has many advantages, such as short start-up time, handy start-up and end-up, low energy expenditure, and low cost [9–11]. In view of the special oxygen demand in plateau areas such as China's Qinghai Tibet Plateau, some experts pointed out that PSA is the most economical and suitable technology. Pressure swing adsorption technology is based on the molecular characteristics of gas components and affinity for adsorption materials, under pressure to separate some gas components from the gas mixture technology. The process was carried out at a temperature close to the ambient temperature. Under high pressure, adsorbent is used to adsorb target gas. The common adsorbents are zeolite molecular sieves, activated carbon, and other special adsorption materials. Then, in order to desorb the adsorbed material, the process turns to low pressure.

Pressure swing adsorption (PSA) technology can realize the separation of O_2 on a lesser scale. Adsorbents are very important for PSA in industry and portable medical equipment. Generally speaking, in air separation, two types of the common adsorption processes were divided. The first process is to use zeolite molecular sieves as nitrogen adsorbent under the conditions of equilibrium. Oxygen is a process product because the quadrupole moment of nitrogen is higher than that of oxygen. The second method is to use carbon molecular sieves (CMSs) as oxygen adsorbents. Zeolite molecular sieves are a kind of major inorganic crystal materials extensively used in chemical industry, catalyst, adsorbent, ion exchange, and other fields. In air separation, because the quadrupole moment of nitrogen is higher than that of oxygen and the force between cation and N_2 in the adsorbent is greater than O_2, the equilibrium adsorption capacity of N_2 is higher than that of O_2. Therefore, zeolite molecular sieve can selectively adsorb nitrogen rather than oxygen and provide oxygen close to pure oxygen. Molecular sieve is a three-dimensional framework structure with ordered micropores with diameter of 2 nm. It has a variety of structures. The main reason is that the T atoms (tetrahedron) in the lattice have different connection ways. The common T atoms are silicon and aluminum. Zeolite molecular sieves have the advantages of low cost, high stability, and easy ion exchange. At the same time, they can adjust the gas-solid interaction by selecting the appropriate ratio of silicon to aluminum. The Linde type-A (LTA) and Faujasite-type (FAU) molecular sieves are the most widely used adsorbents for O_2 production [12, 13]. Due to the large temperature difference in plateau environment, FAU molecular sieves usually have higher N_2–O_2 selectivity than LTA molecular sieves in PSA process. FAU molecular sieves are composed of Si, Al, and O atoms, and their crystal composition changes with the change of Si/Al ratio. FAU molecular sieves are composed of sodalite gabions connected by hexagonal prism. Their properties depend on the properties, amount, and distribution of the skeleton cations and atoms. Ion exchange modification [14], dealumination modification [15], heteroatom isomorphic replacement modification, and pore modification [16] can change the structure of molecular sieves and affect their performance.

Heteroatom isomorphic substitution modification can introduce specific nonmetal or metal atoms into the original framework of molecular sieves to change the redox performance and catalytic activity of molecular sieves and avoid the possible problems of loss of active species and blockage of micropores by nonframework species [17]. Isomorphic substitution refers to the substitution of the T atom (tetrahedron) in the molecular sieves lattice [18]. The isomorphic substitution modification method is widely used in ZSM-5 [19], SBA-15 [20], UTL [21], and other kinds of molecular sieves. The commonly used metals in this modification include Zn [19], Ga [22], Ca [19, 23], Fe [19, 21], and Cr [18, 24]. Among them, the metals Zn, Ca, and Ga have been widely used in the modification of molecular sieves. For example, El-Malki et al. [25] introduced Zn, Ga, and Fe into the HZSM-5 cavity to study acidic sites through sublimation. The study found that, after sublimation, the concentration of Bronsted acid site is low, but, for Ga/ZSM-5 and Fe/ZSM-5, it increases again after hydrolysis. Miyake et al. [26] studied the direct and selective conversion of methanol to para-xylene over the zinc ion-doped ZSM-5/silica molecular sieve-1 core-shell zeolite catalyst. The study found that the p-xylene yield of this catalyst was 40.7 C-mol%, and the para-selectivity was higher than 99 C-mol%. Li et al. [27] used calcium doped biosilica to control bleeding and found that Ca-biosilica is expected to be a fast hemostatic agent due to its effectiveness, excellent biocompatibility, and simple and environmentally friendly preparation process. Liu et al. [28] studied Ga-doped ZSM-22 zeolite as a highly selective and stable catalyst for the isomerization of n-dodecane. The study found that Ga-substituted zeolite has high crystallinity, uniform morphology, and open pore structure. Similar to the zeolites discussed above, Al and Si atoms in FAU molecular sieves can also be replaced by metals. Although a lot of studies have been done on the properties of isomorphic substituted molecular sieves, we still do not know much about how to change the structure and electronic properties of framework atoms after the introduction of heteroatoms, so as to affect their adsorption properties. In particular, there are few reports on nitrogen adsorption in isomorphic FAU molecular sieves, and it is necessary to study FAU molecular sieves as an important catalyst for air separation.

In this work, the energetics of Zn, Ca, and Ga substitution for Si/Al skeleton atoms in FAU molecular sieves have been investigated based on the density functional theory (DFT), by predicting the substituting effect on the adsorption properties of N_2 molecule. We introduce the metal atoms of Zn, Ca, and Ga into β-cage structure which is the basic unit of FAU molecular sieves. Our simulated results reveal that the pore structure has different degrees of relaxation when the skeleton atoms are replaced by metal atoms of Zn, Ca, and Ga; and the isomorphic substitution of skeleton atoms can enhance the adsorption of N_2 molecule.

Our work aims to explore the substitution effect and modification mechanism of isomorphic substitution of metal atoms from the perspective of theoretical prediction, so as to improve the adsorption activity of molecular sieves. This theoretical arithmetic based on computational science has turned out to be a feasible and efficient method to achieve this goal. In addition, we hope that our results can provide guidance for further experimental research in the field of molecular sieves.

2. Calculation Method and Theoretical Models

Density functional theory (DFT) is calculated by using the plane-wave basis in the Vienna ab initio simulation package (VASP) [29]. The core and valence electrons were treated by the projector augmented plane-wave (PAW) method [30]. The generalized gradient approximation (GGA) with the Perdew-Burke-Ernzerhof (PBE) functional was used to represent the exchange-correlation energy [31]. The van der Waals (vdW) interaction is described by using the DFT-D3 method for all calculations. All atoms were fully optimized until the magnitude of the Hellmann-Feynman force and energy on every atom converged to less than 0.2 eV/Å and 10^{-5} eV, respectively. The cutoff energy was set to 400 eV for the plane-wave basis set. The Brillouin zone (BZ) was sampled by a Monkhorst-Pack $1 \times 1 \times 1$ k-point sampling grid for the β-cage structures.

The lattice constant of the FAU molecular sieve structure model was $a = b = c = 25.028$ Å, belonging to Fd3m space group of hexagonal system. As shown in Figure 1(a), the structural unit of the FAU skeleton was the β-cage. Adjacent β-cages were connected by hexagonal columns to form a system of holes and cavities. The holes and cavities are formed by silicon oxygen tetrahedrons and aluminum oxygen tetrahedrons, which are connected by oxygen bridge bonds. Due to the limited computational resources, the β-cage structure of the FAU structural unit (Figure 1(b)) was intercepted from the whole FAU framework in the calculation. The β-cage structure contains 24 Al atoms, 24 Si atoms, and 72 O atoms, making it a multielectron system with nonzero charge. Through analysis, the Si, Al, and O Bader charges were 1.73, 0.62, and 7.63$|e|$, respectively. As Figure 1(c) shows, the Al atoms lose outer electrons, and Si and O atoms have electron localization.

The N_2 molecular adsorption energy (E_{ads}) is calculated as follows:

$$E_{\text{ads}} = E_{N_2/\text{FAU}} - E_{\text{FAU}} - E_{N_2}, \tag{1}$$

where E_{ads} represents the adsorption energy, $E_{N_2/\text{FAU}}$ is the total energy after the adsorption of N_2 molecules in the β-cage channel of FAU, E_{FAU} is the total energy of the intercepted β-cage, and E_{N_2} is the energy of N_2.

3. Results and Discussions

3.1. Structural Properties. To study the effect of isomorphic substitution on the adsorption properties of FAU molecular sieves, Zn, Ca, and Ga atoms were used to replace the Al or Si atoms in the β-cage of FAU molecular sieves, respectively. The β-cage structure is composed of eight-membered rings and twelve-membered rings containing Si-O-Al. There are two kinds of Al and Si skeleton atoms at different positions, as shown in the dotted box in Figure 1(b). One kind contains Al and Si atoms that connect with two eight-membered rings, and the other kind contains Al′ and Si′ atoms that connect with the eight-membered rings and twelve-membered rings. The Zn, Ca, and Ga atoms are incorporated into the β-cage and replace the two kinds of Al and Si atoms, respectively. The optimized structures of the Zn, Ca, and Ga substitutions of the Al and Si atoms in the β-cage are shown in Figures 2(a)~2(f), and the optimized structures of the substitution of Al′ and Si′ atoms are shown in Figures 2(g)~2(l). Therefore, in our simulations, we totally considered twelve hybrid structures and calculated their formation energies. Among all the hybrid structures, only three doping systems, that is, Zn-doping (Al), Ca-doping (Al), and Ca-doping (Si), have the negative formation energies of −4.12 eV, −1.22 eV, and −3.14 eV, respectively. The results indicate that the Zn and Ca atoms tend to substitute the skeleton Al atom; in contrast, the Ga atom is more easily to replace the skeleton Si atom. Hence, these three hybrid structures and the pristine β-cage were adopted in the following simulations for the adsorption properties analysis.

To manifest the structural changes before and after introducing Zn, Ca, and Ga in the framework of the β-cage, the root mean square (RMS) displacement formula was used to calculate the structural relaxation of the substitution position (Al/Si/Al′/Si′). The RMS displacement was calculated as follows:

$$r_{\text{RMS}} = \sqrt{\frac{1}{3}\sum_{i=1}^{3}\left(r_i - r_i^0\right)^2}, \tag{2}$$

where r_i^0 and r_i are the bond lengths of Al/Si-O in the undoped structure and Al/Si/Zn/Ca/Ga-O in the doped structure, respectively.

The calculated RMS displacement is shown in Table 1. Combined with Figure 2, it can be seen that the pore structure has different degrees of relaxation after the skeleton atoms (Al/Si/Al′/Si′) are replaced by Zn, Ca, and Ga atoms. It shows that doping will have a certain effect on the structure.

3.2. Adsorption Properties for the Pristine β-Cage. Four adsorption structures and adsorption energies of N_2 at β-cage channels were calculated. The calculated adsorption energy results are shown in Table 2. One can see from the table that the adsorption energies of the four sites are −0.69 eV, −0.49 eV, −0.44 eV, and −0.78 eV. The simulated results mean that N_2 can be adsorbed at the four adsorption sites with relatively small adsorption energies and low adsorption capacity. Figure 3 depicts the optimization model and the charge differential density diagram of N_2 adsorbed on the pristine β-cage. According to the RMS displacement displayed in Table 2, N_2 can be adsorbed in the β-cage channel, leading to very tiny structural relaxation in the pore. Based

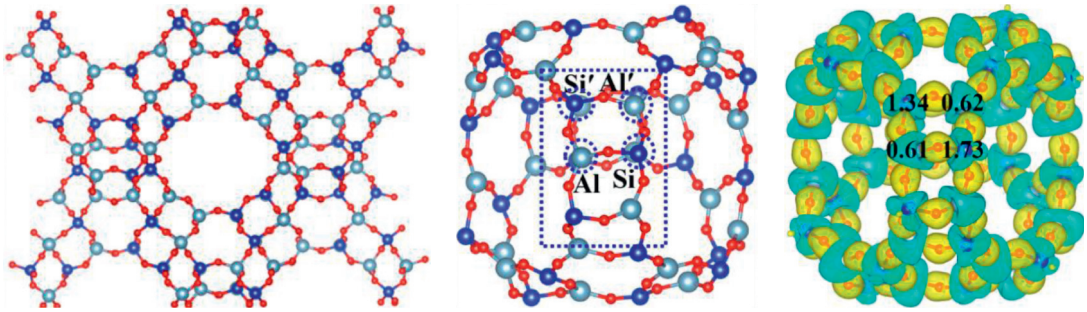

Figure 1: (a) Structure of the FAU molecular sieves. (b) Structure of the β-cage. (c) Charge difference diagram of β-cage. The isosurface value is 0.002 e Bohr^{-3}. The cyan part represents an increase in charge density, and the yellow part represents a decrease in charge density. Red, dark blue, and light blue represent the O, Al, and Si atoms.

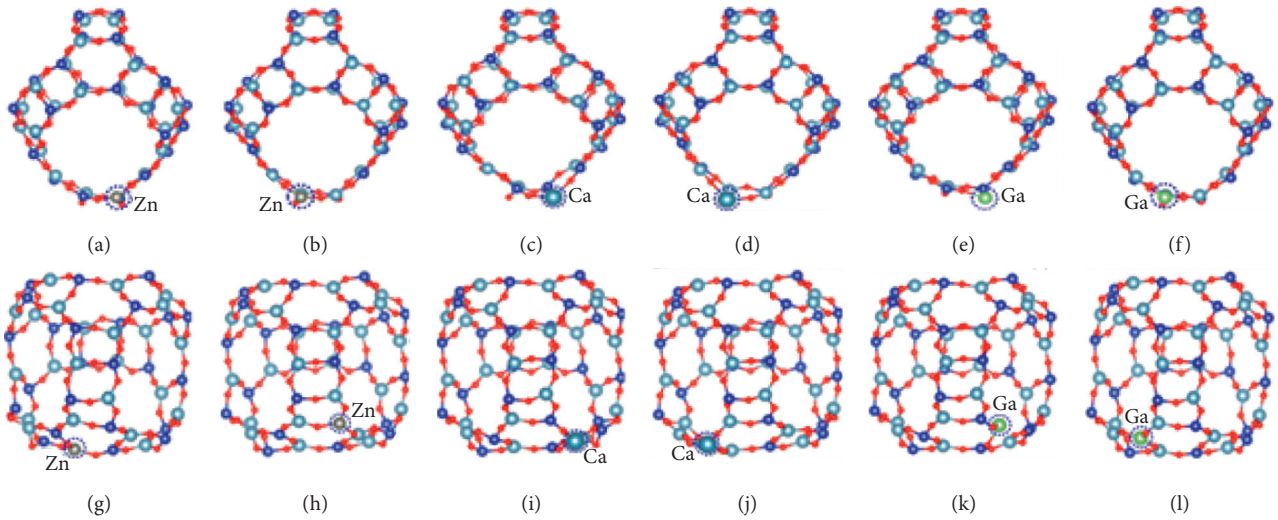

Figure 2: Structure diagrams of Zn, Ca, and Ga substitutions at Al, Si, Al′, and Si′. (a, c, e) Zn/Ca/Ga substitutions at Al site; (b, d, f) Zn/Ca/Ga substitutions at Si site; (g, i, k) Zn/Ca/Ga substitutions at Al′ site; (h, j, l) Zn/Ca/Ga substitutions at Si′ site.

Table 1: Calculated lattice constants, lengths of Al/Si/Zn/Ca/Ga-O bonds, and r_{RMS} of the different substituted atoms in the Zn/Ca/Ga-doped β-cage and pristine β-cage after optimization.

	Lattice constants/Å	Bond length (Si-O)/Å	Bond length (Al-O)/Å	Bond length (Zn/Ca/Ga–O)/Å	r_{RMS}/Å
Pristine (Al, Si)	25.028	1.661	1.706	—	—
Pristine (Al′, Si′)	25.028	1.618	1.721	—	—
Zn-doping (Al)	25.028	1.601	1.747	1.880	0.11
Zn-doping (Al′)	25.028	1.625	1.762	1.911	0.12
Zn-doping (Si)	25.028	1.585	1.757	1.913	0.15
Zn-doping (Si′)	25.028	1.602	1.750	1.912	0.18
Ca-doping (Al)	25.028	1.591	1.736	2.150	0.26
Ca-doping (Al′)	25.028	1.623	1.770	2.181	0.27
Ca-doping (Si)	25.028	1.645	1.715	2.213	0.32
Ca-doping (Si′)	25.028	1.577	1.778	2.190	0.34
Ga-doping (Al)	25.028	1.604	1.725	2.238	0.31
Ga-doping (Al′)	25.028	1.607	1.715	2.130	0.24
Ga-doping (Si)	25.028	1.635	1.708	1.788	0.08
Ga-doping (Si′)	25.028	1.657	1.710	1.785	0.10

on the Bader charge analysis, the average valence charges for the four skeleton atoms (Al/Al′/Si/Si′) are 0.61 eV, 0.62 eV, 1.73 eV, and 1.34 eV, respectively. After interaction with the N_2 molecule, the corresponding average valence charges for the four skeleton sites (Al/Al′/Si/Si′) change to 0.58 eV, 0.62 eV, 1.61 eV, and 1.43 eV, exhibiting that there is no

Table 2: Calculated lengths of the Al/Si-O bonds and r_{RMS} and E_{ads} before and after N_2 adsorption at the Al/Si/Al′/Si′ sites of the pristine β-cage.

Adsorption Site	Bond length (Al/Si-O)/Å (before adsorption)	Bond length (Al/Si-O)/Å (after adsorption)	r_{RMS}/Å	E_{ads}/eV
Pristine (Al)	1.661 1.706 1.706	1.641 1.704 1.701	0.012	-0.69
Pristine (Al′)	1.618 1.721 1.721	1.673 1.688 1.770	0.047	-0.49
Pristine (Si)	1.661 1.706 1.661	1.647 1.705 1.645	0.012	-0.44
Pristine (Si′)	1.618 1.721 1.618	1.672 1.698 1.602	0.035	-0.78

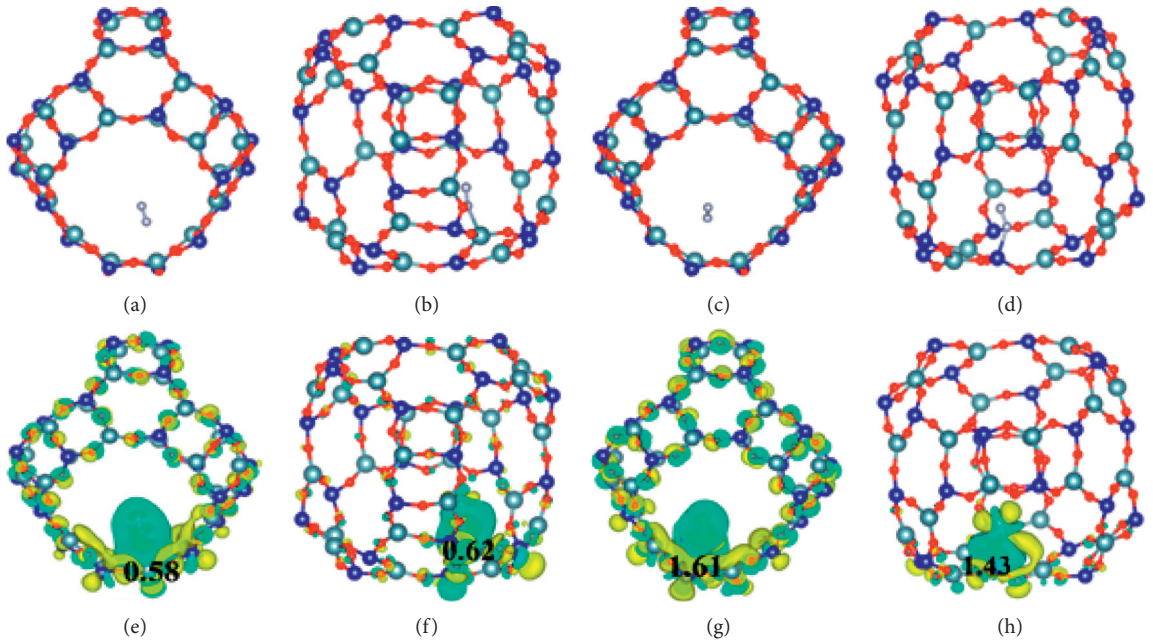

Figure 3: Adsorption structure and charge differential density diagram of N_2 adsorbed at the β-cage. Al (a, e), Al′ (b, f), Si (c, g), and Si′ (d, h) sites. The average valence charge of the adsorption site is shown in the figure; the isosurface value is 0.002 e $Bohr^{-3}$.

obvious charge transfer between the adsorption sites with N_2.

3.3. Adsorption Properties after Isomorphic Substitution. To reveal the effect of doping on N_2 adsorption, the adsorption energies of N_2 at the adsorption sites of the β-cage were calculated. We systematically considered five adsorption sites, containing the metal sites (Zn, Ca, and Ga) and their adjacent Al/Si and Al′/Si′ sites for each heteroatom doped structure and hence totally fifteen adsorption sites were simulated for the N_2 adsorption. All the stable optimized model and adsorption energies are provided in Figure 4 and Table 3, respectively. Other doped structures are not considered because the adsorption energy is very small and even close to zero. As Table 3 shows, the most stable adsorbable structure is based on the model of Zn and Ca substitutions at Al site and a Ga isomorphic substitution for Si atom. The adsorption centers are the Zn, Ca, and Ga heteroatoms and adjacent Al, Al′, Si and Si′ atoms. As seen, only six structures can adsorb the N_2 molecules with a negative adsorption energy: Zn substituting Al atoms, Ca substituting Al atoms, and Ga substituting Si atoms. For the structure with the isomorphic substitution of Al atoms with Zn, N_2 cannot be adsorbed at the Zn heteroatom site and the adjacent Al′ and Si′ sites with a very large and positive adsorption energy. In the case of the isomorphic substitution of Al atoms with Ca, only the Al′ site can adsorb N_2, while the other sites cannot adsorb N_2. When introducing Ga atoms into the β-cage, the N_2 molecule can be adsorbed at the Si, Si′, and Al′ sites near Ga atoms.

Compared with the pristine β-cage structure, the absorption energies of N_2 molecule are much larger for the isomorphic substitution of Si/Al atoms with the metal atoms Zn/Ca/Ga. Our calculated results reveal that the isomorphic substitution of the framework atoms by the metal atoms results in a much stronger interaction between the N_2 molecule and also the β-cage structure. The structure containing the isomorphic substitution of Zn for Al atoms has the largest absorption energy when N_2 is adsorbed at the Si site near the Zn atom. The charge differential density results reveal that there is obvious charge transfer between N_2 and the adsorption sites. Compared with Figure 3, the charge transferring between the Al′ and Si′ sites is relatively local due to a certain extent relaxation of the pore structure after metal atoms doping.

3.4. Electronic Structure Analysis. The projected density of states (PDOS) properties for the adsorption sites were

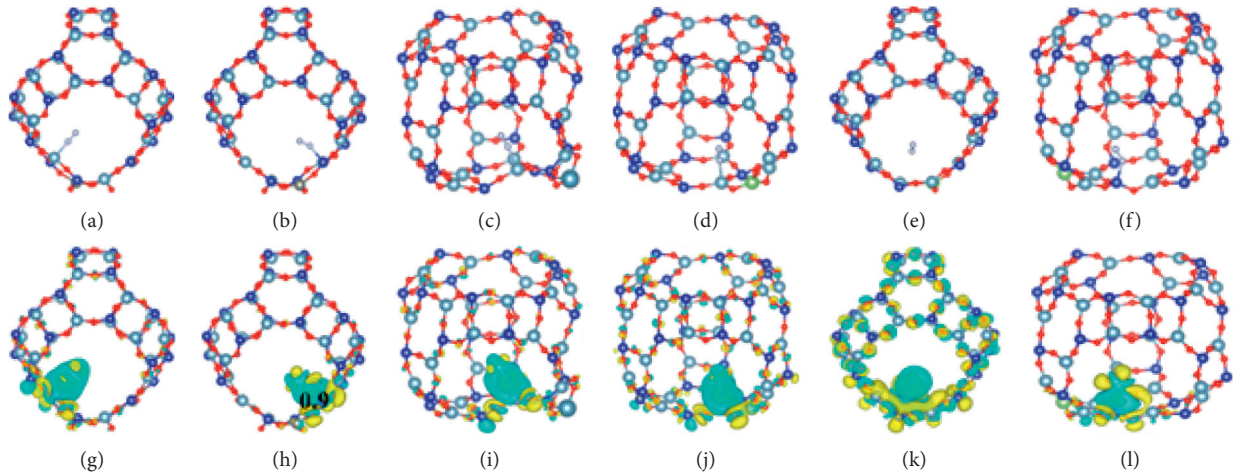

Figure 4: Structure models and charge difference density diagrams of N_2 adsorption at three kinds of doped β-cages that are optimized as the best adsorption sites: (a, g) Zn replaces Al (Al), (b, h) Zn replaces Al (Si), (c, i) Ca replaces Al (Al′), (d, j) Ga replaces Si (Al′), (e, k) Ga replaces Si (Si), and (f, l) Ga replaces Si (Si′). The average valence charge of the Si site after N_2 adsorption is shown in the figure; the isosurface value is 0.002 e $Bohr^{-3}$.

Table 3: Calculated lengths of Al/Si-O bonds and r_{RMS} and E_{ads} of N_2 adsorption at the Al/Si/Al′/Si′ sites of the doped β-cage.

Doping type	Adsorption site	Bond length (Al/Si/-O)/Å (before adsorption)	Bond length (Al/Si/-O)/Å (after adsorption)	r_{RMS}/Å	E_{ads}/eV
Zn-doping (Al)	Al (Zn)	1.601 1.747 1.737	1.651 1.774 1.748	0.033	−1.31
	Si (Zn)	1.601 1.747 1.590	1.648 1.764 1.608	0.031	−1.91
Ca-doping (Al)	Al′ (Ca)	1.650 1.767 1.736	1.713 1.721 1.743	0.042	−1.06
	Al′ (Ga)	1.635 1.708 1.708	1.643 1.704 1.715.	0.007	−1.14
Ga-doping (Si)	Si (Ga)	1.642 1.708 1.635	1.639 1.702 1.639	0.003	−0.83
	Si′ (Ga)	1.635 1.708 1.642	1.650 1.704 1.610	0.021	−0.94

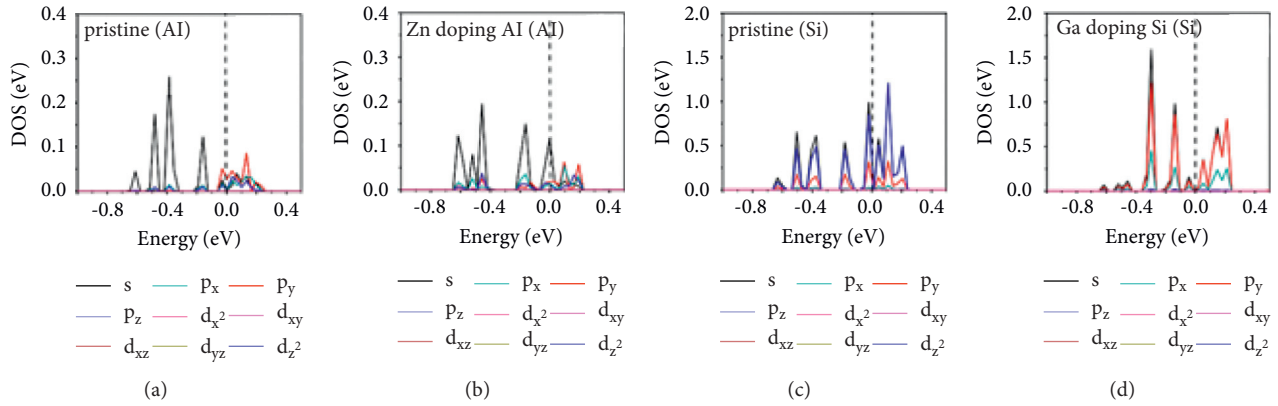

Figure 5: Continued.

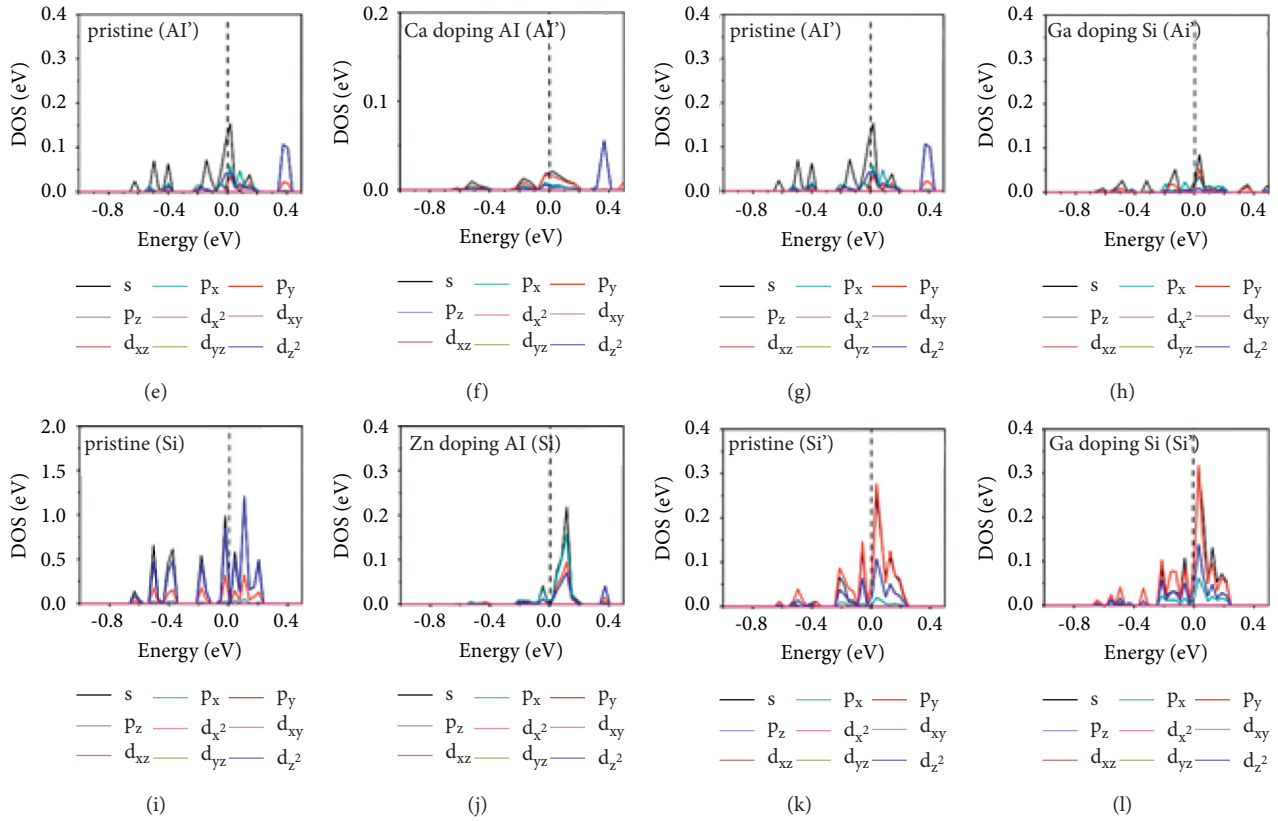

FIGURE 5: The projected density of states (PDOS) for the adsorption sites (Al/Al′/Si/Si′ atoms) in the pure β-cage and the relative adsorption sites in the Zn/Ca/Ga-doped β-cage. The dashed line shows the Fermi level.

calculated in order to comprehensively explore the substitution effect on the adsorption properties of β-cage structure. Figure 5 shows the density of states of the all the stable structures after N_2 adsorption. Compared with the DOS plots of the four adsorption sites on the pristine β-cage structure (Figures 5(a), 5(c), 5(e), 5(g), 5(i), and 5(k)), the density of states of all the adsorbable structures (Figures 5(b), 5(d), 5(f), 5(j), 5(h), and 5(l)) has significant changes. The DOS analysis results show that the number of electronic states near the Fermi level significantly decreases. As for metal materials, we know that the higher the electron density near the Fermi level is, the more active the free electrons it has. For the Zn-doped β-cage pore structure, the N_2 molecule on the adjacent Si atom has the largest adsorption energy. As Figure 5(d) shows, the number of electronic states for the Si site near the Fermi level almost decreases to zero. The Bader charge analysis of Zn-doping is calculated, which shows that the charge of the Si site decreases from 1.61 eV to 0.9 eV, forming electron-deficient holes. This result is attributed to the electron loss in the pore framework structure after Al^{3+} is replaced by Zn^{2+}, since the coordination of the metals does not match the substituted atoms. Therefore, Zn-doping leads to the formation of electron-deficient holes near Si sites as the electronic structure analysis results exhibit and thus enhances the local polarity of the pore structure and enhances the adsorption of N_2 molecules.

4. Conclusion

In summary, we introduce Zn, Ca, and Ga dopants into the FAU basic unit β-cage channel structure to activate the basal skeleton structure for air separation. Detailed calculations are carried out for the pristine β-cage and the Zn, Ca, and Ga substitutions at the skeleton Si/Al sites, which lead to the following conclusions: (1) The results showed that all the adsorption sites in the pure β-cage channel were very weak, especially for the Si site. The relative adsorption energy was only 0.44 eV. (2) The isomorphic substitution of Zn, Ca, and Ga on the pristine β-cage structure greatly enhances the adsorption of N_2 molecule. This is because electron loss appeared in the pore framework structure after the skeleton Si/Al atom was replaced by Zn/Ca/Ga, since the coordination of the metals does not match the substituted atoms. Therefore, the incorporation of Zn/Ca/Ga into the β-cage leads to the formation of electron-deficient holes at the adsorption sites and thus enhances the local polarity of the pore structure and enhances the adsorption of N_2 molecules. In the absence of relevant background, these findings provide molecular understanding, such as the influence of different heteroatom distribution, different adsorption structure, and other factors on the adsorption process and properties.

Data Availability

The data used to support the findings of this study are included within the article.

Conflicts of Interest

The authors declare that they have no conflicts of interest.

Acknowledgments

This work was financially supported by the National Natural Science Foundation of China (Grant no. 22168036) and Department of Education of Tibet Autonomous Region ([2021]1-21 Theoretical research and design of two dimensional electrocatalytic materials).

References

[1] X. Wei, X. Ni, S. Zhao, and A. Chi, "Influence of exposure at different altitudes on the executive function of plateau soldiers-evidence from ERPs and neural oscillations," *Frontiers in Physiology*, vol. 12, Article ID 632058, 2021.

[2] A. M. Luks, E. R. Swenson, and P. Bärtsch, "Acute high-altitude sickness," *European Respiratory Review*, vol. 26, no. 143, Article ID 160096, 2017.

[3] Y. Fu, Y. Liu, Z. Li et al., "Insights into adsorption separation of N_2/O_2 mixture on FAU zeolites under plateau special conditions: a molecular simulation study," *Separation and Purification Technology*, vol. 251, 2020.

[4] A. M. Luks, H. van Melick, R. R. Batarse, F. L. Powell, I. Grant, and J. B. West, "Room oxygen enrichment improves sleep and subsequent day-time performance at high altitude," *Respiration Physiology*, vol. 113, no. 3, pp. 247–258, 1998.

[5] Y. Liu, Z. Song, C. Song, and D. Wang, "A novel point source oxygen supply method for sleeping environment improvement at high altitudes," *Building Simulation*, vol. 14, pp. 1–18, 2021.

[6] S. P. Reynolds, A. D. Ebner, and J. A. Ritter, "Enriching PSA cycle for the production of nitrogen from air," *Industrial & Engineering Chemistry Research*, vol. 45, no. 9, pp. 3256–3264, 2006.

[7] J. C. Santos, P. Cruz, T. Regala, F. D. Magalhães, and A. Mendes, "High-purity oxygen production by pressure swing adsorption," *Industrial & Engineering Chemistry Research*, vol. 46, no. 2, pp. 591–599, 2007.

[8] A. M. M. Mendes, C. A. V. Costa, and A. E. Rodrigues, "Oxygen separation from air by PSA: modelling and experimental results: Part I: isothermal operation," *Separation and Purification Technology*, vol. 24, no. 1-2, pp. 173–188, 2001.

[9] R. S. Todd and P. A. Webley, "Pressure drop in a packed bed under nonadsorbing and adsorbing conditions," *Industrial & Engineering Chemistry Research*, vol. 44, no. 18, pp. 7234–7241, 2005.

[10] D.-K. Moon, Y. Park, S.-H. Kim, M. Oh, and C.-H. Lee, "Analysis of thermal parameter effects on an adsorption bed for purification and bulk separation," *Separation and Purification Technology*, vol. 181, pp. 95–106, 2017.

[11] A. M. Ribeiro, J. C. Santos, and A. E. Rodrigues, "PSA design for stoichiometric adjustment of bio-syngas for methanol production and co-capture of carbon dioxide," *Chemical Engineering Journal*, vol. 163, no. 3, pp. 355–363, 2010.

[12] W. Loewenstein, "The distribution of aluminum in the tetrahedra of silicates and aluminates," *American Mineralogist*, vol. 39, pp. 92–97, 1954.

[13] S. Calero, D. Dubbeldam, R. Krishna et al., "Understanding the role of sodium during adsorption. A force field for alkanes in sodium exchanged faujasites," *Journal of the American Chemical Society*, vol. 126, no. 36, pp. 11377–11386, 2004.

[14] X. Sheng, Y. Zhou, Y. Duan, Y. Zhang, and M. Xue, "Effect of different lanthanum source and preparation method on the lanthanum-doped mesoporous SBA-15 synthesis," *Journal of Porous Materials*, vol. 18, no. 6, pp. 677–683, 2011.

[15] W. T. Lim, S. M. Seo, O. S. Lee, L. Wang, and G. Q. Lu, "Synthesis and crystal structure of dehydrated, deaminated, and dealuminated zeolite Y (FAU): single-crystal structure of $|Na_{33}\ H_{26}\ (Al_5\ O_4\ )|[Si_{126}\ Al_{66}\ O_{384}\ ]$-FAU," *Journal of Inclusion Phenomena and Macrocyclic Chemistry*, vol. 67, no. 3-4, pp. 261–269, 2010.

[16] L. Tao, G.-S. Li, S.-F. Yin et al., "Synthesis and characterization of H-ZSM-5 zeolites and their catalytic performance in CH_3Br conversion to aromatics," *Reaction Kinetics, Mechanisms and Catalysis*, vol. 103, no. 1, pp. 191–207, 2011.

[17] G. Wang, H. Yuan, A. Kuang, W. Hu, G. Zhang, and H. Chen, "High-capacity hydrogen storage in Li-decorated $(AlN)_n$ ($n = 12, 24, 36$) nanocages," *International Journal of Hydrogen Energy*, vol. 39, no. 8, pp. 3780–3789, 2014.

[18] S. Ahmed, "Methanol to olefins conversion over metal containing MFI-type zeolites," *Journal of Porous Materials*, vol. 19, no. 1, pp. 111–117, 2011.

[19] K. Omata, Y. Yamazaki, Y. Watanabe, K. Kodama, and M. Yamada, "Artificial neural network (ANN)-aided optimization of ZSM-5 catalyst for the dimethyl ether to olefin (DTO) reaction from neat dimethyl ether (DME)," *Industrial & Engineering Chemistry Research*, vol. 48, no. 13, pp. 6256–6261, 2009.

[20] J. Ma, L.-S. Qiang, J.-F. Wang, X.-B. Tang, and D.-Y. Tang, "Effect of different synthesis methods on the structural and catalytic performance of SBA-15 modified by aluminum," *Journal of Porous Materials*, vol. 18, no. 5, pp. 607–614, 2010.

[21] M. V. Shamzhy, O. V. Shvets, M. V. Opanasenko et al., "Synthesis of isomorphously substituted extra-large pore UTL zeolites," *Journal of Materials Chemistry*, vol. 22, no. 31, p. 15793, 2012.

[22] X. Su, G. Wang, X. Bai et al., "Synthesis of nanosized HZSM-5 zeolites isomorphously substituted by gallium and their catalytic performance in the aromatization," *Chemical Engineering Journal*, vol. 293, pp. 365–375, 2016.

[23] R. Kawase, A. Iida, Y. Kubota et al., "Hydrothermal synthesis of calcium and boron containing MFI-type zeolites by using organic amine as structure directing agent," *Industrial & Engineering Chemistry Research*, vol. 46, no. 4, pp. 1091–1098, 2007.

[24] G. Wang, H. Chen, Y. Li, A. Kuang, H. Yuan, and G. Wu, "A hybrid density functional study on the visible light photocatalytic activity of (Mo,Cr)-N codoped $KNbO_3$," *Physical Chemistry Chemical Physics*, vol. 17, no. 43, pp. 28743–28753, 2015.

[25] E.-M. El-Malki, R. A. van Santen, and W. M. H. Sachtler, "Introduction of Zn, Ga, and Fe into HZSM-5 cavities by sublimation: identification of acid sites," *The Journal of Physical Chemistry B*, vol. 103, no. 22, pp. 4611–4622, 1999.

[26] K. Miyake, Y. Hirota, K. Ono, Y. Uchida, S. Tanaka, and N. Nishiyama, "Direct and selective conversion of methanol to para-xylene over Zn ion doped ZSM-5/silicalite-1 core-

shell zeolite catalyst," *Journal of Catalysis*, vol. 342, pp. 63–66, 2016.

[27] J. Li, J. Han, Q. Sun et al., "Biosynthetic calcium-doped biosilica with multiple hemostatic properties for hemorrhage control," *Journal of Materials Chemistry B*, vol. 6, no. 47, pp. 7834–7841, 2018.

[28] S. Liu, Y. He, H. Zhang et al., "Design and synthesis of Ga-doped ZSM-22 zeolites as highly selective and stable catalysts forn-dodecane isomerization," *Catalysis Science & Technology*, vol. 9, no. 11, pp. 2812–2827, 2019.

[29] G. Kresse and J. Furthmüller, "Efficient iterative schemes for ab initio total-energy calculations using a plane-wave basis set," *Physical Review B*, vol. 54, no. 16, pp. 11169–11186, 1996.

[30] G. Kresse and D. Joubert, "From ultrasoft pseudopotentials to the projector augmented-wave method," *Physical Review B*, vol. 59, no. 3, pp. 1758–1775, 1999.

[31] J. P. Perdew, K. Burke, and M. Ernzerhof, "Generalized gradient approximation made simple," *Physical Review Letters*, vol. 77, no. 18, pp. 3865–3868, 1996.

Hindawi
Advances in Condensed Matter Physics
Volume 2021, Article ID 2301222, 27 pages
https://doi.org/10.1155/2021/2301222

Review Article

Research Advance on the Sensing Characteristics of Refractive Index Sensors Based on Electromagnetic Metamaterials

Zongli Wang, Xin Wang, and Junlin Wang

College of Electronic Information Engineering, Inner Mongolia University, Hohhot 010021, China

Correspondence should be addressed to Xin Wang; wangxin219@imu.edu.cn and Junlin Wang; wangjunlin@imu.edu.cn

Received 10 May 2021; Revised 30 June 2021; Accepted 10 July 2021; Published 20 July 2021

Academic Editor: Shuyuan Xiao

Among different sensing platforms, metamaterials composed of subwavelength or deep subwavelength sized metal resonance elements arrays that are etched on semiconductor substrates or dielectric substrates exhibit excellent characteristics due to the strong localization and enhancement of resonance electromagnetic fields. As a new type of detection method, metamaterial sensors can break through the resolution limit of traditional sensors for a small amount of substance and have the advantages of high sensitivity, fast response, and simple measurement. Significant enhancement of the sensing characteristics of metamaterial sensors was realized by optimizing microstructures (single split-ring, double split-ring, nested split-ring, asymmetric split-ring, three-dimensional split-ring, etc.), using ultrathin substrates or low-index substrate materials, etching away local substrate, and integrating microfluidic channel, etc. This paper mainly reviews the research advance on the improvement of sensing characteristics from optimizing resonance structures and changing substrate materials and morphology. Furthermore, the sensing mechanism and main characteristic parameters of metamaterial sensors are introduced in detail, and the development trend and challenge of metamaterial sensing applications are prospected. It is believed that metamaterial sensors will have potential broader application prospects in environmental monitoring, food safety control, and biosensing in the future.

1. Introduction

Optical sensors have the advantages of high sensitivity, strong resistance to electromagnetic interference, low noise, high electrical and chemical stability, etc., so they have important applications in life science, food safety, chemical monitoring, and environment monitoring [1–5]. The generalized optical sensor can identify the measured substance or monitor the biomedical reaction process by detecting and analyzing the changes of lightwave intensity, phase, polarization, and other related information [6, 7]. The refractive index [8] is the most typical optical parameter. The real part of the refractive index affects the phase of the light wave, the imaginary part affects the intensity of the light wave, and its anisotropic distribution determines polarization and chirality. Generally, the optical refractive index sensor will introduce a resonance mechanism based on various optical effects to enhance the interaction between the light wave and the measured substance.

Metamaterials [9–12] are usually artificial electromagnetic materials composed of metal resonance elements arrays with subwavelength or deep subwavelength dimensions that are etched on semiconductor substrates or dielectric substrates according to specific rules. It has extraordinary physical properties that natural materials do not have and can control electromagnetic waves in a certain way. Metamaterials are sensitive to changes in the dielectric properties of the surrounding environment and have strong spectral characteristics for the local enhancement of the incident electromagnetic fields. When the dielectric properties (i.e., refractive index) of the surrounding environment change, the resonant characteristics (resonant amplitude, resonant frequency, phase, etc.) of the electromagnetic waves passing through the metamaterials will change accordingly. Therefore, by observing or measuring the changes, the detection of nonlinear substance around the metamaterials and the selection of a very small amount of objects to be tested can be achieved.

Metamaterial sensors [13–16] are optical sensors that can convert changes in the external refractive index into changes in optical signals. As a new type of detection method, metamaterial sensors can break through the resolution limit of traditional sensors, and have the advantages of high sensitivity, fast response, and simple measurement. In the past few decades, metamaterial sensors have made great progress in structural development and applications. Metamaterial sensors have the ability to restrict light to the nanoscale region and have high selectivity, making them have broad application prospects in the fields of environmental monitoring, drug discovery, food safety control, and temperature sensing.

Generally, the sensing characteristics of metamaterial sensors are significantly improved by optimizing microstructure and changing substrate material and morphology, which includes two main aspects, namely, improving sensitivity and improving quality factors. Improving the sensitivity of metamaterial sensors requires that the local field distribution of the resonant mode of the electromagnetic wave can overlap spatially to a greater extent with the substance being measured, that is, increasing the sensing area to enhance the interaction. Improving the quality factor of the metamaterial sensors requires lower losses in resonant mode.

The purpose of this article is to review the research advance on the sensing characteristics of metamaterial sensors. The basic principles, detecting processes, and sensing characteristics of various metamaterial sensors based on different microstructures and substrates are presented in detail, and the development trend and prospects of the metamaterials sensing technology are discussed. In addition, metamaterial sensors have potential applications in areas such as environmental sensing, homeland security, and biosensing.

2. Sensing Mechanism and Characteristic Parameters of Metamaterial Sensors

2.1. Sensing Mechanism. The operation principle of metamaterial sensors is based on the change in reflection and transmission coefficients (scattering parameters, S_{11} and S_{21}), which is induced in variation in the permittivity, permeability, or refractive index of the metamaterial resonator. The change in the dielectric constant around the sensor translates into a change in the electromagnetic signal spectrum in the form of an offset in the position of the resonance peak.

Metamaterials are artificial electromagnetic materials composed of arrays of subwavelength or deep subwavelength metal resonance elements fabricated on semiconductor substrates or dielectric substrates. The resonances are mainly divided into low-frequency resonances and high-frequency resonances. Low-frequency resonance can be understood as the coupling of capacitors and inductors, and resonant frequency can be expressed as follows [17]:

$$\omega_{LC} = (LC)^{-(1/2)} = \frac{1}{\sqrt{L}\sqrt{\varepsilon_0 \int {}^{\nu}\varepsilon(\nu)E(\nu)\mathrm{d}\nu}}. \quad (1)$$

As can be seen from formula (1), the resonant frequency is mainly determined by the inductance and capacitance. The inductance is mainly determined by the geometric parameters of metamaterials. If it is a nonmagnetic material, as long as the geometric parameters of the metamaterials are determined, the inductance will not change. The capacitance is related to the permittivity and electric field of the surrounding medium. As the permittivity of the surrounding environment changes, the overall capacitance will change, causing a change in the resonant frequency. For the change of electric field, high quality factor resonance and strong local field distribution can be realized by designing a special metamaterial structure, thereby improving the sensitivity of the sensor.

The high-frequency resonance of metamaterials can be understood as plasmon resonance, and its resonant frequency is expressed as follows [18]:

$$\omega_d \propto \frac{1}{\left(2d\varepsilon_{\mathrm{eff}}^{1/2}\right)}. \quad (2)$$

Here, d is mainly determined by the geometric parameters of the metamaterials, and $\varepsilon_{\mathrm{eff}}$ is the average permittivity of the environment. When the substance to be measured is connected to the metamaterial structure, it will cause the surrounding permittivity to change and then change the resonant frequency.

Since the metamaterial microstructure interacts with the substrate, and there is also capacitance between the substrate and the metamaterial microstructure, the change in the substrate also causes a shift in the resonant frequency of the metamaterials. The overall capacitance of the metamaterials can be expressed as follows [19]:

$$c = \sum_{i=1}^{4} c_i, \quad (3)$$

where c_1 is the capacitance of the substrate, c_2 is the capacitance between the substrate and the metamaterial microstructure, c_3 is the capacitance of the metamaterial microstructure itself, and c_4 is the capacitance between the metamaterial microstructure and the substance to be measured.

If the metamaterial microstructure is fabricated on a substrate with high resistance, high permittivity, and a relatively large thickness, c_1 contributes a lot to the overall capacitance, the capacitance change of the metamaterial itself is relatively small, and the sensitivity is correspondingly low. Therefore, reducing the relative contribution of the substrate, such as using a low permittivity, small absorption, and thin substrate, can also improve the sensitivity of the metamaterial sensors.

2.2. Characteristic Parameters. The sensing behaviors of metamaterial sensors are evaluated with well-known indicators, the quality factor Q, the sensitivity S, and the figure of merit FOM.

Assuming f_0 is the resonant frequency of the metamaterial sensor, it is very related to the structural parameters

of the metamaterial sensor and the external environment, so the weak refractive index disturbance Δn will bring the resonant frequency shift Δf. By detecting the change of resonant frequency through the spectrum analysis system, the information of the measured substance can be obtained. However, the spectrum analysis system has its hardware limitations in terms of weak signal detection and spectral resolution, so we need to optimize the design of the metamaterial sensor structure to achieve greater changes in Δf. Generally, the refractive index frequency sensitivity of the metamaterial sensor is defined as $S(f) = \Delta f/\Delta n$, where Δf represents the change in the resonant frequency of the metamaterial sensor and Δn represents the change in the refractive index of the substance to be measured. The unit of Δn is RIU (Refractive Index Unit), which represents the unit refractive index. However, because the sensitivity $S(f)$ of the metamaterial sensor is related to the working band, the normalized sensitivity $S(f)'$ is used to exclude the influence of the working band, which is defined as follows: $S(f)' = S(f)/f_0$.

Generally, the quality factor Q reflects the resonance characteristics of the sensor. That is, the sharper the resonance peak, the greater the corresponding value, and the higher the sensitivity of the sensor. In addition, the quality factor Q also determines the resolution of the sensor. The larger the value, the higher the resolution of the sensor. The quality factor of the sensor can be defined as follows: $Q(f_0) = f_0/\text{FWHM}$ (where f_0 is the resonant frequency of the metamaterial sensor and FWHM (Full Width at Half Maximum) is the half-height width of the resonance peak).

In order to make a more reasonable comparison of the characteristics of sensors working in different frequency bands, FOM (figure of merit) is usually used to describe the characteristics of the sensors. When the sensing sensitivity is the same, the larger the FOM and the better the sensing characteristics. Generally, FOM can be defined as FOM = S/FWHM, where S represents the refractive index frequency sensitivity of sensors and FWHM represents the half-height width of the resonance peak, that is, the sensing characteristics that guarantee both high sensitivity $S(f)$ and high quality factor Q is the best.

3. Research Advance in Improving the Sensing Characteristics of Metamaterial Refractive Index Sensors

Following the definition of FOM, the enhancement of the sensing capacity of metamaterial sensors can be considered from two aspects. One is to design metamaterial sensors with higher quality factor Q, while the other is to make the relevant, resonant frequency shift Δf with a larger step for the same surrounding changes. The first route is to optimize the metal resonance structures on the metamaterial surface to achieve high Q resonances, and in recent years, many novel resonance structures have been shown. Another route is to highlight the effects of changes in the surrounding dielectric by reducing substrate effects to achieve greater spectral modulation under the same surrounding dielectric changes.

3.1. Optimizing Metamaterial Structures. For metamaterials, a split-ring resonator (SRR) is the most commonly exploited topology. SRRs can be achieved by etching ring-shaped metal patterns with one or more opening gaps on the substrate surface, where the rings can be regarded as inductors, and the opening gaps can be regarded as capacitors. From the perspective of the equivalent circuit model, the SRR structure constitutes the LC oscillation circuit, and the resonant frequency is expressed as formula (1). The structural parameters of SRR determine the resonant frequency, which can be achieved at any frequency by proper selection. When the surrounding environment of the SRR changes, the equivalent capacitance and inductance corresponding to the SRR will be inevitably changed, which in turn will change the resonant frequency, so sensing can be achieved by detecting this change. In addition to SRR, metallic wires, with their simple shape, are often used as structural units in the composition of metamaterials. When the direction of the electric field of the incident electromagnetic wave is parallel to the wire, the positive and negative charges accumulate at each end of the wire, corresponding to a pair of electric dipoles. The alternating electric field causes a reciprocal movement of the charges inside the wire, so the wire is equivalent to a pair of oscillating dipoles under the electromagnetic field, and its resonant mode is dipole resonance, with the same resonant frequency as the applied electric field. Fano resonance is caused by the interference phase between a wider spectral line and a narrower discrete resonance cancellation or phase length, and Fano resonance has a higher Q-factor than dipole resonance and LC resonance.

In 2007, Driscoll et al. [18] successfully prepared tunable terahertz filters on a benzocyclobutene (BCB) film and a silicon (Si) particle film based on symmetric SRRs array metamaterial surface, and the mixed droplets of alcohol and nanosilicon spheres were coated on the surface of metamaterials. Observing the transmission spectrum of the metamaterials, it was found that its resonant frequency had changed, as shown in Figure 1(a). This is the first time that terahertz metamaterials are used in the field of sensing, which fully shows that such metamaterials can be used as sensors to detect biochemical samples with different dielectric properties. After that, metamaterials based on planar SRRs array were widely used in the field of sensing. Lee and Yook [20] applied planar SRRs metamaterials to biochemical detection for the first time in the microwave band and identified and detected avidin with a frequency shift of 40 MHz, as shown in Figure 1(b). Wu et al. [21] fabricated symmetric SRRs array on Si substrate and quartz substrate to construct terahertz metamaterial sensors. 50 μL streptavidin agarose (SA), biotin, octadecanethiol (ODT), and biotin were mixed to make a sample to be measured. The experimental detection of SA is realized based on the principle of resonant frequency movement measurement, as shown in Figure 1(c). Quartz-based metamaterials will produce two resonance peaks with a high-frequency resonant frequency of about 2 THz. After loading the sample to be measured, the resonance peak will have a frequency shift of 6.76 GHz and Q-factor of 8. As shown in Figure 1(d), in 2019, Han et al. [22] proposed a square SRRs metamaterial sensor based on

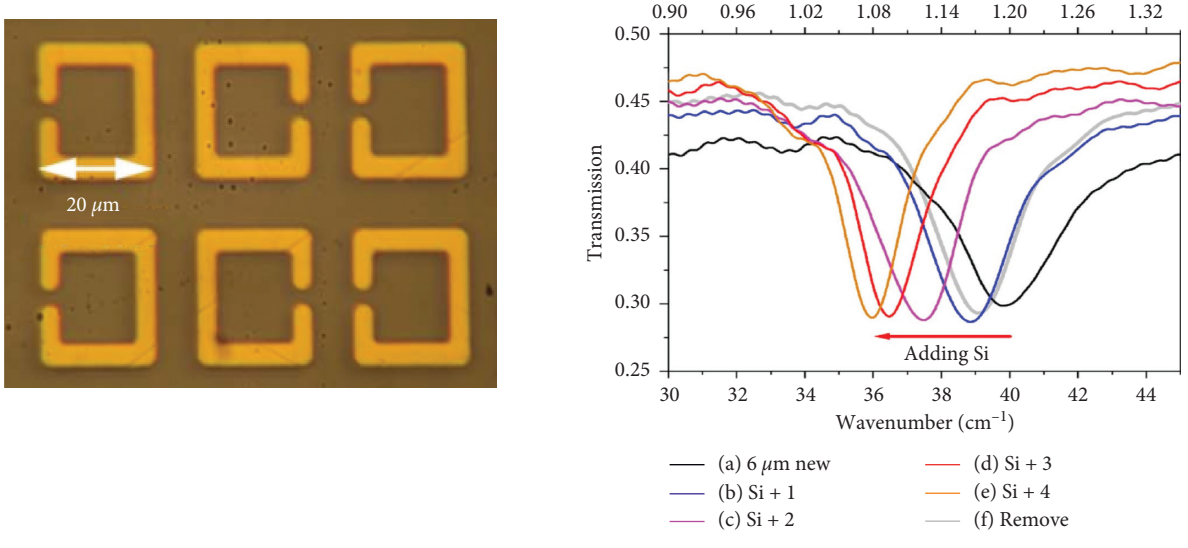

(a)

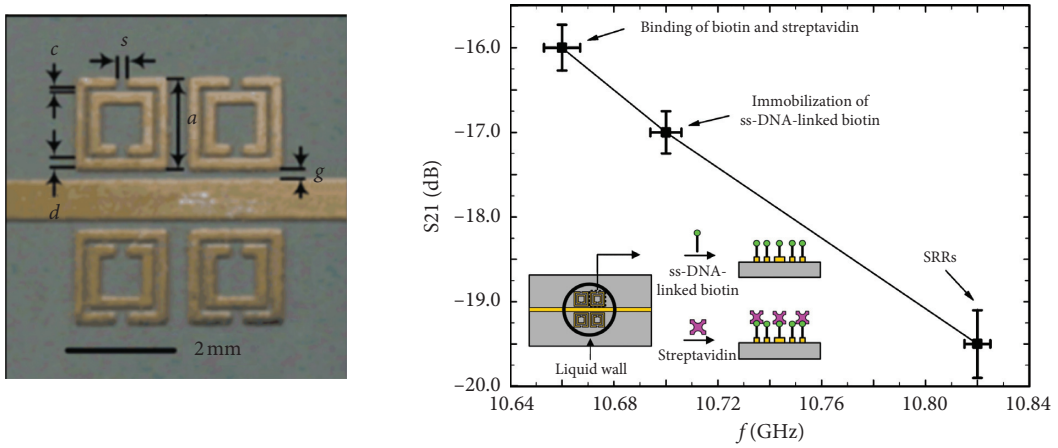

(b)

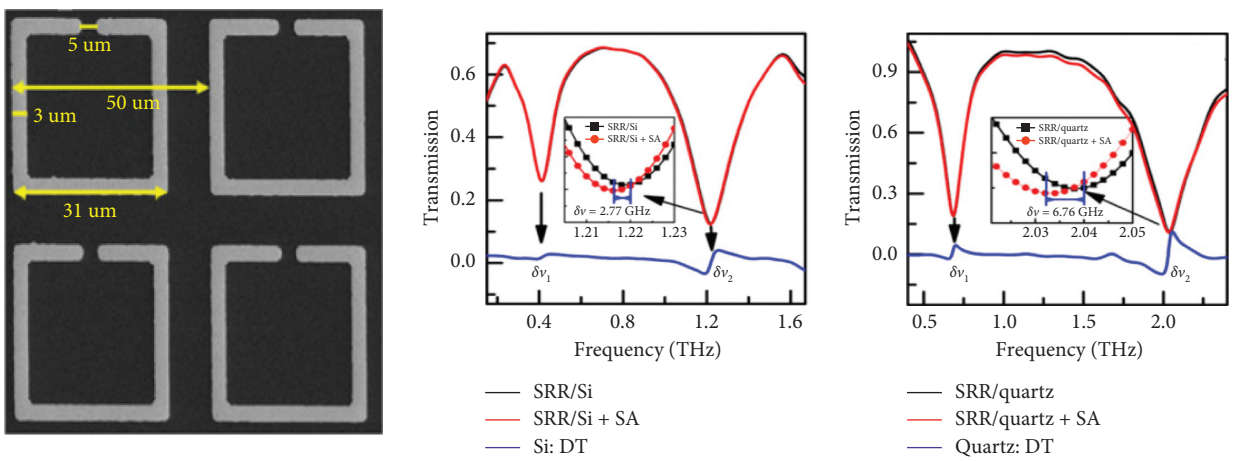

(c)

Figure 1: Continued.

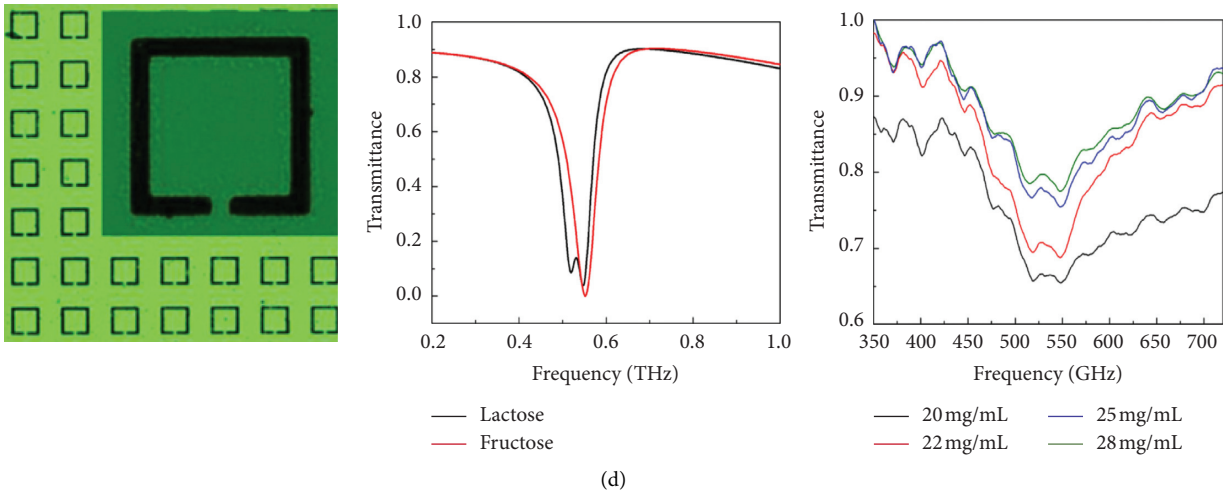

Figure 1: Schematic diagrams and transmission spectra of metamaterial sensors based on symmetric SRRs arrays. (a) Reproduced with permission from reference [18] copyright 2007, AIP publishing. (b) Reproduced with permission from reference [20] copyright 2008, AIP publishing. (c) Adapted with permission from reference [21] copyright 2015, Elsevier B.V. (d) Adapted with permission from reference [22] copyright 2018, Elsevier B.V.

resonant coupling for the fingerprint detection of lactose. The designed sensor in this work consisted of a periodic array of square-shaped copper SRRs on the top of a quartz substrate, which can achieve sensing detection of lactose concentration. It can be found from the research of these sensors that metamaterials based on SRRs structure can be used for substance detection, but the detection sensitivity is limited, and the sensing characteristics still need to be improved.

In pursuit of better sensing characteristics, such as higher quality factor Q, higher sensitivity and higher figure of merit FOM, dipole resonance, quadrupole resonance, Fano resonance, electromagnetic induced transparency (EIT)-like mode or trapped mode can be excited by metamaterials with asymmetric SRR structures. Breaking structural symmetry of metamaterial resonance structure is one of the common and efficient approaches to achieve such sharp resonances and improve sensing sensitivity.

Singh et al. [23] systematically studied the influence of the opening position of the asymmetric SRRs structure and the polarization of the incident waves. This asymmetric SRRs structure will produce three resonance mechanisms, namely LC resonance, dipole resonance, and quadrupole resonance. It is found that as the opening position is farther from the center of the SRRs, the quality factor Q resulted from quadrupole resonance is higher. In addition, Singh et al. also simulated the surface current distribution of the SRRs structure at the resonant frequency and found that the asymmetric SRRs structure has very weak electromagnetic field scattering when the quadrupole resonance occurs, which greatly reduces the energy coupled to the free space, and finally produces a very sharp resonance peak. It can be seen from Figure 2 that the quadrupole resonance has a resonance peak near 1.75 THz. When the electromagnetic wave is incident with horizontal polarization, the Q-factor can be as high as 95. Therefore, the quadrupole resonant

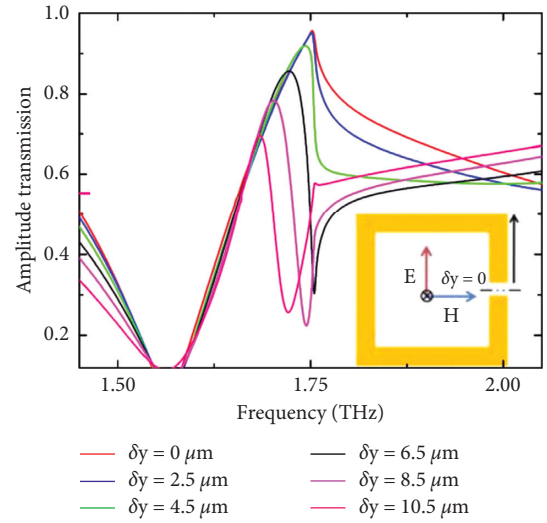

Figure 2: Transmission spectra of metamaterials based on asymmetric SRRs array; adapted with permission from reference [23] copyright 2010, Optical Society of America.

mode can achieve a good localization of the electromagnetic field and will provide new means for sensing applications.

Fano resonance has the advantages of sharp resonance profile, narrow resonance peak width, and strong localized field enhancement, so various Fano resonance metamaterial sensors based on asymmetric SRR structures have been proposed for high sensitivity refractive index sensing [24–26]. Debus and Bolivar [24] designed a double-opening asymmetric SRRs structure, as shown in Figure 3(a). For a perfect conductor material, the calculated Q-factor is as high as 40, and the electromagnetic field is localized around the double-opening SRRs.

When the substance with permittivity of 3.2 and thickness of 10 nm is deposited on the surface of the

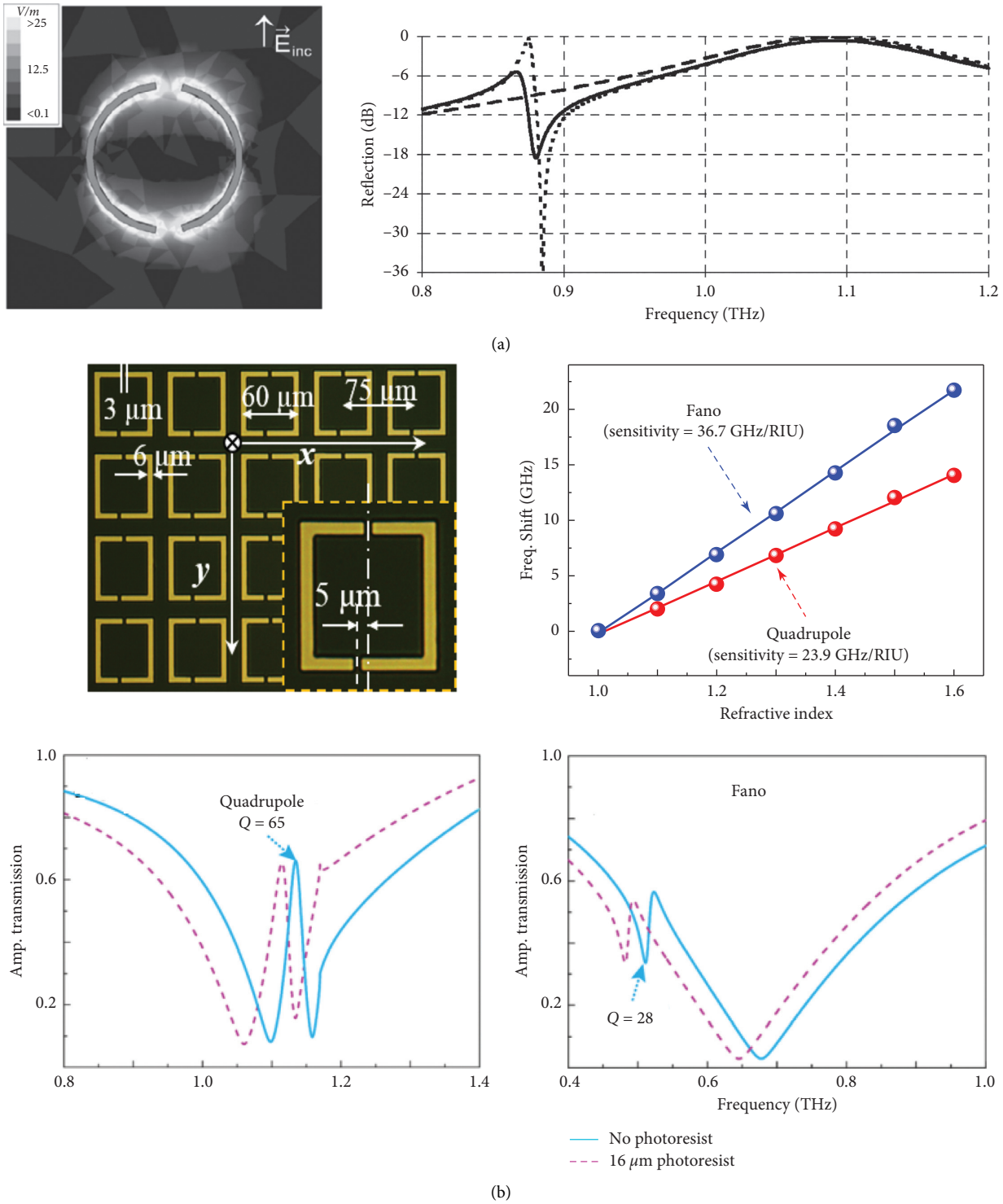

Figure 3: (a) Schematic diagrams and reflection spectra of metamaterial sensors based on double-opening asymmetrical SRRs arrays, reproduced with permission from reference [24] copyright 2007, AIP publishing. (b) Schematic diagrams and transmission spectra of metamaterial sensors based on double-opening asymmetrical SRRs arrays, reproduced with permission from reference [25] copyright 2014, AIP publishing.

metamaterial structure, it will cause the resonance peak at 867 GHz to shift by 5 GHz, which corresponds to $S = 6.3$ GHz/RIU. Singh et al. [25] analyzed the terahertz sensing characteristics of the Fano resonance and the quadrupole resonance in the double-opening asymmetric SRRs structure, as shown in Figure 3(b), the Q-factor of the quadrupole resonance is as high as 65, while the Q-factor of Fano resonance can also reach 28, which is much higher than

the Q-factor of the resonance peaks produced by the previous structures. When the thickness of the substance to be measured is kept at $4\,\mu$m, the Fano resonance can achieve maximum sensitivity of 36.7 GHz/RIU, while the quadrupole resonance can achieve a sensitivity of 23.9 GHz/RIU. In 2019, Behera and Kim [26] presented FDTD simulation studies of asymmetric 2D and 3D gold resonators for different applications of high sensitivity, high figure of merit, and circular dichroism polarization and incident angle-independent refractive index sensing, respectively. It is shown that the sensitivity of the triple C-shape asymmetric Fano resonant cavity is improved to 606 nm/RIU and the FOM of the quadruple C-shape resonant is as high as 16.5 and the polarization and angle of incidence are independent.

Although highly sensitive refractive index sensing based on metamaterial sensors can rely on a single-band Fano resonant frequency shift, the effect of environmental changes (e.g., temperature and humidity) on the frequency shift of the resonance cannot be ignored. As a result, relying on a single Fano resonance alone can easily introduce errors when used for sensing applications. Therefore, the research team is now focusing on the multiband Fano resonant frequency domain as a solution to reduce the sensing errors caused by environmental variations [27, 28].

Li et al. [27] demonstrated multiple Fano resonances in an integrated single dark-mode hybrid metamaterial waveguide structure consisting of three gold tangents placed on a dielectric plate waveguide, as shown in Figure 4(a). By breaking the structural symmetry, a quadrupole mode on the middle vertical cut wire is excited and further results in multiple Fano resonances through both the diffracted waves and near-field coupling with bright dark mode. A high Q-factor refractive index sensor with FOM of 330 and 281 is realized. This study provides a method for obtaining multiple high Q-factor Fano resonances that can broaden access for the fabrication of biochemical sensor devices. As shown in Figure 4(b), Kong et al. [28] proposed a multiple Fano resonant metamaterial refractive index sensor consisting of microcavities and microstructures. By fine-tuning the microcavity thickness and microstructure configuration, multiple Fano resonances can be generated for refractive index sensing: depending on the single Fano resonance, the sensitivity can reach 831 nm/RIU and the FOM of 600; in addition, the spectral spacing of the double Fano resonance can also be used for refractive index detection with a sensitivity of 194 nm/RIU, but with significantly reduced errors caused by environmental variations. Refractive index sensors based on multiple Fano resonances have the advantages of high sensitivity, narrow Fano resonance peaks, high ease of integration, and potential to reduce environmental errors, and are expected to provide a new strategy for optical refractive index sensing.

EIT [29] is a classical quantum interference effect that occurs in coherently driven atomic systems at multiple energy levels (triple or quadruple energy levels), where this interference alters the optical response of the atomic medium, creating a clear window of transparency within a wide absorption band. In 2008, Zhang et al. [30] introduced the concept of plasma-induced transparency (PIT) in metamaterials, and a variety of metamaterial structures have since been designed to simulate the EIT effect. PIT is an EIT-like metamaterial behavior that has attracted a great deal of attention due to its wide range of practical applications. Most EIT-like metamaterials are based on two resonant modes, bright and dark or superradiative and subradiative modes. In metamaterials, EIT-like phenomena can be modelled by destructive interference between the bright and dark modes and the superradiative and subradiative modes. For EIT-like phenomena to occur in metamaterials, the two modes should have close resonant frequencies and very different Q-factor [31].

Recently, EIT-like Fano resonances have been confirmed based on cut lines [30, 32, 33] and SRRs [34–37]. Due to the strong interference between two or more resonance modes, the EIT-like-Fano resonance structure has inherent sensitive properties to changes in the local environment. Because of the asymmetric line shape, small perturbations can cause significant spectral changes, including peak-frequency shifts and linewidth changes. This sensitive nature, therefore, makes metamaterials particularly attractive as biomedical and chemical sensing platforms because of their unique advantages, including nonlabelling, nondestructive, time-saving, and low cost compared to conventional bioassays.

However, the practical application of EIT-like metamaterials for biosensing has not yet been fully promoted. On the one hand, the small theoretical sensitivity of the existing biosensors and the single criteria for evaluating their performance make it difficult to apply them in practical engineering. On the other hand, the small variations in frequency shift and miniaturised manufacturing processes of most existing metamaterial biosensors hinder the widespread use of these biosensors in reality. In practice, it is ideal that the transparent window of the EIT phenomenon can be modulated arbitrarily. The corresponding modulation methods are passive modulation and active modulation. Jin et al. [38] designed a novel terahertz metamaterial structure consisting of a pair of subwavelength inverse U-shaped SRR resonators and tangential resonators to achieve the weak coupling region EIT effect. Theoretical and simulation results show that the EIT-like phenomena can be trimmed by modulating the relative coupling distance between the broken filaments and SRRs or the mutual distance between the SRR pairs, as shown in Figure 5. This method is a passive modulation, mainly achieved by changing the geometric parameters of the resonant cavity structure, but it is determined that each modulation requires a refabrication of the structure, which limits its practical application and increases the cost of the application. In addition, the introduction of photosensitive silicon cells in the dark-mode resonant cavity unit enables active optical control of the EIT-like effect by increasing the dark-mode damping rate.

Shen et al. [29] presented a tunable electromagnetically induced reflection effect with a high Q-factor based on a complementary bulk Dirac semimetal terahertz metamaterial structure. As shown in Figure 6, the design consists of a wire-slot structure and an SRR resonator slot structure, which act as a radiating and a subradiating unit, respectively. Destructive interference between these two elements

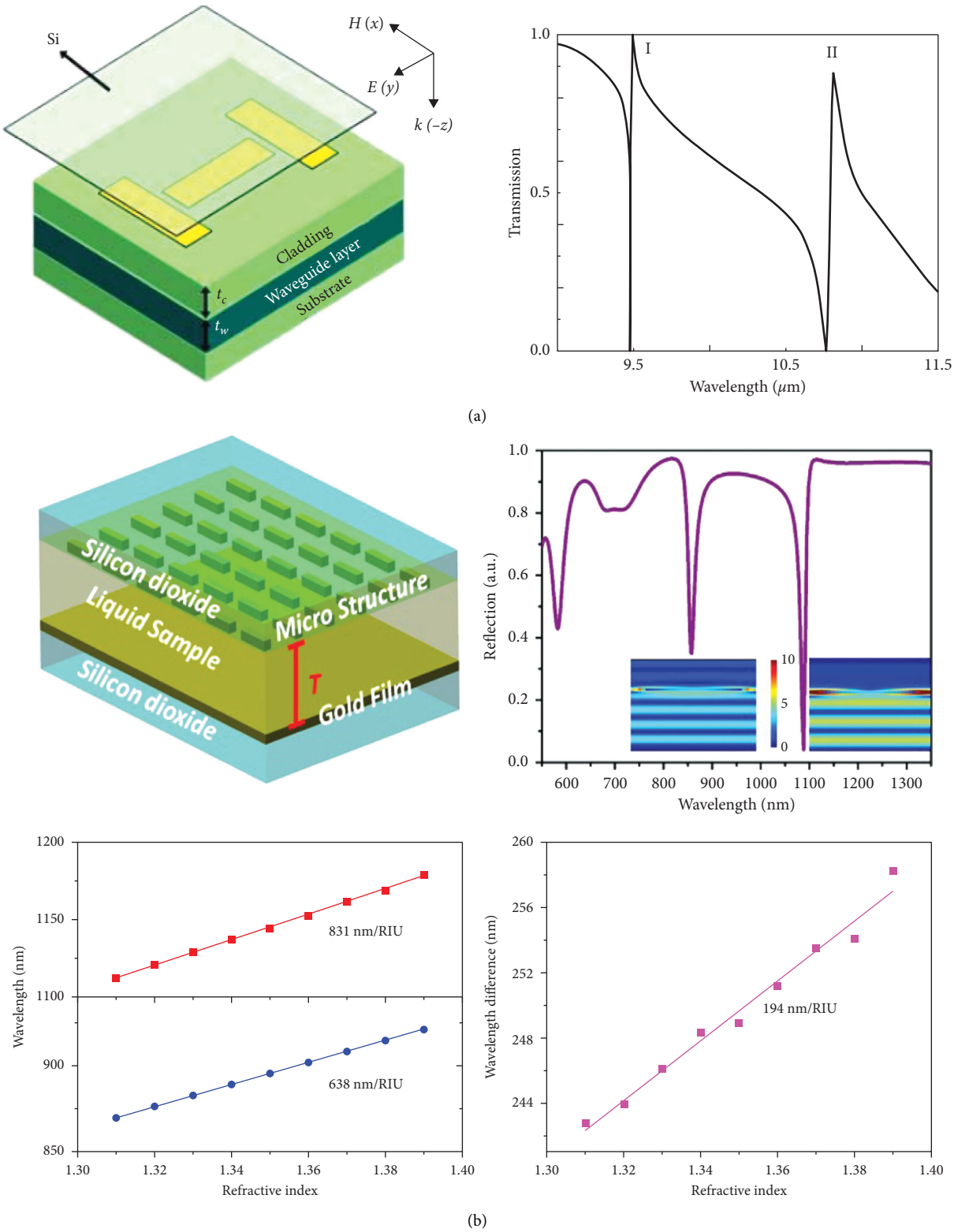

Figure 4: Schematic diagrams and transmission spectra of metamaterial sensors with multiple Fano resonances. (a) Reproduced with permission from reference [27] copyright 2018, IEEE. Schematic diagrams, reflection spectra, and sensitivity of metamaterial sensors with multiple Fano resonances. (b) Reproduced with permission from reference [28] copyright 2018, IEEE.

produces a reflection peak with a high Q-factor (~87.6), resulting in sensitive terahertz sensing, where the proposed bulk Dirac semimetallic sensor has a sensitivity of 302.5 GHz/RIU with a FOM of 19. This study provides an alternative approach to the design of terahertz ultrasensitive sensors, filters, and slow optical devices. The EIT-like

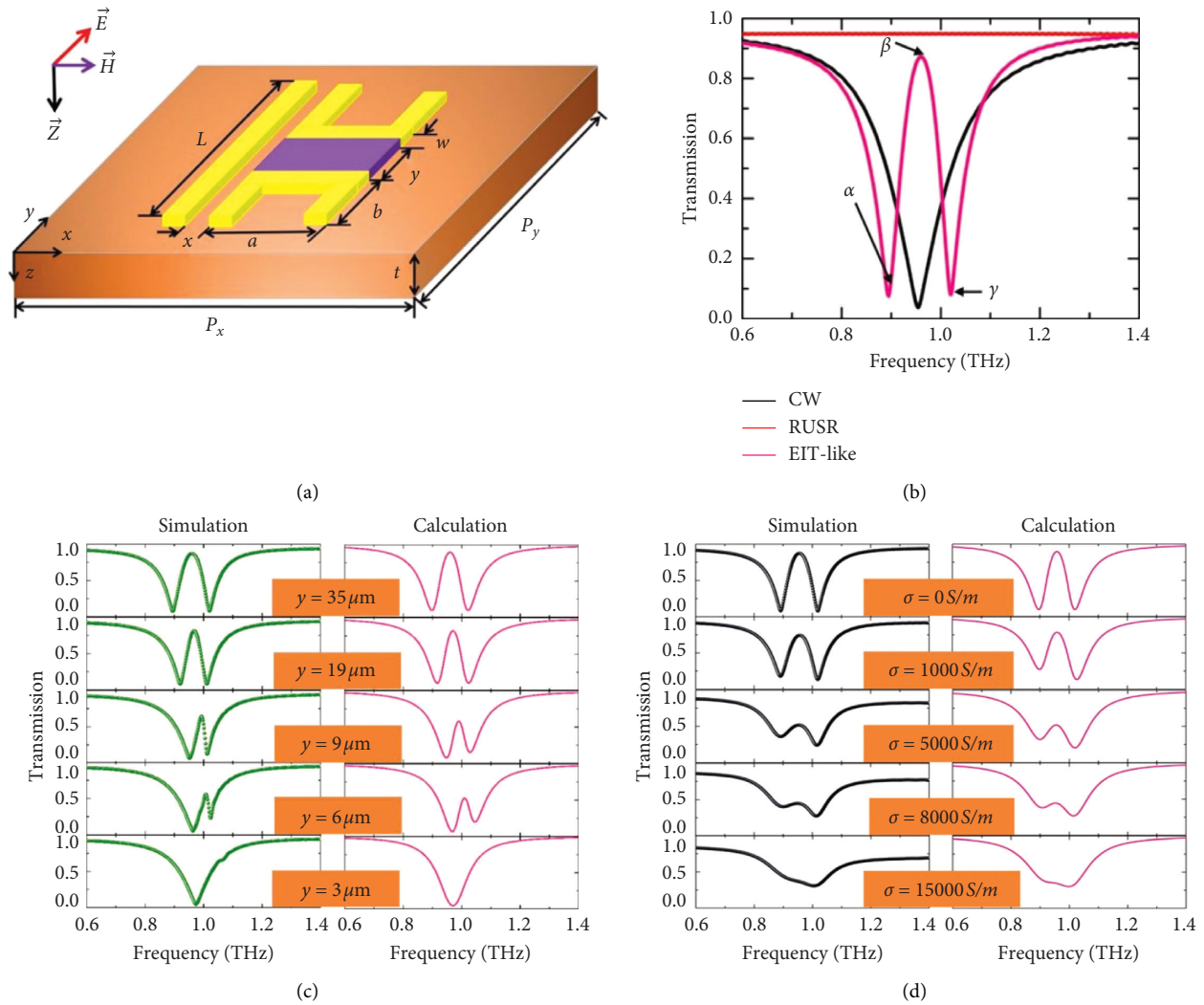

Figure 5: (a) Schematic diagram of EIT metamaterials. (b) Simulated transmission profile versus frequency. (c) Modulation of the transparent window when the coupling distance varies. (d) Transmission spectra at different silicon conductivities. (a–d) Reproduced with permission from reference [38] copyright 2019, Springer Nature.

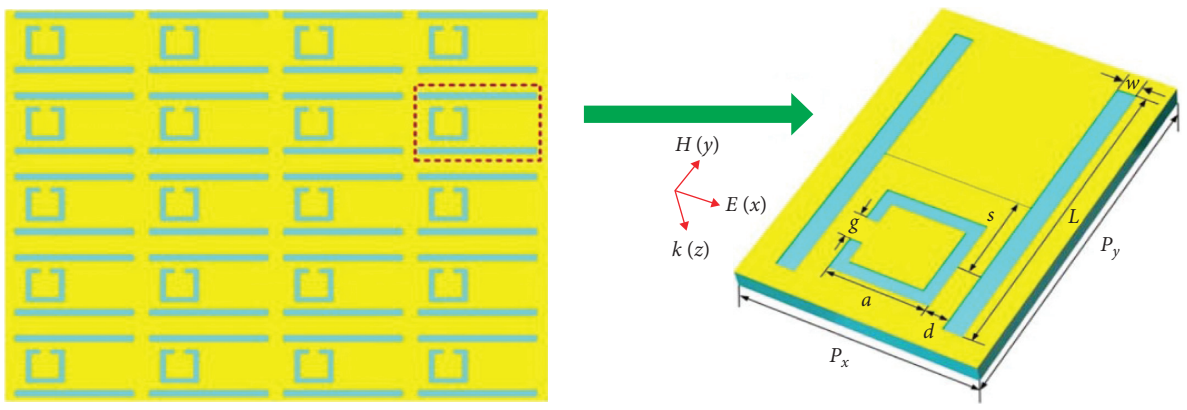

Figure 6: Continued.

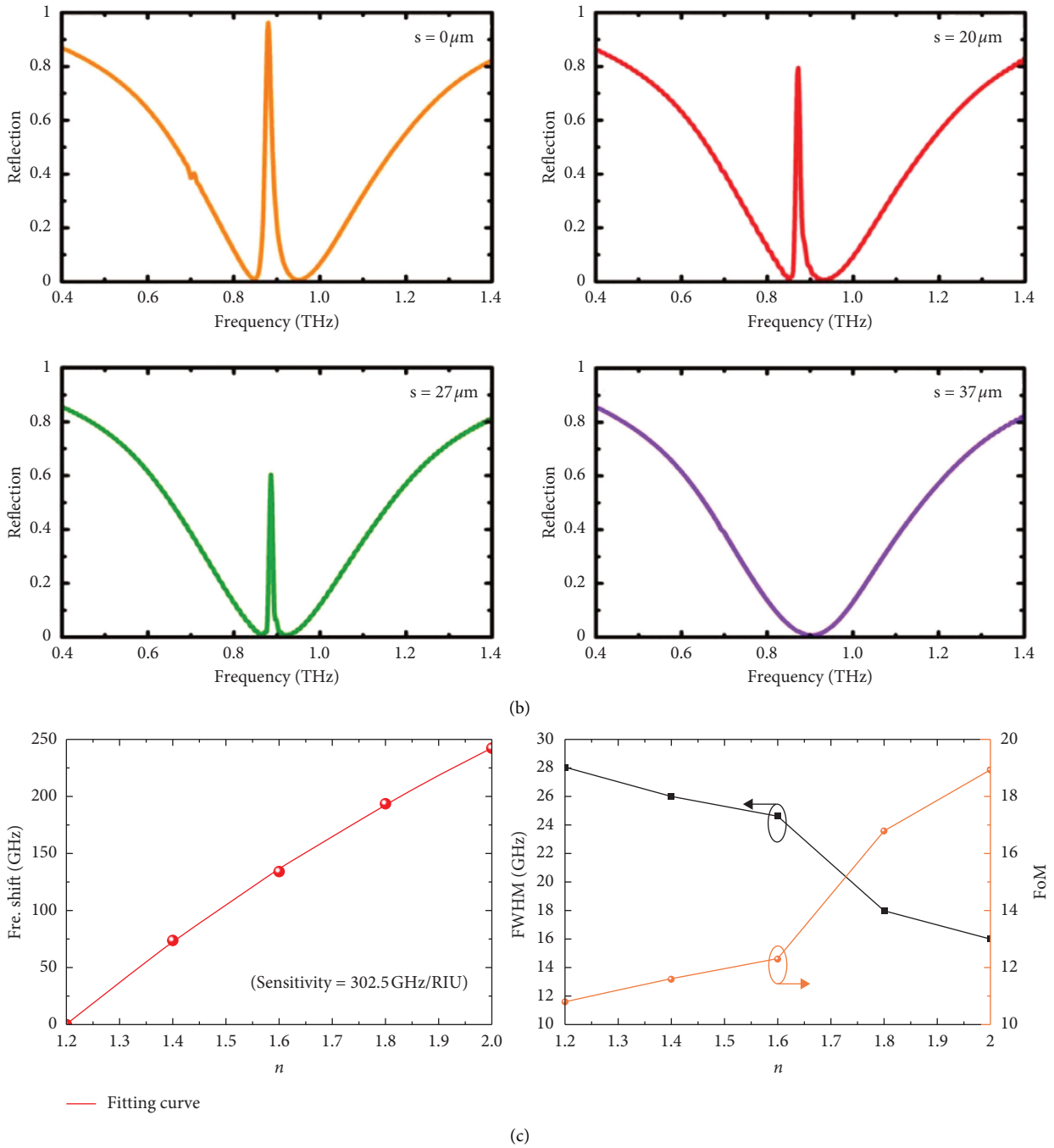

Figure 6: (a) Complementary bulk Dirac semimetal metamaterial structure. (b) Simulated reflection spectra under different lateral displacements ($E_f = 70$ meV). (c) Simulated frequency shift, FWHM, and FOM. (a, b) Reproduced with permission from reference [29] copyright 2014, IOP publishing.

transmission has promising applications in the design of slow-light devices and high sensitivity sensors.

Based on the planar SRRs structure, the resonant mode field is localized between the openings, and part of the mode field is inside the substrate, which limits the interaction between the electromagnetic field and the measured substance, so metamaterial sensors based on three-dimensional SRRs structure have been proposed. Compared with the planar SRRs structure, the electromagnetic field is extended to three-dimensional space, which can increase the mutual contact area with the substance to be measured, thereby improving the sensing sensitivity.

Bian et al. [39] proposed a metamaterial structure based on three-dimensional SRRs. The calculated surface current distribution is shown in Figure 7(a). It can be seen that the energy density is the largest at the opening, and the three-dimensional SRRs will make less energy dissipate on the substrate, which will greatly improve the interaction

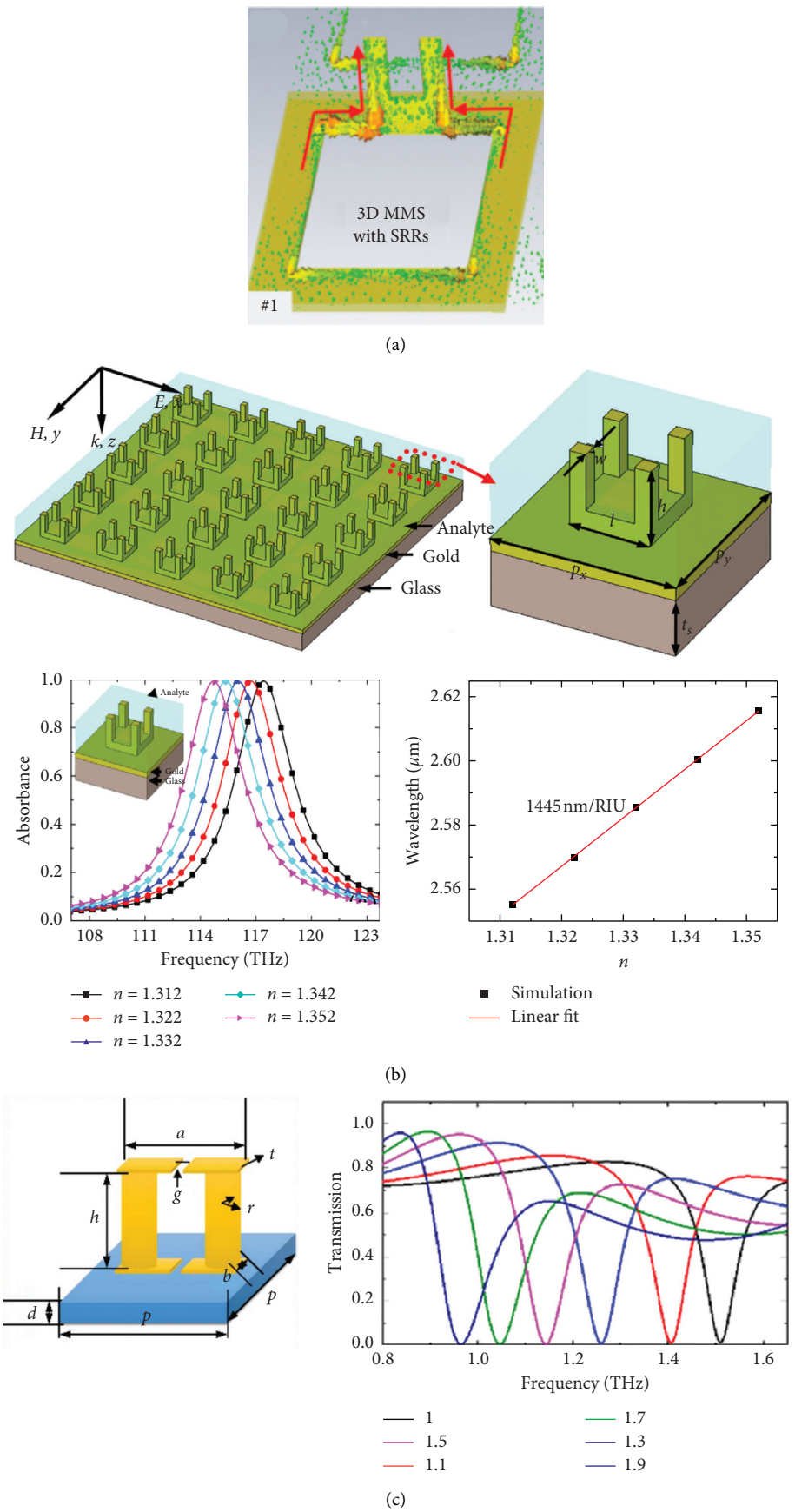

Figure 7: Continued.

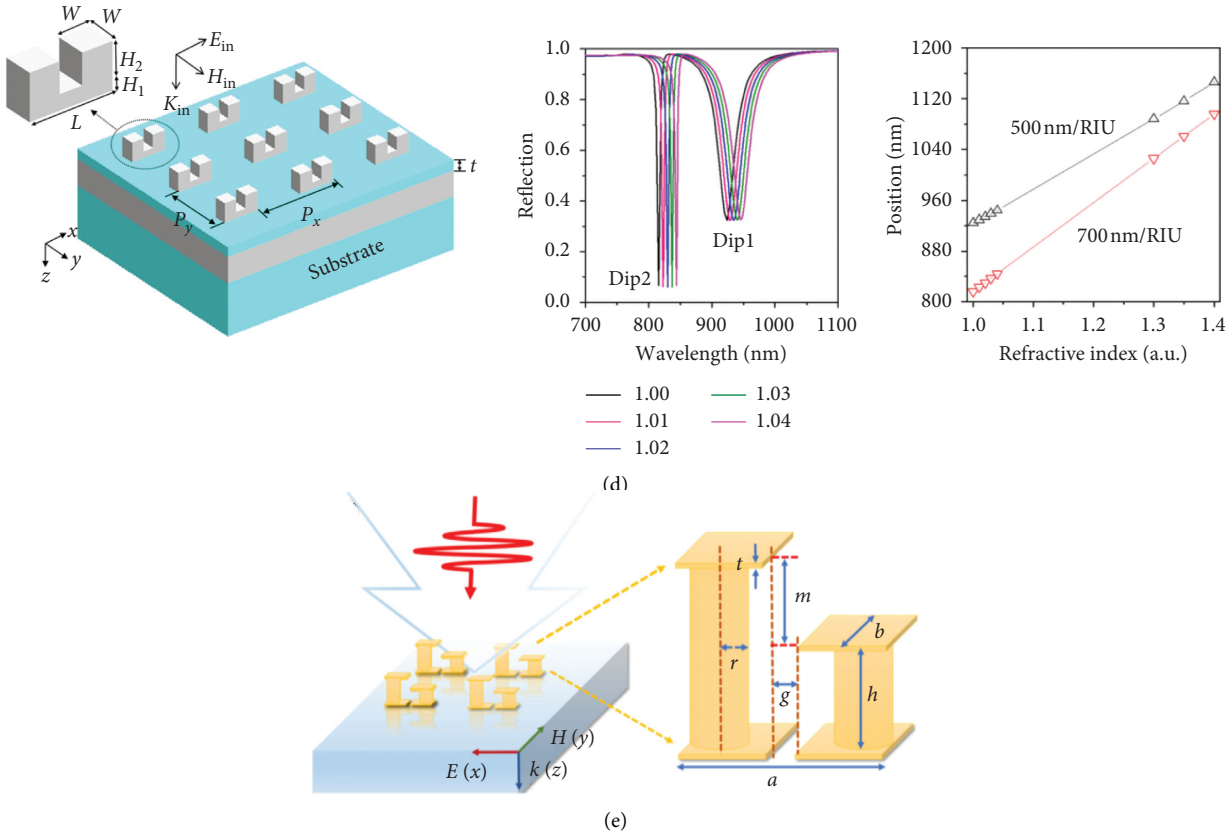

FIGURE 7: (a) Schematic diagrams of metamaterial sensors based on three-dimensional SRRs arrays. (b) Schematic diagrams, absorption spectra, and sensitivity of metamaterial sensors based on three-dimensional SRRs arrays, reproduced with permission from reference [40] copyright 2016, Elsevier B.V. (c) Schematic diagrams and transmission spectra of metamaterial sensors based on three-dimensional SRRs arrays, reproduced with permission from reference [41] copyright 2017, Optical Society of America. (d) Schematic diagrams, reflection, and sensitivity of metamaterial sensors based on three-dimensional SRRs arrays, reproduced with permission from reference [42] copyright 2018, IEEE. (e) Schematic diagrams of metamaterial sensors based on three-dimensional SRRs arrays, reproduced with permission from reference [43] copyright 2019, IEEE.

between the effective energy and the substance to be measured, and thus improve the sensing sensitivity. Cheng et al. [40] designed a metamaterial sensor composed of four U-shaped SRRs. Its structural schematic and transmission curve are shown in Figure 7(b). The calculated sensitivity reaches 1445 nm/RIU, the *Q*-factor reaches 41.2, and the FOM reaches 28.8. Wei et al. [41] designed a terahertz metamaterial sensor based on vertical split-ring with double splits. Its structural diagram and transmission curve are shown in Figure 7(c). The calculated sensitivity is 788 GHz/RIU, the *Q*-factor is about 20, and the FOM is about 10. In 2018, Jing et al. [42] reported an enhanced and modified 3D optical metamaterial with magnetic plasmon resonance, which consists of a periodic array of silver perpendicular SRR resonators, for an effective method of high sensitivity sensing. As shown in Figure 7(d), the sensitivity and FOM of the 3D metamaterials were as high as 700 nm/RIU and 170, respectively, indicating that the proposed 3D metamaterials have promising applications in label-free biomedical sensing. In 2019, Wang et al. [43] presented symmetry breaking introduced in vertical split-ring resonators metamaterials to excite narrow resonance, as shown in Figure 7(e). In contrast to previously reported planar asymmetric metamaterials, three-dimensional metamaterials are mainly excited by the combined magnetic and electrical components of terahertz illumination. In this case, ultranarrow linewidths (FWHM of 5.90 GHz) and sharp resonances with a high *Q*-factor of 327 at 1.93 THz emerge. The combination of high *Q*-factor resonance and high sensitivity of asymmetric vertical SRR metamaterials will lead to further inspiration for superior performance sensor design.

The metamaterial absorber is a typical structure of metamaterials. It is usually composed of a metal-dielectric-metal three-layer structure. At the resonant frequency, the upper and lower layers of metal usually form a reverse current, which in turn forms a vertical interface current loop, resulting in magnetic resonance. When the incident electromagnetic wave energy is transmitted vertically downwards and enters the dielectric layer through the top metal slit, it will form a lateral transmission. Therefore, by optimizing the structure of the metamaterial absorber and tuning the electric resonance and magnetic resonance, extremely strong electromagnetic field localization can be realized, thereby achieving zero reflection and zero

transmission of the incident electromagnetic wave at the resonant frequency, that is, complete absorption.

Metamaterial absorbers rely mainly on their strong resonance properties to gain significant advantages, as this type of sensor can produce a strong and measurable readout signal strong enough to accurately track the resonance absorption peak of a parameter shift in the reflection spectrum. The equivalent electromagnetic parameters of the metamaterial change with the substrate or geometry of the medium, resulting in a change in frequency. Metamaterial absorbers can be used to measure changes in the derived parameters.

Recently, there has been an increasing interest in metamaterial absorbers, providing an attractive platform for electromagnetic wave sensing applications [15, 16, 44–50]. Narrow-band or multiband metamaterial absorbers are critical in sensing and molecular detecting applications. In 2010, Na [44] first designed and implemented a metamaterial absorber working in the infrared band. The top layer of the metal structure is a periodic circular microdisk. The experiments measured the absorption spectra of air and water as the measured substance, as shown in Figure 8(a), the sensitivity reaches 400 nm/RIU and FOM reaches 87. Mirzaei et al. [48] modelled a metamaterial based label-free biosensor for DNA detection with a frequency shift of 3.6 GHz. As shown in Figure 8(b), a near-perfect metamaterial absorber for terahertz sensing applications has been proposed by Saadeldin et al. The structure has a near-perfect absorption of 99% at 2.249 THz and a narrow resonance peak with a Q-factor of 22.05. The structure has a sensitivity of 300 GHz/RIU, FOM of 2.94, and a refractive index range of 1.0 to 1.39 when applied as a sensor for sensing. In addition, the effect of the thickness of the analyte on the sensitivity was investigated over a range of 1.0 to 4.0 μm variations when the refractive index of the analyte $n = 1.35$, and the sensitivity $S = 23.7$ GHz/μm. Nanostructured plasma metamaterials are considered to be a good platform for narrow-band optical absorption and have a wide range of applications in sensing, filtering, modulation, and emission tailoring. However, achieving optical sensing and dynamic control of light in subnanometer absorption bandwidths remains a challenge. As shown in Figure 8(c), Feng et al. [49] demonstrated an asymmetric metal grating structure with perfect light absorption near 1.55 μm wavelength with a bandwidth of 0.28 nm using a propagating surface plasma mode with a low dissipation rate. By varying the structure parameters, the proposed structure provides a solution for chemical or biological sensing in the visible spectral range. The results show that the sensitivity and FOM of the sensor are 440 nm/RIU and 1333.33 RIU^{-1}, respectively.

3.2. Changing Substrate Properties. Recently, many research teams have attempted different approaches to achieve greater spectral modulation with the same medium variation, such as using low refractive index substrates, using ultrathin substrates, etching parts of high refractive index substrates, or integrating microfluidic channels or microcavities.

The dielectric layers of the metamaterial sensors mentioned previously are mostly made of GaAs and Si with high dielectric constants, which provide a large capacitance to the resonator and therefore reduce the capacitance variation caused by the target material. Recently, it has been found that the sensitivity can be significantly improved by using low refractive index materials instead of the commonly used high refractive index substrate materials and by using ultrathin substrates [51–54].

In 2010, Tao et al. [51] proposed a metamaterial biosensor based on SRRs structure and ultrathin silicon nitride (SiNx) substrate. In the experiment, 400 nm thick SiNx and 500 μm thick Si were selected as substrates, and silk fibro with different thicknesses was applied on the surface of the sensor element by spin coating. The measured transmission spectrum is shown in Figure 9(a). The test results show that when the thickness of the silk fibroin is 1500 nm, the resonance peak offset of the Si substrate sensor is 10 GHz, and the resonance peak offset of the SiNx substrate sensor is 116 GHz, indicating the sensor sensitivity of the SiNx substrate about 10 times that of Si substrate sensors. The main reason is that the permittivity of the SiNx substrate is about 7, the permittivity of the Si substrate is about 11, and the thickness of the Si substrate is much larger than the thickness of the SiNx substrate, resulting in the capacitance ratio of the Si substrate being much larger than of the SiNx substrate. Therefore, the sensitivity of the Si substrate sensor is smaller than that of the SiNx substrate sensor. Brian et al. [52] found that the refractive index sensitivity of nanopore arrays increases as the separation distance between the holes increases and redshifts the resonance. However, if a nanopore sensor is fabricated on a low refractive index substrate, additional sensitivity enhancement occurs, but the resonance is blue-shifted. They found that approximately 40% higher bulk refractive index sensitivity for a system of approximately 100 nm holes in 20 nm gold films fabricated on Teflon substrates ($n = 1.32$) compared to the case when conventional glass substrates ($n = 1.52$) were used. As shown in Figure 9(b), in order to get closer to practical applications, Hu et al. studied a paper-based terahertz metamaterial sensor [53], which can be used for quantitative analysis of different concentrations of glucose. In the experiment, 100 μL of glucose solution was deposited on the SRRs resonator, and as the glucose concentration increases, the offset of the resonant frequency increases, and the maximum offset can reach 300 GHz. For a glucose solution with a concentration of 7 $\text{mmol}\cdot\text{L}^{-1}$, the sensitivity is 14.3 $\text{GHz}\cdot(\text{mmol}\cdot\text{L}^{-1})^{-1}$, and for a glucose solution with a concentration of 30 $\text{mmol}\cdot\text{L}^{-1}$, the sensitivity is 10 $\text{GHz}\cdot(\text{mmol}\cdot\text{L}^{-1})^{-1}$. The flexible metamaterial based on the paper substrate has the characteristics of high sensitivity, transparency, portability, etc. and has more practical application value. In 2017, Srivastava et al. [54] experimentally demonstrated a dual-surface terahertz metamaterial sensor based on asymmetric SRRs with double splits on an ultrathin flexible polyimide substrate with a low refractive index, as shown in Figure 9(c), which can realize sensing on both sides of the structure and reveals a highly enhanced sensitivity. It has promising applications in industrial sensing systems and

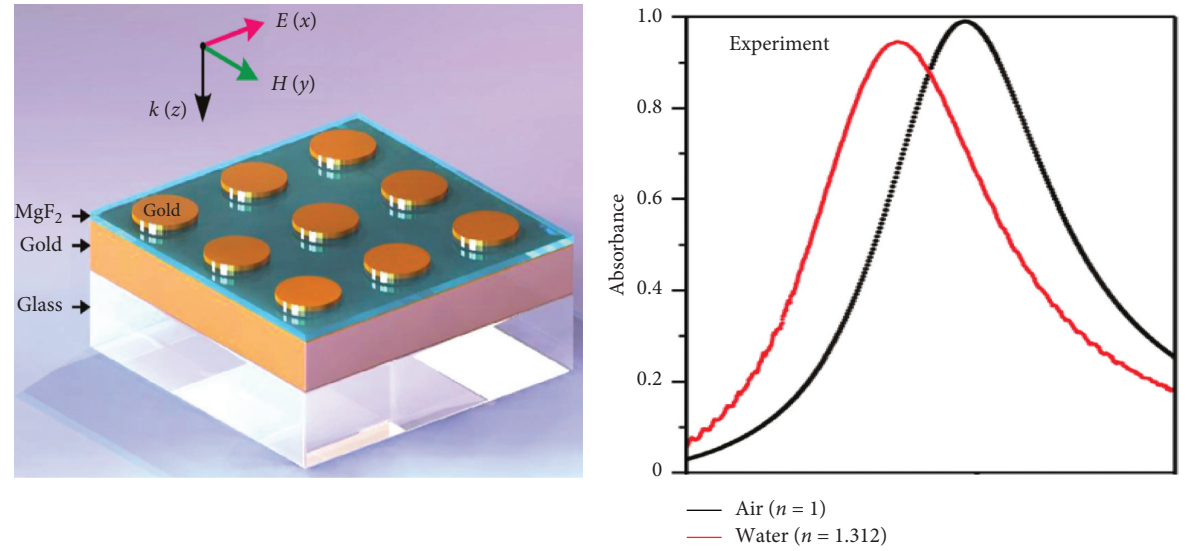

(a)

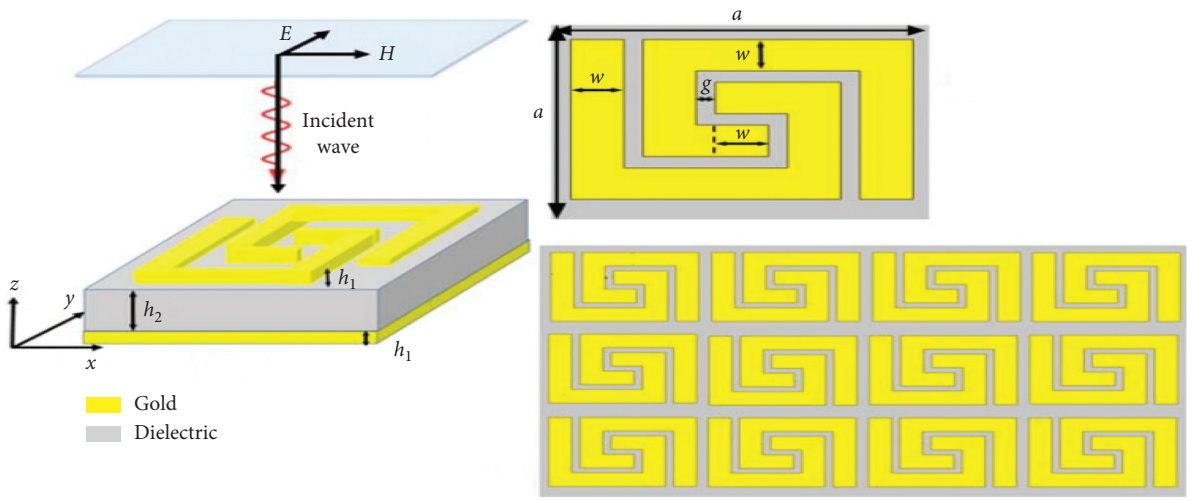

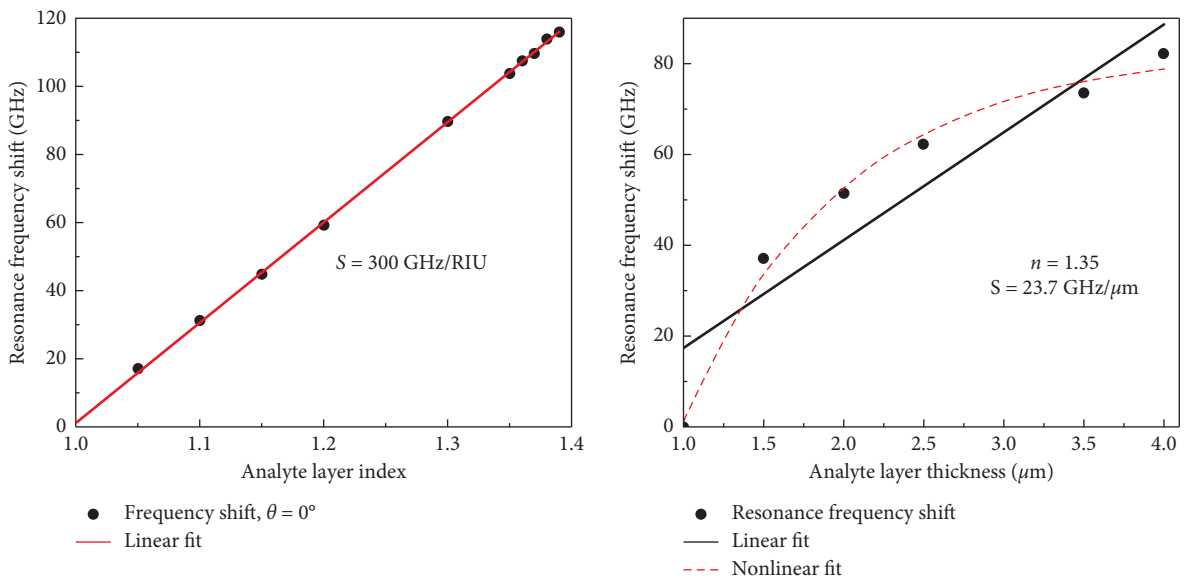

(b)

Figure 8: Continued.

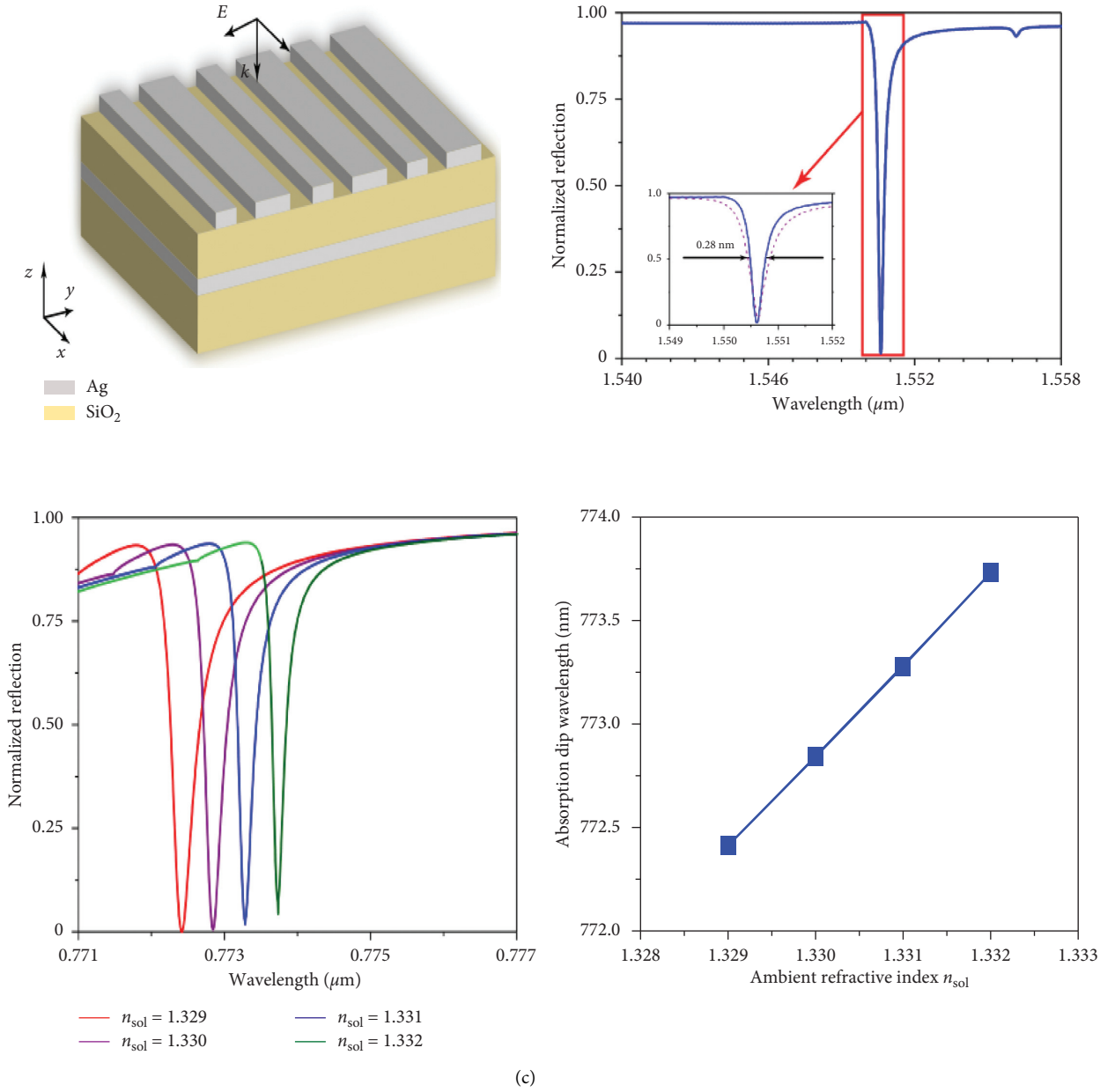

Figure 8: Schematic diagrams, reflection/absorption spectra, and sensitivity of metamaterial absorber sensors. (a) Reproduced with permission from reference [44] copyright 2010, American Chemical Society. (b) Reproduced with permission from reference [16] copyright 2019, IEEE. (c) Reproduced with permission from reference [49] copyright 2018, Optical Society of America.

improves biosensing performance at lower molecular concentrations.

However, high index semiconductor substrates are typically required to actively control the metamaterial response of the gated structure, and this is problematic with ultrathin substrates because of the integration required for the integrated fluidic channels, resulting in poor durability. In order to achieve greater spectral modulation for the same medium variation and to increase the sensing sensitivity of metamaterial sensors, the substrate effect is reduced by etching parts of the high refractive index substrate to highlight the effect of the surrounding medium variation [55–58].

In 2018, Moritake and Tanaka [57] proposed and demonstrated the use of selective and isotropic etching of substrates to eliminate the effect of substrate on plasma resonance. The concept of substrate etching is shown in Figure 10(a). After the formation of metal nanostructures on the substrate, only the substrate is selectively etched. This is shown in Figure 10(a). It is demonstrated that the use of substrate etching reduces the effective refractive index around the metal nanostructure, thereby eliminating the substrate-induced resonant red-shift and improving the refractive index sensitivity. In addition, the change in the resonance quality factor Q of the substrate etching method was investigated in detail. As shown in Figure 10(b), the

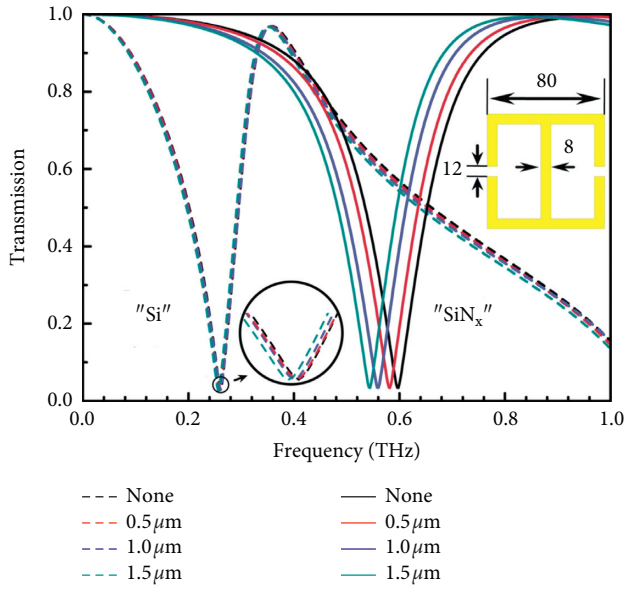

(a)

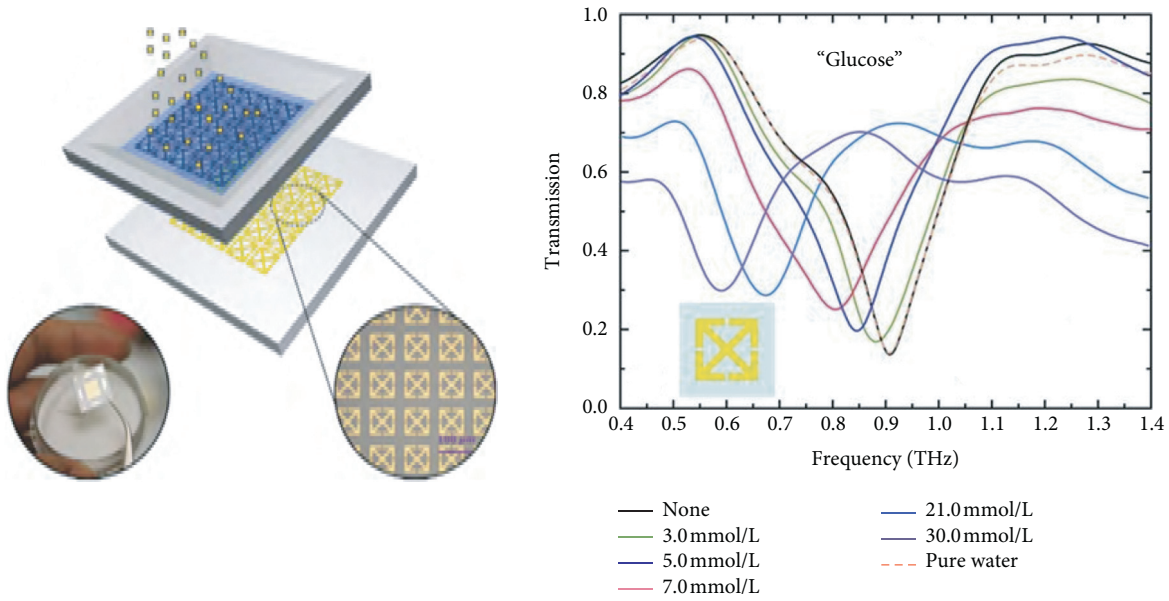

(b)

Figure 9: Continued.

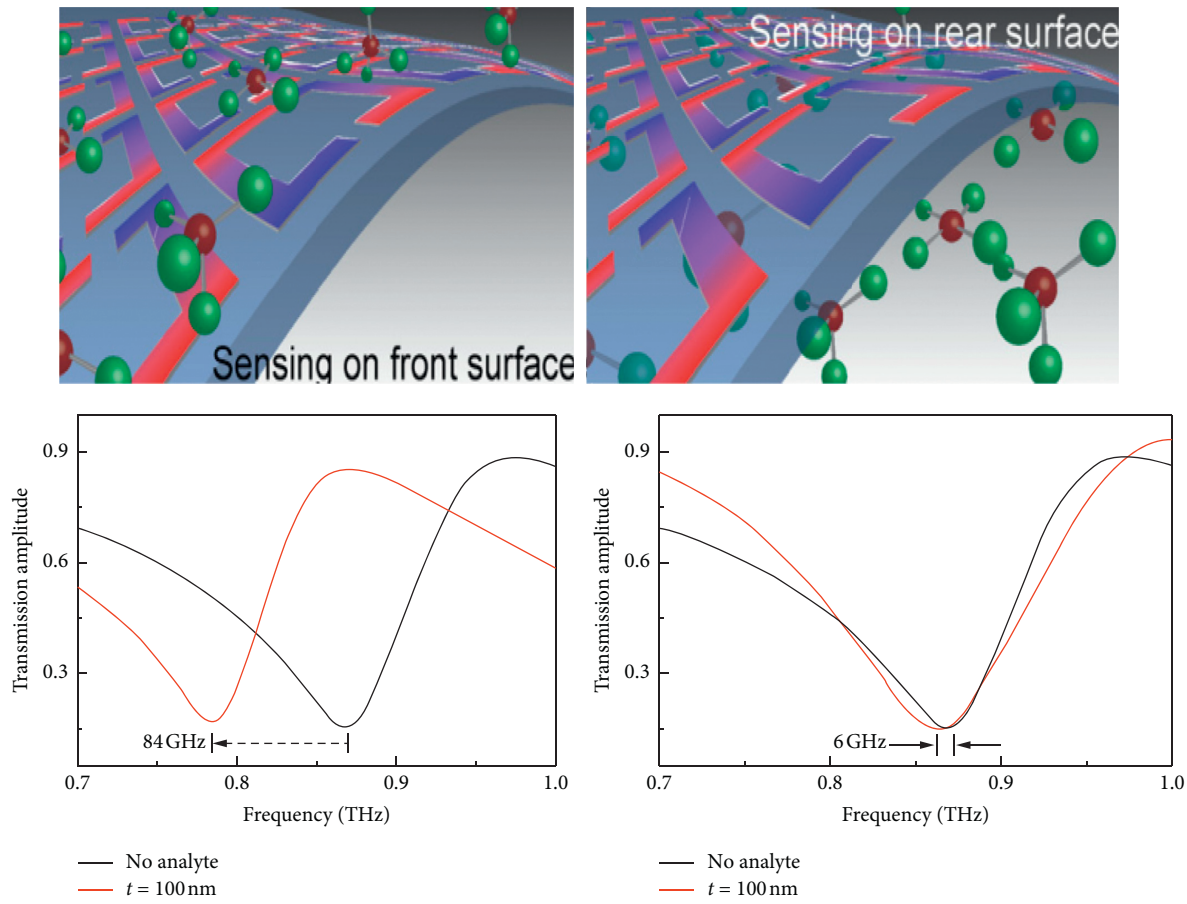

(c)

Figure 9: (a) Transmission spectra of metamaterial sensors based on ultrathin substrates, reproduced with permission from reference [51] copyright 2010, AIP publishing. (b) Schematic diagrams and transmission spectra of metamaterial sensors based on lower-index substrates, reproduced with permission from reference [53] copyright 2011, John Wiley and Sons. (c) Schematic diagrams and transmission spectra of metamaterial sensors based on an ultrathin flexible polyimide substrate, reproduced with permission from reference [54] copyright 2017, AIP publishing.

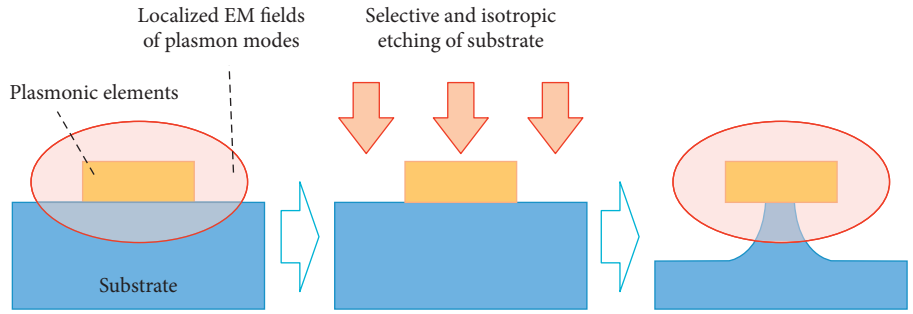

(a)

Figure 10: Continued.

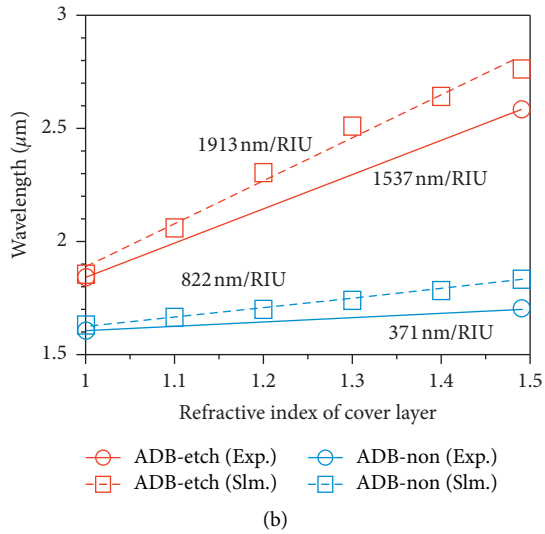

(b)

Figure 10: (a) Schematic of substrate etching for plasmonic elements formed on a substrate. (b) The wavelength shift as a function of the refractive index of the coating layer for the asymmetric double bar (ADB)-etch and ADB-non. (a, b) Reproduced with permission from reference [57] copyright 2018, Optical Society of America.

refractive index sensitivity is significantly improved to 1537 nm/RIU due to the substrate etching making the electric field accessible under the nanostructure. The refractive index sensitivity is substantially improved compared to the case without substrate etching. The method proposed in this paper is applicable to a variety of plasmonic structures to eliminate the influence of substrates on the realization of high-performance plasmonic devices.

In 2019, Meng et al. [58] proposed a metamaterial sensor with an etched trench introduced in the inductance-capacitance gap region of a split-ring resonator, and the results showed an increase in frequency shift and sensitivity when a dielectric material of up to 18 μm thickness was deposited on the sensor surface. As shown in Figure 11, Wang et al. [59] theoretically optimized the conventional fabrication process for realizing terahertz metamaterial absorbers and analyzed the feasibility of matching the existing surface micromachining process. The results showed that the sensing performance of the new metamaterial sensor was significantly enhanced due to the surface-relief design compared to the conventional metamaterial sensor. The proposed method for the design of terahertz metamaterial absorbers can be used to implement ultrasensitive metamaterial sensors.

To design a highly sensitive refractive index sensor, the degree of overlap between the electromagnetic field and the substance needs to be enhanced. Related studies have shown that when molecules are not attached to the sensor surface, the electric field strength decreases as the distance between the substance and the surface increases, which results in a weakening of sensitivity. The research team, therefore, began to investigate how to design geometrical structures to enhance the overlap between the substance and the electromagnetic field.

The emergence of microfluidics, which has received widespread attention from research teams, allows the manipulation of very small amounts of fluid (10^{-9} to 10^{-18} L) using microchannels (approximately 10–100 μm in size) [60]. It is potentially valuable in the field of biological and chemical detection because of its high sensitivity, low cost, and fast measurement. By designing different forms of microfluidic channels, the refractive index sensitivity of the sensors has been greatly enhanced [61–64].

Zhou et al. [63] demonstrated a metamaterial integrated microfluidic sensor with the capability of multiband sensing for the dielectric property of various chemicals. As shown in Figure 12(a), the sensor is composed of a symmetrical double SRRs structure, which enhances the resonant strength and sensing capability of the resonant cavity compared to a single SRRs. As shown in Figure 12(b), a dielectric model is developed by fitting a nonlinear curve to the resonance and theoretical derivation and experimentally validated to obtain a complex dielectric constant from the measured "butterfly-like" result curve, which can be used as a diagnostic indicator to identify chemicals. In addition, the sensor has been extended to integrate multiple resonators to obtain the dielectric spectrum of ethanol, enhancing its potential for chemical analysis and practical applications.

Withayachumnankul et al. [62] implemented a metamaterials microfluidic sensor based on a single SRR resonator, as shown in Figure 13. At resonance, an SRR creates a strong electric field in the deep subwavelength region. The flow of the liquid over this region can alter the local field distribution and thus affect the SRR resonance behavior. Specifically, the resonant frequency and bandwidth are influenced by the complex dielectric constant of the liquid sample. By establishing an empirical relationship between the sensor resonance and the sample dielectric constant, the complex dielectric constant of the liquid sample can be estimated. This work advances the use of SRR-based microfluidic sensors for the identification, classification and characterisation of chemical and biochemical analytes.

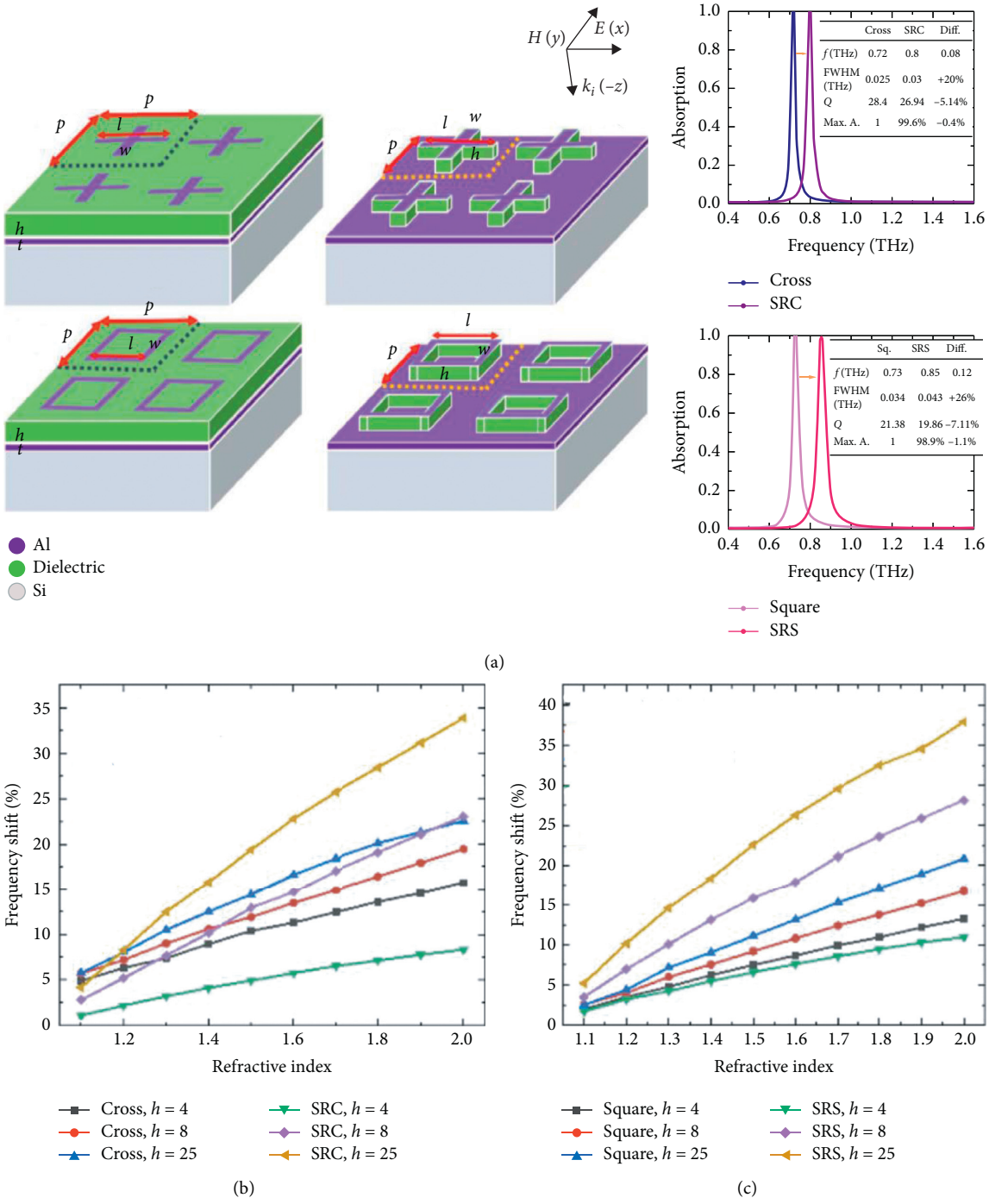

FIGURE 11: Comparison of the two most common terahertz metamaterial absorbers and numerical simulations in terms of absorption and sensing capabilities, reproduced with permission from reference [59] copyright 2020, Optical Society of America.

Hu et al. [64] proposed and experimentally demonstrated a novel metamaterial absorber integrated terahertz microfluidic sensor. As shown in Figure 14(a), by introducing matter into two parallel metallic structures, a transverse cavity resonance occurs inside the absorber, resulting in a significant increase in sensitivity. Furthermore, the emergence of this highly sensitive sensor provides an interesting approach to the design of subsequent highly sensitive chemical and biological sensors.

3.3. Other Ways. Furthermore, to achieve very strong magnetic resonance in metamaterials for high-performance sensing, Chen et al. [65] studied numerically photonic microcavity-enhanced magnetic plasmon resonance in metamaterials for high quality refractive index sensing, as shown in Figure 15(a). The radiation damping of the magnetic plasmon resonance is greatly reduced and the linewidth is greatly reduced due to the coupling of the magnetic plasmon resonance excited in the metallic SRRs to

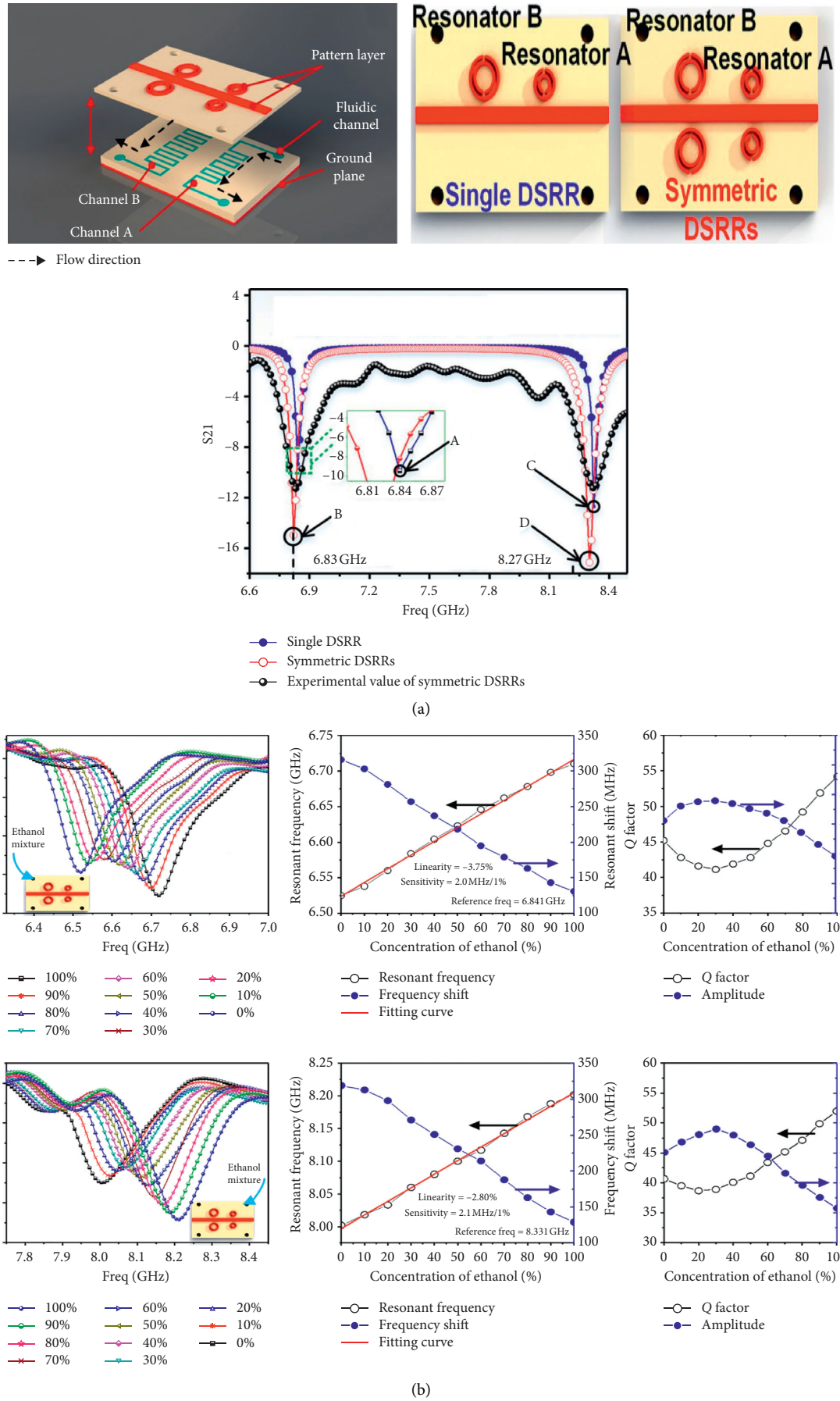

FIGURE 12: (a) Schematic diagrams and simulated transmission spectra of integrated microfluidic metamaterial sensors. (b) Measured results from the metamaterial sensor for ethanol with different concentrations in channels A and B. (a, b) Adapted with permission from reference [63] copyright 2018, Springer Nature.

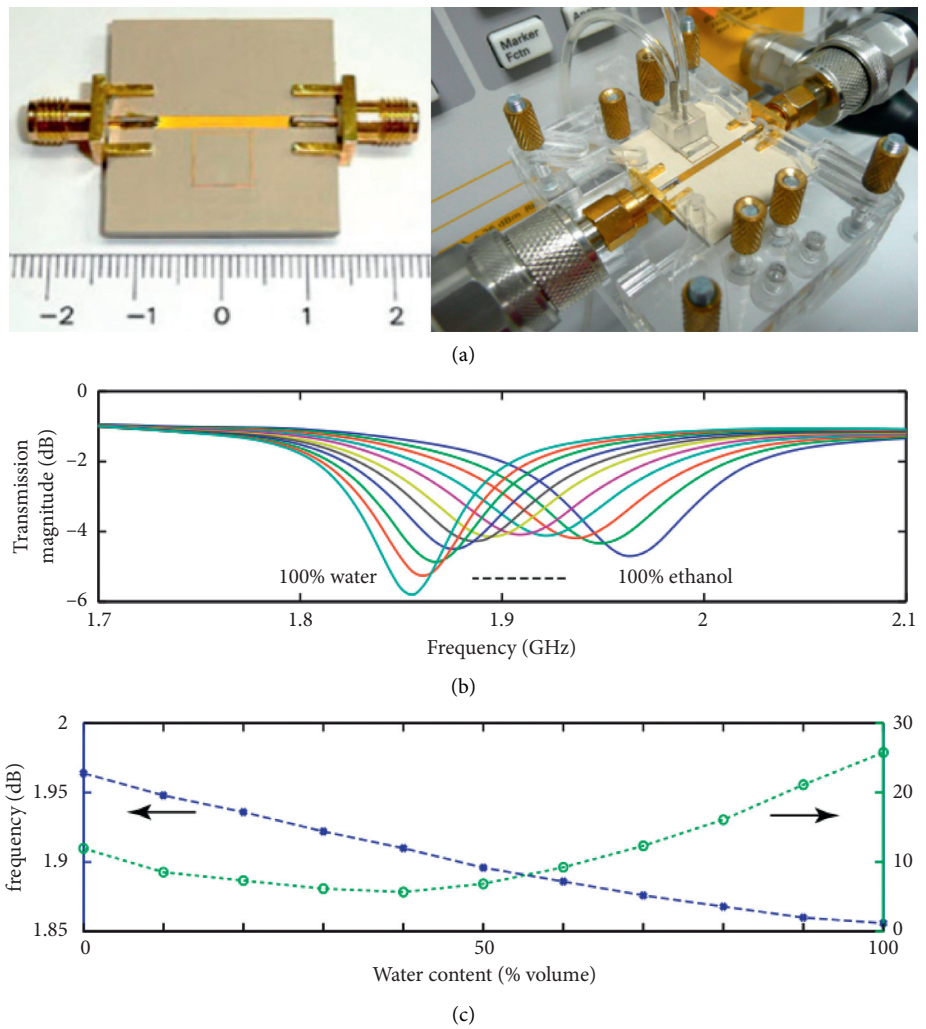

FIGURE 13: Assembly of microfluidic sensor modules based on microstrip-coupled SRR metamaterials and measured transmission response of water-ethanol mixtures at different volume fractions, adapted with permission from reference [62] copyright 2013, Elsevier B.V.

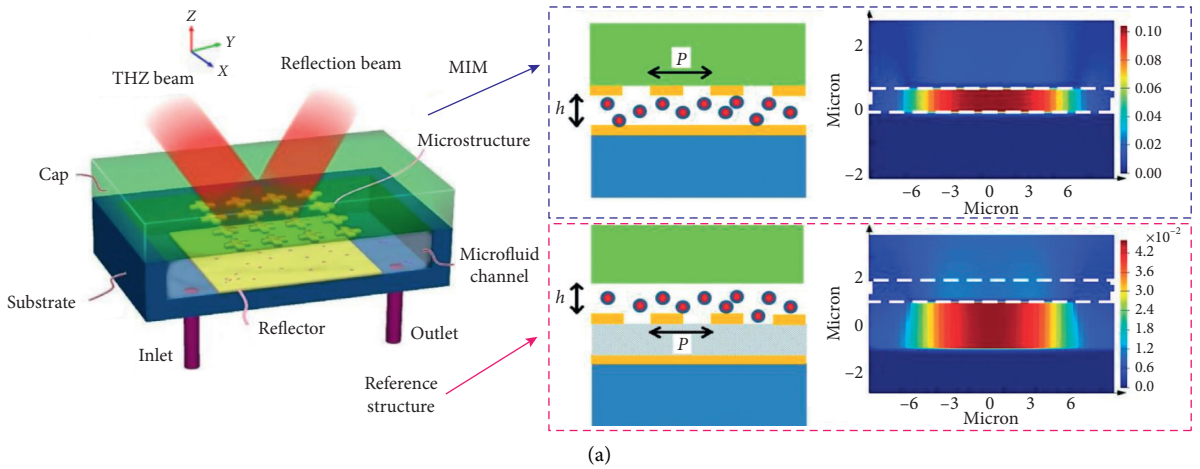

FIGURE 14: Continued.

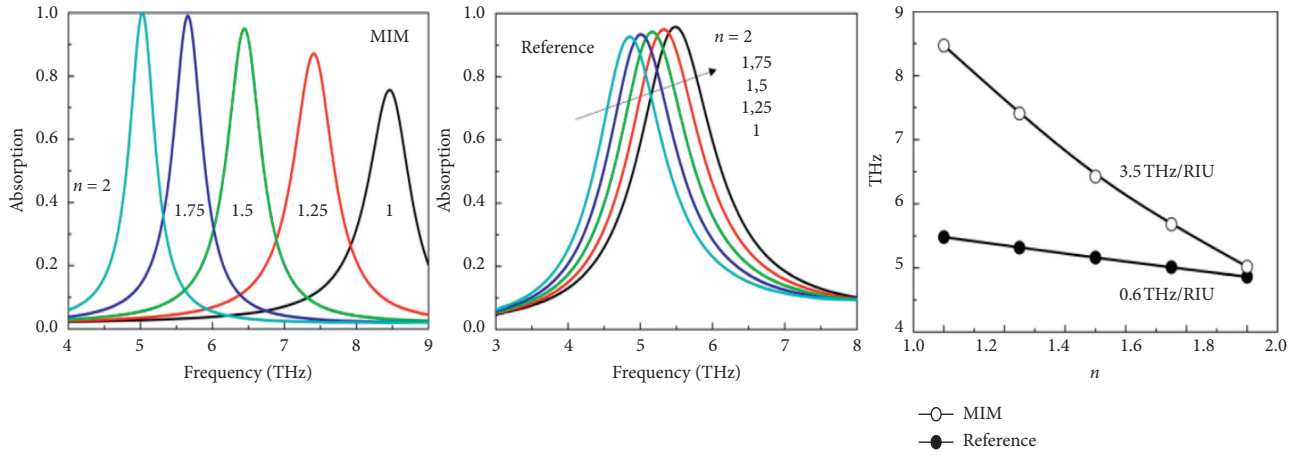

(b)

Figure 14: (a) Schematic diagram of the metamaterial absorber sensors with microfluidic channel located inside and on top of the metamaterial absorber. (b) Absorption spectra and resonance peak corresponding to different channel refractive index for MIM and reference. (a, b) Reproduced with permission from reference [64] copyright 2016, John Wiley and Sons.

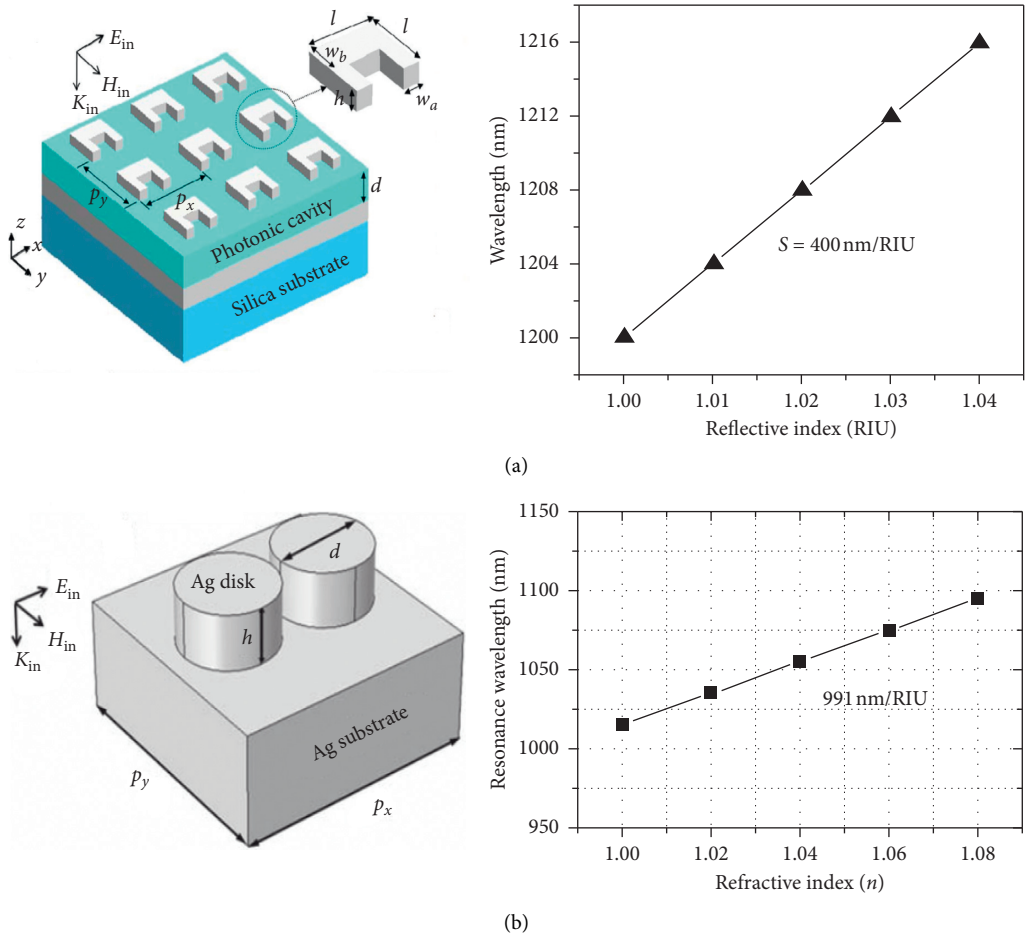

Figure 15: Schematic diagrams and refractive index wavelength sensitivity of metamaterial sensors based on strong magnetic resonance. (a) Reproduced with permission from reference [65] copyright 2019, IEEE. (b) Reproduced with permission from reference [14] copyright 2019, IOP publishing.

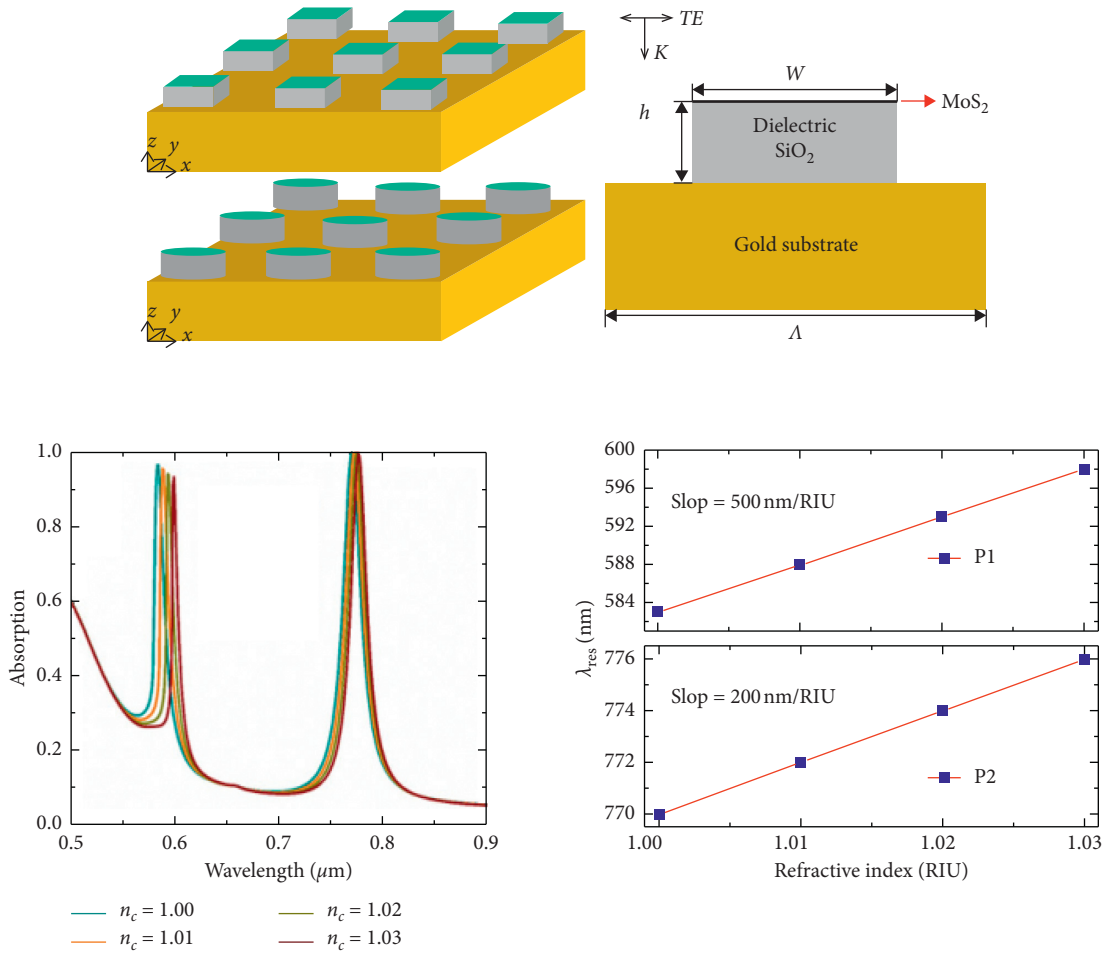

FIGURE 16: Schematic diagrams and refractive index wavelength sensitivity of metamaterial sensor based on cylinder MoS_2, reproduced with permission from reference [66] copyright 2019, Elsevier B.V.

the photonic microcavity mode supported by the photonic microcavity. The cavity-coupled metamaterial sensor has the advantages of narrow bandwidth, wide modulation range and large magnetic field enhancement at magnetic plasma resonance with high sensitivity ($S = 400$ nm/RIU and $S^* = 26$ RIU) and figure of merit (FOM = 33 and FOM* = 4215). It is shown that the proposed metamaterials have potential applications in plasma biosensors. In 2019, a metamaterial structure consisting of a pair of closely spaced metallic nanodiscs arranged on a metallic substrate was proposed by Chen et al. [14]. A very strong magnetic resonance exists in this structure, and theoretical analysis suggests that the magnetic resonance is caused by incoming plasma hybridisation within the pair of metallic nanodiscs. Under strong magnetic resonance, the electric field tends to increase, and ultranarrow bandwidths and near-perfect absorption can be achieved. It is shown that the designed sensor has a high sensitivity ($S = 991$ nm/RIU, $S^* = 47$ RIU) and FOM (FOM = 124, FOM* = 17702).

Qiu et al. [66] proposed and investigated a dual-frequency perfect metamaterial absorber consisting of a simple periodic patterned cylindrical/square MoS_2-dielectric silica arrays supported by a metal ground plane, as shown in Figure 16. The application of this metamaterial absorber in refractive index sensors is also presented in the paper. Compared to previous dual-band metamaterial absorbers, the cylinder MoS_2-based absorber is simple in shape, greatly simplifies the fabrication process and is polarization insensitive. It has great potential in the visible and near-infrared spectral range, for instance, as a plasma sensor.

As shown in Figure 17, Chen and Fan [67] demonstrated a novel terahertz metamaterial sensor with integrated microfluidic channels, where two pairs of high refractive index dielectric disks were arranged into the unit cell. The ultrahigh-strong toroidal dipole response associated with the presence of trapped modes was excited and studied by introducing a new symmetry-breaking method into the cell structure. Simulation results show that the sensor has a high Q-factor and FOM of 3189 and 515, respectively, and thus with this advantage, it will be used in a wide range of applications in liquid and gas sensing.

He et al. [68] proposed an ultrasensitive terahertz sensor based on a graphene metamaterial with a complementary structure of wire slot and split-ring resonator slot arrays, as shown in Figure 18. The sensitivity of the sensor reached 177.7 GHz/RIU with FOM of 59.3. In addition, this structure

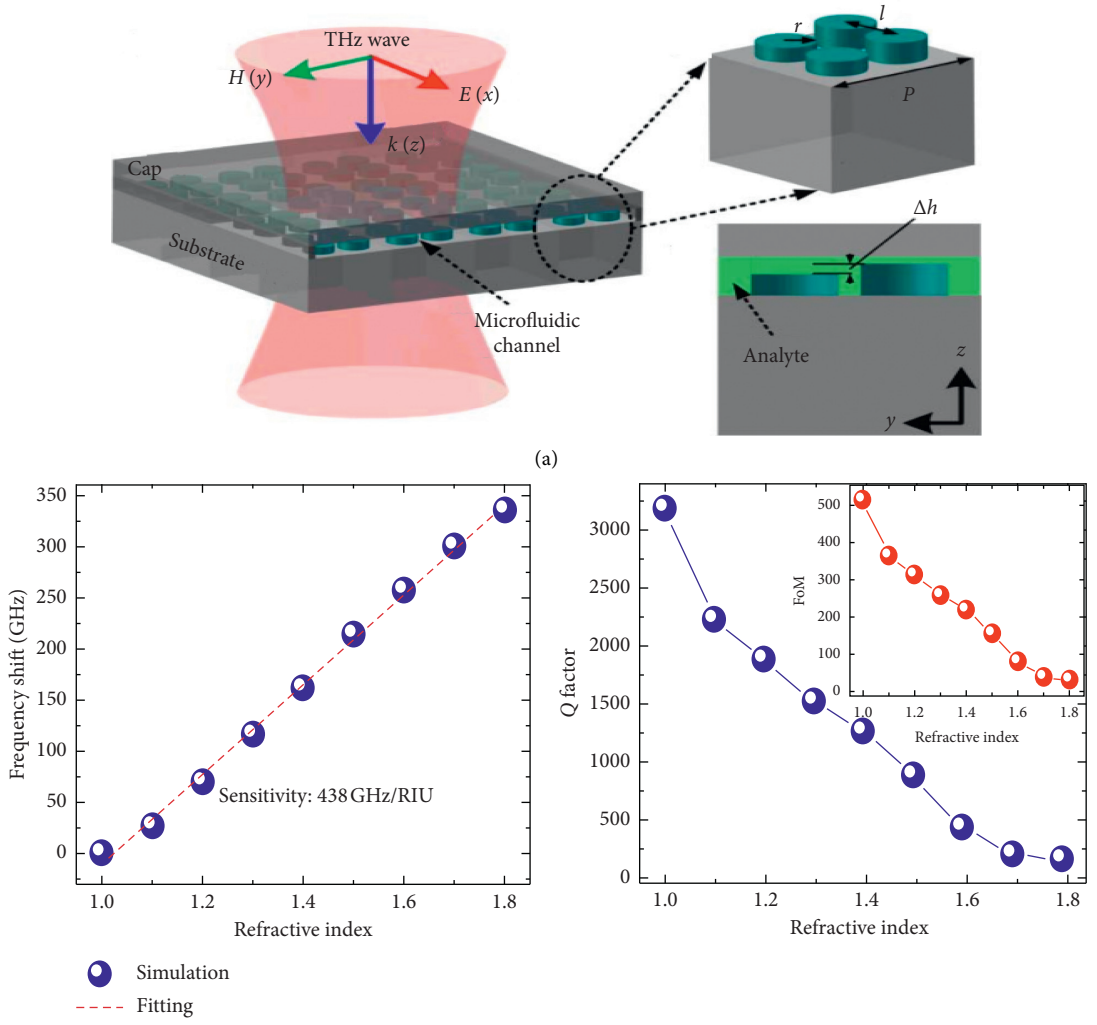

FIGURE 17: Schematic diagrams, refractive index frequency sensitivity, and Q-factor of all-dielectric metamaterial sensor, reproduced with permission from reference [67] copyright 2019, Optical Society of America.

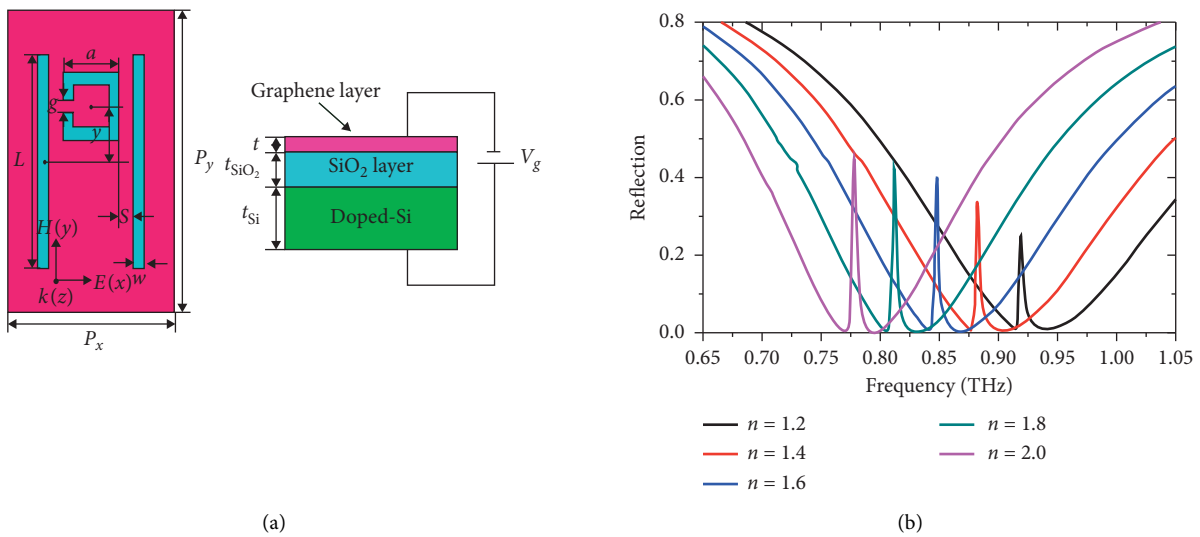

FIGURE 18: Continued.

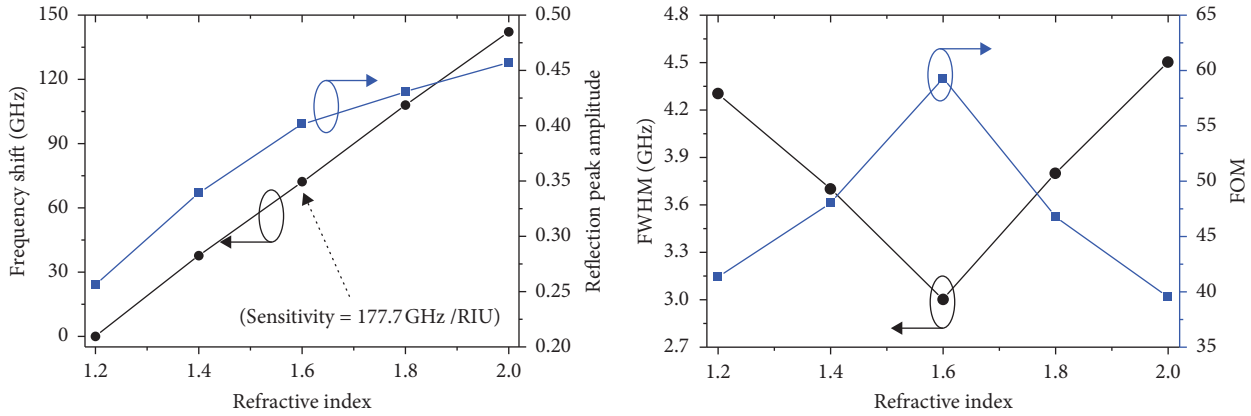

Figure 18: Schematic diagram, reflection spectra, refractive index frequency sensitivity, and FOM of sensor based on complementary graphene metamaterials, reproduced with permission from reference [68] copyright 2016, the Royal Society of Chemistry (RSC).

has the advantage of enhancing the absorption and sensing performance of biomolecules, as well as dynamically adjusting the sensing range by adjusting the Fermi energy of the graphene.

4. Challenges and Prospects

Metamaterials can manipulate electromagnetic waves in specific ways and exhibit supernormal electromagnetic properties that natural materials do not possess. In addition, metamaterials can realize strong localization and enhancement of electromagnetic field, thereby providing a novel sensing platform with the advantages of high sensitivity, high resolution, fast response, and simple measurement.

Metamaterial sensors can break through the resolution limit of traditional sensors for a small amount of substance and have higher sensing sensitivity and resolution than traditional sensors. During the past decade, researchers have been focusing on further improving the sensing characteristics of metamaterial sensors and promoting their development. Currently, metamaterial sensing technology is relatively mature. However, in order to truly move towards practical applications and explore the broad application prospects of metamaterial sensors in the fields of substance detection, environment sensing, biosensing, food safety control, and homeland security, like any emerging field, metamaterial sensing also faces many challenges:

(1) Metamaterial sensors still need improvements in sensitivity and resolution by designing special metamaterial structures or using specific dielectric materials.

(2) With the advancement of microfabrication and nanofabrication technology, the precise preparation of different metamaterial sensors is realized, creating new possibilities for its practical application.

(3) In addition to the realization of metamaterial sensors based on resonant frequency shift, the combination of the amplitude and phase changes of electromagnetic waves with the characteristics of metamaterials can expand the types of metamaterial sensors.

(4) Continue to develop the fields of metamaterial sensing, such as pressure, temperature, density, thickness, strain, and position.

(5) To address the detection limitation of only one substance at a time, multichannel metamaterial sensors should be developed.

5. Conclusion

In this review paper, we introduced metamaterial sensors from several aspects such as sensing mechanism, main characteristic parameters, and sensing characteristics improvement. It focuses on the development overview of improving the sensing sensitivity of the metamaterial sensors by optimizing the structure and changing substrate properties.

The superiority and versatility of metamaterial sensors are obvious. They usually exhibit enhanced characteristics and capabilities potential to overcome many of the limitations of conventional sensing devices. However, based on actual needs, the sensitivity, accuracy, and detection limit of metamaterial sensors need to be further improved. With the progress of microstructure processing technology and the emergence of new materials, it is believed that more and more high-performance metamaterial sensors will appear and have broader application prospects in the future.

Conflicts of Interest

The authors declare that they have no conflicts of interest.

Acknowledgments

This work was supported and funded by the National Natural Science Foundation of China (51965047), Natural Science Foundation of Inner Mongolia (2018MS06007), and

Research Startup Fund of High-Level Talents Introduction in 2018 (21700-5185131 and 21700-5185128).

References

[1] J. J. Wang, L. Chen, S. Kwan, F. Liu, and X. Deng, "Resonant grating filters as refractive index sensors for chemical and biological detections," *Journal of Vacuum Science & Technology B: Microelectronics and Nanometer Structures*, vol. 23, no. 6, Article ID 3006, 2005.

[2] Y. Cheng, H. Luo, F. Chen, and R. Gong, "Triple narrow-band plasmonic perfect absorber for refractive index sensing applications of optical frequency," *OSA Continuum*, vol. 2, no. 7, Article ID 2113, 2019.

[3] T. Wu, Y. Liu, Z. Yu, Y. Peng, C. Shu, and H. Ye, "The sensing characteristics of plasmonic waveguide with a ring resonator," *Optics Express*, vol. 22, no. 7, Article ID 7669, 2014.

[4] T.-Y. Chen, P. T. K. Loan, C.-L. Hsu et al., "Label-free detection of DNA hybridization using transistors based on CVD grown graphene," *Biosensors and Bioelectronics*, vol. 41, pp. 103–109, 2013.

[5] F. Chen, Y. Cheng, and H. Luo, "Temperature tunable narrow-band terahertz metasurface absorber based on InSb micro-cylinder arrays for enhanced sensing application," *IEEE Access*, vol. 8, pp. 82981–82988, 2020.

[6] C.-S. Chu, K.-Z. Lin, and Y.-H. Tang, "A new optical sensor for sensing oxygen based on phase shift detection," *Sensors and Actuators B: Chemical*, vol. 223, pp. 606–612, 2016.

[7] T. York, S. Achilefu, S. P. Lake et al., "Bioinspired polarization imaging sensors: from circuits and optics to signal processing algorithms and biomedical applications," *Proceedings of the IEEE*, vol. 102, no. 10, pp. 1450–1469, 2014.

[8] L. Li, W. Long, C. Jiang, and Q. Chen, "Research progress of terahertz sensor based on artificial microstructure," *Infrared and Laser Engineering*, vol. 48, no. 2, Article ID 203001, 2019.

[9] G. V. Eleftheriades and N. Engheta, "Metamaterials: fundamentals and applications in the microwave and optical regimes [scanning the issue]," *Proceedings of the IEEE*, vol. 99, no. 10, pp. 1618–1621, 2011.

[10] D. R. Smith, J. B. Pendry, and M. C. K. Wiltshire, "Metamaterials and negative refractive index," *Science*, vol. 305, no. 5685, pp. 788–792, 2004.

[11] J. Valentine, S. Zhang, T. Zentgraf et al., "Three-dimensional optical metamaterial with a negative refractive index," *Nature*, vol. 455, no. 7211, pp. 376–379, 2008.

[12] J. Li, C. M. Shah, W. Withayachumnankul et al., "Mechanically tunable terahertz metamaterials," *Applied Physics Letters*, vol. 102, no. 12, pp. 2742–2765, 2013.

[13] T. Chen, S. Li, and H. Sun, "Metamaterials application in sensing," *Sensors*, vol. 12, no. 3, pp. 2742–2765, 2012.

[14] J. Chen, H. Nie, C. Tang et al., "Highly sensitive refractive-index sensor based on strong magnetic resonance in metamaterials," *Applied Physics Express*, vol. 12, no. 5, Article ID 052015, 2019.

[15] L. Shengyong, A. Xiaochuan, W. Ronghua, and C. Jiajun, "Design and simulation verification an environmental change metamaterial sensor," *Optics Communications*, vol. 428, pp. 251–257, 2018.

[16] A. S. Saadeldin, M. F. O. Hameed, E. M. A. Elkaramany, and S. S. A. Obayya, "Highly sensitive terahertz metamaterial sensor," *IEEE Sensors Journal*, vol. 19, no. 18, pp. 7993–7999, 2019.

[17] J. Liu, L. Fan, J. Ku, and L. Mao, "Absorber: a novel terahertz sensor in the application of substance identification," *Optical and Quantum Electronics*, vol. 48, p. 80, 2016.

[18] T. Driscoll, G. O. Andreev, and D. N. Basov, "Tuned permeability in terahertz split-ring resonators for devices and sensors," *Applied Physics Letters*, vol. 91, no. 6, Article ID 62511, 2007.

[19] X. Yan, X. F. Zhang, L. J. Liang, and J. Q. Yao, "Research progress in the application of biosensors by using metamaterial in terahertz wave," *Guang Pu Xue Yu Guang Pu Fen Xi/Spectroscopy and Spectral Analysis*, vol. 34, no. 9, pp. 2365–2371, 2014.

[20] H.-J. Lee and J.-G. Yook, "Biosensing using split-ring resonators at microwave regime," *Applied Physics Letters*, vol. 92, no. 25, Article ID 254103, 2008.

[21] X. Wu, B. Quan, X. Pan et al., "Alkanethiol-functionalized terahertz metamaterial as label-free, highly-sensitive and specific biosensor," *Biosensors and Bioelectronics*, vol. 42, pp. 626–631, 2012.

[22] B. Han, Z. Han, J. Qin, Y. Wang, and Z. Zhao, "A sensitive and selective terahertz sensor for the fingerprint detection of lactose," *Talanta*, vol. 192, pp. 1–5, 2019.

[23] R. Singh, I. A. I. Al-Naib, M. Koch, and W. Zhang, "Asymmetric planar terahertz metamaterials," *Optics Express*, vol. 18, no. 12, pp. 13044–13050, 2010.

[24] C. Debus and P. H. Bolivar, "Frequency selective surfaces for high sensitivity terahertz sensing," *Applied Physics Letters*, vol. 91, no. 18, Article ID 184102, 2007.

[25] R. Singh, W. Cao, I. Al-Naib, L. Cong, W. Withayachumnankul, and W. Zhang, "Ultrasensitive terahertz sensing with high-Q fano resonances in metasurfaces," *Applied Physics Letters*, vol. 105, no. 17, pp. 1–5, 2014.

[26] S. Behera and K. Kim, "Applications of asymmetric 2D and 3D gold fano resonators and optical realization approach," *Journal of Physics D: Applied Physics*, vol. 52, no. 27, Article ID 275106, 2019.

[27] W. Li, Y. Su, X. Zhai, X. Shang, S. Xia, and L. Wang, "High-Q multiple fano resonances sensor in single dark mode metamaterial waveguide structure," *IEEE Photonics Technology Letters*, vol. 30, no. 23, pp. 2068–2071, 2018.

[28] Y. Kong, J. Cao, W. Qian, C. Liu, and S. Wang, "Multiple fano resonance based optical refractive index sensor composed of micro-cavity and micro-structure," *IEEE Photonics Journal*, vol. 10, no. 6, pp. 1–10, 2018.

[29] S. Shen, Y. Liu, W. Liu, Q. Tan, J. Xiong, and W. Zhang, "Tunable electromagnetically induced reflection with a high Q factor in complementary dirac semimetal metamaterials," *Materials Research Express*, vol. 5, no. 12, 2018.

[30] S. Zhang, D. A. Genov, Y. Wang, M. Liu, and X. Zhang, "Plasmon-induced transparency in metamaterials," *Physical Review Letters*, vol. 101, no. 4, Article ID 47401, 2008.

[31] X. Zhang, Q. Li, W. Cao et al., "Polarization-independent plasmon-induced transparency in a fourfold symmetric terahertz metamaterial," *IEEE Journal of Selected Topics in Quantum Electronics*, vol. 19, no. 1, Article ID 8400707, 2012.

[32] N. Liu, L. Langguth, T. Weiss et al., "Plasmonic analogue of electromagnetically induced transparency at the drude damping limit," *Nature Materials*, vol. 8, no. 9, pp. 758–762, 2009.

[33] X. Duan, S. Chen, H. Yang et al., "Polarization-insensitive and wide-angle plasmonically induced transparency by planar metamaterials," *Applied Physics Letters*, vol. 101, no. 14, Article ID 143105, 2012.

[34] Z. Li, Y. Ma, R. Huang et al., "Manipulating the plasmon-induced transparency in terahertz metamaterials," *Optics Express*, vol. 19, no. 9, pp. 8912–8919, 2011.

[35] X. Liu, J. Gu, R. Singh et al., "Electromagnetically induced transparency in terahertz plasmonic metamaterials via dual excitation pathways of the dark mode," *Applied Physics Letters*, vol. 100, no. 13, Article ID 131101, 2012.

[36] J. Gu, R. Singh, X. Liu et al., "Active control of electromagnetically induced transparency analogue in terahertz metamaterials," *Nature Communications*, vol. 3, no. 1, Article ID 1151, 2012.

[37] X. Yan, M. Yang, Z. Zhang et al., "The terahertz electromagnetically induced transparency-like metamaterials for sensitive biosensors in the detection of cancer cells," *Biosensors and Bioelectronics*, vol. 126, pp. 485–492, 2018.

[38] K. Jin, X. Yan, X. Wang et al., "Dark mode tailored electromagnetically induced transparency in terahertz metamaterials," *Applied Physics B*, vol. 125, no. 5, p. 68, 2019.

[39] B. Bian, S. Liu, H. Zhang, B. Li, and B. Ma, "A new triple-band polarization-insensitive wide-angle microwave metamaterial absorber," *Progress in Electromagnetics Research Symposium*, vol. 5, no. 12, pp. 435–438, 2013.

[40] Y. Cheng, X. S. Mao, C. Wu, L. Wu, and R. Gong, "Infrared non-planar plasmonic perfect absorber for enhanced sensitive refractive index sensing," *Optical Materials*, vol. 53, pp. 195–200, 2016.

[41] W. Wei, F. Yan, S. Tan, Z. Hong, and Y. Hou, "Ultrasensitive terahertz metamaterial sensor based on vertical split ring resonators," *Photonics Research*, vol. 5, no. 6, pp. 571–577, 2017.

[42] C. Jing, H. Nie, C. Peng et al., "Enhancing the magnetic plasmon resonance of three-dimensional optical metamaterials via strong coupling for high-sensitivity sensing," *Journal of Lightwave Technology*, vol. 36, pp. 3481–3485, 2018.

[43] W. Wang, Y. Hou, F. Yan et al., "Symmetry breaking and resonances hybridization in vertical split ring resonator metamaterials and the excellent sensing potential," *Journal of Lightwave Technology*, vol. 37, no. 19, pp. 5149–5157, 2019.

[44] L. Na, M. Mesch, T. Weiss, M. Hentschel, and H. Giessen, "Infrared perfect absorber and its application as plasmonic sensor," *Nano Letters*, vol. 10, no. 7, pp. 2342–2348, 2010.

[45] B. X. Wang, X. Zhai, G. Z. Wang, W. Q. Huang, and L. L. Wang, "A novel dual-band terahertz metamaterial absorber for a sensor application," *Journal of Applied Physics*, vol. 117, no. 1, Article ID 014504, 2015.

[46] R. Zafar, S. Nawaz, G. Singh, A. d'Alessandro, and M. Salim, "Plasmonics-based refractive index sensor for detection of hemoglobin concentration," *IEEE Sensors Journal*, vol. 18, no. 11, pp. 4372–4377, 2018.

[47] X. Wang and J. Wang, "Terahertz metamaterial absorber sensor based on three-dimensional split-ring resonator array and microfluidic channel," *Guangxue Xuebao/Acta Optica Sinica*, vol. 40, no. 19, Article ID 1904001, 2020.

[48] S. Mirzaei, N. G. Green, M. Rotaru, and S. H. Pu, "Detecting and identifying DNA via the THz backbone frequency using a metamaterial-based label-free biosensor," *Proceedings of the SPIE*, vol. 10103, 2017.

[49] A. Feng, Z. Yu, and X. Sun, "Ultranarrow-band metagrating absorbers for sensing and modulation," *Optics Express*, vol. 26, no. 22, pp. 28197–28205, 2018.

[50] S. Tan, F. Yan, W. Wang, H. Zhou, and Y. Hou, "Ultrasensitive sensing with three-dimensional terahertz metamaterial absorber," *Journal of Optics*, vol. 20, no. 5, Article ID 055101, 2018.

[51] H. Tao, A. C. Strikwerda, M. Liu et al., "Performance enhancement of terahertz metamaterials on ultrathin substrates for sensing applications," *Applied Physics Letters*, vol. 97, no. 26, Article ID 261909, 2010.

[52] B. Brian, B. Sepúlveda, Y. Alaverdyan, L. M. Lechuga, and M. Käll, "Sensitivity enhancement of nanoplasmonic sensors in low refractive index substrates," *Optics Express*, vol. 17, no. 3, pp. 2015–2023, 2009.

[53] T. Hu, L. R. Chieffo, M. A. Brenckle, S. M. Siebert, and F. G. Omenetto, "Metamaterials on paper as a sensing platform," *Advanced Materials*, vol. 23, no. 28, pp. 3197–3201, 2011.

[54] Y. K. Srivastava, L. Cong, and R. Singh, "Dual-surface flexible THz fano metasensor," *Applied Physics Letters*, vol. 111, no. 20, Article ID 201101, 2017.

[55] A. Dmitriev, C. Hägglund, S. Chen et al., "Enhanced nanoplasmonic optical sensors with reduced substrate effect," *Nano Letters*, vol. 8, no. 11, pp. 3893–3898, 2008.

[56] M. A. Otte, M.-C. Estévez, L. G. Carrascosa, A. B. González-Guerrero, L. M. Lechuga, and B. Sepúlveda, "Improved biosensing capability with novel suspended nanodisks," *The Journal of Physical Chemistry C*, vol. 115, no. 13, pp. 5344–5351, 2011.

[57] Y. Moritake and T. Tanaka, "Impact of substrate etching on plasmonic elements and metamaterials: preventing red shift and improving refractive index sensitivity," *Optics Express*, vol. 26, no. 3, pp. 3674–3683, 2018.

[58] K. Meng, S. J. Park, A. D. Burnett et al., "Increasing the sensitivity of terahertz split ring resonator metamaterials for dielectric sensing by localized substrate etching," *Optics Express*, vol. 27, no. 16, Article ID 23164, 2019.

[59] W. Wang, F. Yan, S. Tan et al., "Enhancing sensing capacity of terahertz metamaterial absorbers with a surface-relief design," *Photonics Research*, vol. 8, no. 4, pp. 96–104, 2020.

[60] G. M. Whitesides, "The origins and the future of microfluidics," *Nature*, vol. 442, no. 7101, pp. 368–373, 2006.

[61] A. Salim and S. Lim, "Review of recent metamaterial microfluidic sensors," *Sensors*, vol. 18, no. 1, p. 232, 2018.

[62] W. Withayachumnankul, K. Jaruwongrungsee, A. Tuantranont, C. Fumeaux, and D. Abbott, "Metamaterial-based microfluidic sensor for dielectric characterization," *Sensors and Actuators A: Physical*, vol. 189, pp. 233–237, 2013.

[63] H. Zhou, D. Hu, C. Yang et al., "Multi-band sensing for dielectric property of chemicals using metamaterial integrated microfluidic sensor," *Scientific Reports*, vol. 8, no. 1, Article ID 14801, 2018.

[64] X. Hu, G. Xu, L. Wen et al., "Metamaterial absorber integrated microfluidic terahertz sensors," *Laser & Photonics Reviews*, vol. 10, no. 6, pp. 962–969, 2016.

[65] J. Chen, C. Peng, S. Qi et al., "Photonic microcavity-enhanced magnetic plasmon resonance of metamaterials for sensing applications," *IEEE Photonics Technology Letters*, vol. 31, no. 2, pp. 113–116, 2019.

[66] C. Qiu, J. Wu, R. Zhu, L. Shen, and B. Zheng, "Dual-band near-perfect metamaterial absorber based on cylinder MoS2-dielectric arrays for sensors," *Optics Communications*, vol. 451, pp. 226–230, 2019.

[67] X. Chen and W. Fan, "Ultrahigh-Q toroidal dipole resonance in all-dielectric metamaterials for terahertz sensing," *Optics Letters*, vol. 44, no. 23, pp. 5876–5879, 2019.

[68] X. He, Q. Zhang, G. Lu, G. Ying, F. Wu, and J. Jiang, "Tunable ultrasensitive terahertz sensor based on complementary graphene metamaterials," *RSC Advances*, vol. 6, no. 57, pp. 52212–52218, 2016.

Hindawi
Advances in Condensed Matter Physics
Volume 2021, Article ID 3914210, 16 pages
https://doi.org/10.1155/2021/3914210

Research Article

A Novel Elastic Metamaterial with Multiple Resonators for Vibration Suppression

Saman Ahmadi Nooraldinvand,[1] Hamid M. Sedighi ,[1,2] and Amin Yaghootian[1]

[1]*Mechanical Engineering Department, Faculty of Engineering, Shahid Chamran University of Ahvaz, Ahvaz, Iran*
[2]*Drilling Center of Excellence and Research Center, Shahid Chamran University of Ahvaz, Ahvaz, Iran*

Correspondence should be addressed to Hamid M. Sedighi; h.msedighi@scu.ac.ir

Received 6 April 2021; Accepted 19 May 2021; Published 2 June 2021

Academic Editor: Shengxuan Xia

In this paper, two models of elastic metamaterial containing one and two resonators are proposed to obtain the bandgaps with the aim of providing broadband vibration suppression. The model with one DOF is built by assembling several unite cells in which each unite cell consists of a rectangular frame as the base structure and a rack-and-pinion mechanism that is joined to the frame with a linear spring on both sides. In the second model with two DOF, a small mass is added while its center is attached to the center of the pinion on one side and the other side is connected to the rectangular frame via a linear spring. In the first mechanism, the pinion is considered as the single resonator, and in the 2DOF model, on the other hand, the pinion and small mass acted as multiple resonators. By obtaining the governing equations of motion for a single cell in each model, the dynamic behavior of two metastructures is thoroughly investigated. Therefore, the equations of motion for the two models are written in matrix form, and then, the dispersion relations are presented to analyze the influences of system parameters on the bandgaps' starting/ending frequencies. Finally, two models are successfully compared and then numerically simulated via MATLAB-SIMULINK and MSC-ADAMS software. With the aid of closed-form expressions for starting/ending frequencies, the correlation between the system parameters and bandgap intervals can be readily recognized.

1. Introduction

Metamaterials are referred to the types of advanced materials that are synthetically made including small substructures which generally behave like a continuous material. The frequency bands at which acoustic and elastic waves cannot propagate are called bandgap, which is the most prominent feature of metamaterials. The propagation of waves of different wavelengths is controlled by the low/high-frequency bandgaps generated by the metamaterials. Given this unique property, metamaterials can be used in the field of acoustic insulation, filtration of waves, oscillations reduction, and sonic transmission [1–3]. The cell body of an acoustic metamaterial consists of a basic structure in which one or more locally vibrating components are located. Interactions between the base environment and local vibrators enable interesting physical phenomena such as bandwidth, negative effective density, negative modulus of elasticity, directional filtering and wave conduction, increased dissipation, and vibroacoustic attenuation [4, 5]. Basically, two types of local resonators are used: (1) translational resonator and (2) rotary resonator, which cause negative effective density and negative effective elastic modulus, respectively [6]. Huang et al. [7] demonstrated the consequence of using different equivalent models to represent a lattice system consisting of mass-in-mass units. Then they studied the dispersive wave propagation and compared to various equivalent models. They found that, if the classical elastic continuum is utilized to represent the original mass-in-mass structure, the effective mass density will be frequency dependent and may become negative for frequencies near the resonance frequency of the internal mass. In the meantime, if a multi-

displacement microstructure continuum model is utilized, the dispersive behavior of wave propagation and the band gap structure can be adequately described.

Active and passive periodic structures are made up of similar substructures or unit cells that are joined to each other in a similar way. The periodicity of these structures exhibits unique dynamic properties because they can prevent wave propagation and act as a mechanical filter [8]. Wave propagation is not possible in infinite periodic structures at particular frequency intervals. Photonic bandgaps are frequency bands in which acoustic/elastic waves cannot be transmitted. Unlike infinite periodic structures, wave transmission or vibration occurs sparingly if finite periodic structures are excited within the band gaps, which can be examined for frequency response function diagrams to obtain this wave or vibration transmission [9]. Propagation or passbands allow waves along these structures which propagate in certain frequency ranges without attenuation; and stopbands, attenuation bands, or bandgaps are the frequency bands in which waves can be attenuated [10]. In periodic structures, two common methods for generating phononic bandgaps are Bragg scattering and local resonances [9]. The band structure and wave reduction mentioned above are due to these two types of mechanisms that are clearly different from each other [11]. In the high-frequency mode, Bragg bandgaps can be used to filter the waves, but in the low-frequency mode, this is not possible [12]. On the other hand, at much lower frequencies than Bragg scattering, bandgaps can be created by local resonance [9]. Control of resonant-type bandgaps due to local resonance (LR) mechanism is easily possible, unlike Bragg-type bandgaps. In order to adjust the bandgap properties, the properties of the locally resonant structure can be changed. Chen and Chien [12] proposed a mass grid system, and before this new idea was applied to the field of elastic, it was presented in the field of acoustic.

Lazarov and Jensen [10] conducted their study in both linear and nonlinear modes to propagate the wave in one-dimensional chains in which nonlinear oscillators are joined. They found that in the nonlinear state, the bandgap could shift depending on the amplitude and degree of local nonlinearities. Also, the results of their research showed that in the linear mode, the location of the gap is around the resonant frequency which allows the gap to be generated at a lower frequency domain. Casalotti et al. [13] examined an Euler-Bernoulli beam with an arrangement of nonlinear mass-spring substructures attached to investigate the ability of the nonlinear metamaterial beam to absorb multistate vibrations. Beam-connected substructures that act as local resonators or vibration absorbers created bandgaps. At first, they identified the frequency stop bands of the unite cell, and then in order to investigate the multifrequency stopband, the frequency response for the nonlinear metamaterial beam was extracted. They indicated that, for the metamaterial beam, the oscillations related to the lowest three vibration modes were significantly reduced by properly adjusting the constituent parameters of local absorbers. Zhou et al. [14] presented two models of an acoustic metamaterial beam in which local resonators were attached owning to both flexible bandgaps and high static stiffness. Initially, an equivalent model by mass-spring-beam of acoustic metamaterial beam with variable cross section was considered and analyzed analytically. The dispersion relationship of acoustic metamaterial beam was extracted, and the effect of different control parameters on bandgaps was investigated. Then, they simulated and examined a two-dimensional finite element model of acoustic metamaterial beam for the sake of validation in COMSOL Multiphysics. Their results showed that there is good compatibility between the analytical model and the two-dimensional model. Finally, a three-dimensional model of acoustic metamaterial beam was presented and discussed in two forms of equal and unequal thickness to measure the wave attenuation. Huang and Sun [15] studied a multiresonator mass-in-mass grid system and obtained its dispersion curves and bandgap. It was shown that bandgap can be displaced by changing the magnitude of the internal masses and the spring constant. They proposed a monoatomic model equivalent to the original system and found that the effective mass at bandgaps frequencies is negative. Finally, they introduced a microstructure continuous model that can obtain the dispersive behavior and bandgap structure of the original system. According to the study conducted by Sun et al. [16], it was shown that an acoustic absorber based on metamaterial can be thought of as a uniform isotropic beam with a number of very small mass-spring subsystems at different points. They also discussed how to create bandgap by subsystems, the negative effective mass, and stiffness. Their results showed that common mechanical vibration absorbers are the basis of the actual working mechanism of metamaterial beam. Shear forces and bending moments were then created to hold the beam straight and prevent wave propagation. An important and in-depth topical review in the field of active metamaterials and metadevices was performed by Xiao et al. [17]. They reported the advancement of active metadevices and metamaterials ranging from microwave to visible wavelengths, including milestones as well as the state of the art, and finally presented the future prospects together with several emerging tuning strategies and materials.

Most studies of metamaterial models are based on a damper-spring-damper combination. However, this paper uses a new combination of rack-and-pinion mechanism and mass to achieve wider bandgaps and investigate the dynamic behavior of the new combination. In the current research, two models of elastic metamaterials are proposed to obtain broadband bandgaps for vibration suppression. The models are made from a combination of a rack-and-pinion mechanism connected to a concentrated mass. The governing equations of both models with one and two degrees of freedom are solved by MATLAB-SIMULINK and dispersion curves and frequency response diagrams are also drawn. Then, the effect of control parameters on the starting and ending frequencies of the bandgaps is mathematically investigated. Finally, both models are modeled and simulated in MSC-ADAMS software, and the

desired graphs are numerically extracted. There is a satisfactory agreement between the simulated results and those obtained by numerical algorithms.

2. Models: 1DOF and 2DOF

In this section, two models consisting of one- and two-degree-of-freedom elastic metamaterials (EMM) are introduced and discussed. The models include rectangular cells containing a rack-and-pinion mechanism and a concentrated mass. The presence of a rack prevents slipping between the pinion and the cell which converts the transfer motion to a pure rolling motion. The aim of this study is to analytically obtain the bandgaps of the proposed models in order to reduce or eliminate the mechanical vibrations. For both one- and two-degree-of-freedom models, the mathematical models are presented and the staring/ending frequencies of bandgaps are mathematically extracted with close-form expressions.

2.1. One DOF Model of EMM

2.1.1. One DOF Model: Mathematical Formulation. The proposed one-degree-of-freedom model of elastic metamaterials is shown in Figure 1. As shown, the main body of this model consists of rectangular frames with a rack-and-pinion inside. Rectangular frames are then connected by linear springs. On the other hand, the pinion is connected to the walls of the rectangular frame by two linear springs.

The parameters defined for the problem are shown in Figure 2, which represents the unit cell of the one-degree-of-freedom model. Therefore, using Newton's second law, the governing equations of a unit cell are derived as follows:

$$\sum F_x = m_1\ddot{x}_n \Rightarrow -k_1\left(x_n - x_{n-1}\right) - k_1\left(x_n - x_{n+1}\right) - m_2\left(\ddot{x}_n + r\ddot{\theta}\right) = m_1\ddot{x}_n, \tag{1}$$

$$\sum M_O = I_O\ddot{\theta} \Rightarrow -2k_2\left(r\theta\right)r - m_2\left(\ddot{x}_n\right)r = I_O\ddot{\theta}, \tag{2}$$

where m_1 and m_2 are frame and pinion masses, respectively, $r$andθ are the radius and the rotational displacement of pinion, respectively, x_n represents the translational displacement of the nth cell, and I_O denotes the mass moment of inertia of the pinion with respect to the point o.

Now, Equations (1) and (2) are written in a matrix form as follows:

$$\begin{bmatrix} m_1 + m_2 & m_2 r \\ m_2 r & I_O \end{bmatrix}\begin{bmatrix} \ddot{x}_n & \ddot{\theta} \end{bmatrix} + \begin{bmatrix} 2k_1 & 0 \\ 0 & 2k_2 r^2 \end{bmatrix}\begin{bmatrix} x_n \\ \theta \end{bmatrix} + \begin{bmatrix} -k_1\left(x_{n-1} + x_{n+1}\right) \\ 0 \end{bmatrix} = \begin{bmatrix} 0 \\ 0 \end{bmatrix}, \tag{3}$$

and the dimensionless parameters used in this model are defined by

$$\begin{aligned} M &= \frac{m_1}{m_2}, \\ \widehat{I} &= \frac{I_O}{m_2 r^2}, \\ \widehat{K} &= \frac{k_1}{k_2}, \\ \widehat{\omega}_n &= \sqrt{\frac{k_2}{m_2}}, \\ r\overline{x}_n &= x_n, \\ \tau &= \omega t, \\ \widetilde{\omega} &= \frac{\omega}{\widehat{\omega}_n}, \end{aligned} \tag{4}$$

where $\widehat{\omega}_n$ is the local natural frequency, $M, \widehat{I}, \widehat{K}, \overline{x}_n, \tau$, and $\widetilde{\omega}$ are the dimensionless mass, moment of inertia, stiffness, displacement, time, and frequency, respectively. By replacing these dimensionless parameters in Equation (3), the new form of governing equations can be written as follows:

$$\begin{bmatrix} (M+1)\widetilde{\omega}^2 & \widetilde{\omega}^2 \\ \widetilde{\omega}^2 & \widehat{I}\widetilde{\omega}^2 \end{bmatrix}\begin{bmatrix} \dfrac{d^2\overline{x}_n}{d\tau^2} \\ \dfrac{d^2\theta}{d\tau^2} \end{bmatrix} + \begin{bmatrix} 2\widehat{K} & 0 \\ 0 & 2 \end{bmatrix}\begin{bmatrix} \overline{x}_n \\ \theta \end{bmatrix} + \begin{bmatrix} -\widehat{K}\left(\overline{x}_{n-1} + \overline{x}_{n+1}\right) \\ 0 \end{bmatrix} = \begin{bmatrix} 0 \\ 0 \end{bmatrix}. \tag{5}$$

2.1.2. One DOF Model: Dispersion Properties. In this section, the solution corresponding to the harmonic wave for the

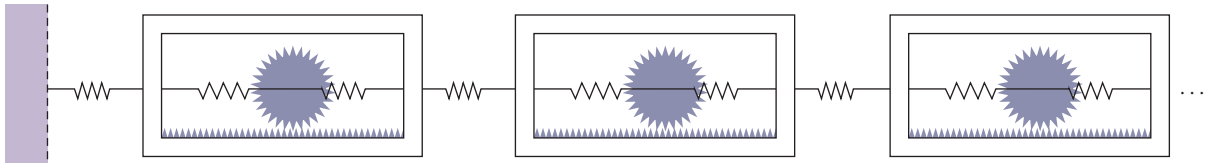

Figure 1: A schematic of the metamaterial arrangement of the 1DOF model.

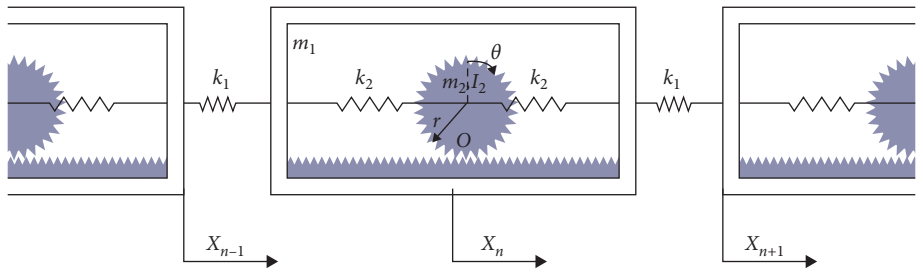

Figure 2: A schematic of a unite cell of the 1DOF model.

1DOF model is defined for extracting the dispersion relations and the bandgap frequencies:

$$\begin{bmatrix} \overline{x}_n \\ \theta \end{bmatrix} = \begin{bmatrix} \overline{x}_n^{\circ} \\ \theta^{\circ} \end{bmatrix} e^{i(\mathrm{qa}.n+\tau)} + c.c, \qquad [\overline{x}_{n\pm1}] = [\overline{x}_{n\pm1}^{\circ}] e^{i(\mathrm{qa}.n+\tau)} + c.c, \tag{6}$$

where $\overline{x}_n^{\circ}$ and θ° are the steady-state amplitude of the solution, qa is the phase factor, and $n$represents the periodic number. Moreover, $a.n$ indicates the distance between $n$thcell from the origin (support) [18–22]. Substituting Equations (6) into (5), the new form of the governing equation in its matrix form is as follows:

$$\begin{bmatrix} (M+1)\widetilde{\omega}^2 & \widetilde{\omega}^2 \\ \widetilde{\omega}^2 & \widehat{I}\widetilde{\omega}^2 \end{bmatrix} \begin{bmatrix} \overline{x}_n^{\circ}(-1)e^{i(\mathrm{qa}.n+\tau)} + c.c \\ \theta^{\circ}(-1)e^{i(\mathrm{qa}.n+\tau)} + c.c \end{bmatrix} + \begin{bmatrix} 2\widehat{K} & 0 \\ 0 & 2 \end{bmatrix} \begin{bmatrix} \overline{x}_n^{\circ} e^{i(\mathrm{qa}.n+\tau)} + c.c \\ \theta^{\circ} e^{i(\mathrm{qa}.n+\tau)} + c.c \end{bmatrix} + \begin{bmatrix} -\widehat{K}\left(\overline{x}_n^{\circ} e^{i\mathrm{qa}(n-1)} e^{i\tau} + \overline{x}_n^{\circ} e^{i\mathrm{qa}(n+1)} e^{i\tau} + c.c\right) \\ 0 \end{bmatrix} = \begin{bmatrix} 0 \\ 0 \end{bmatrix}. \tag{7}$$

Now, by factoring and arranging the different expressions in Equation (7), the final form of the equations of motion for the considered system is given by

$$\begin{bmatrix} -(M+1)\widetilde{\omega}^2 + 2\widehat{K} - \widehat{K}(2\cos(\mathrm{qa})) & -\widetilde{\omega}^2 \\ -\widetilde{\omega}^2 & -\widehat{I}\widetilde{\omega}^2 + 2 \end{bmatrix} \begin{bmatrix} \overline{x}_n^{\circ} \\ \theta^{\circ} \end{bmatrix} e^{i(\mathrm{qa}.n+\tau)} + c.c = \begin{bmatrix} 0 \\ 0 \end{bmatrix}. \tag{8}$$

The dispersion relation for the 1DOF model can be obtained from Equation (8). For a nontrivial solution, the determinant of the coefficient matrix must be equal to zero. Therefore, the dispersion relation is extracted as

$$(\widehat{I}(1+M)-1)\widetilde{\omega}^4 + 2(-M-1-\widehat{I}\widehat{K}(1+\cos(\mathrm{qa})))\widetilde{\omega}^2 + 4\widehat{K}(1-\cos(\mathrm{qa})) = 0. \tag{9}$$

By solving Equation (9) for $\widetilde{\omega}$, the relation for the acoustic and optical frequencies of the EMM can be achieved as described in Equations (10) and (11). Then, by employing the obtained closed-form expressions, the dispersion curves for the 1DOF model are shown in Figure 3.

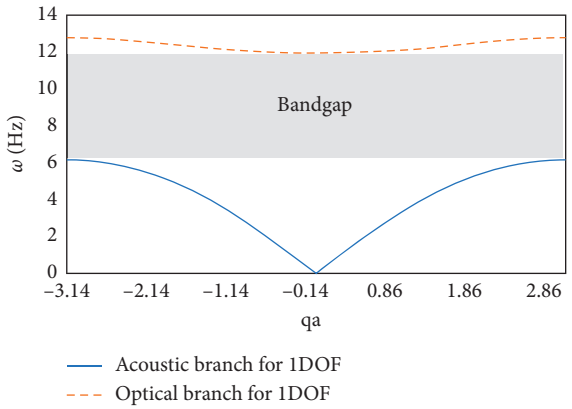

Figure 3: Dispersion curves for the 1DOF model.

where

$$\widetilde{\omega}_{\text{Acoustic}} = \sqrt{\frac{\Delta - \sqrt{\Phi}}{\Psi}}, \tag{10}$$

$$\widetilde{\omega}_{\text{Optical}} = \sqrt{\frac{\Delta + \sqrt{\Phi}}{\Psi}}, \tag{11}$$

$$\begin{aligned}
\Delta &= M + \widehat{I}\widehat{K} - \widehat{I}\widehat{K}\cos(\text{qa}) + 1,\\
\Psi &= \widehat{I} + \widehat{I}M - 1,\\
\Phi &= \widehat{I}^2\widehat{K}^2\cos^2(\text{qa}) + \left(-2\widehat{I}^2\widehat{K}^2 + 4\widehat{I}\widehat{K} - 4\widehat{K}\right)\cos(\text{qa}) + (1 + 4\widehat{K} + 2M - 2\widehat{I}\widehat{K} - \widehat{I}\widehat{K}M).
\end{aligned} \tag{12}$$

Equations (10) and (11) express the acoustic and optical frequency branches, respectively. Low-frequency and high-frequency dispersive curves are then presented by $\widetilde{\omega}_{\text{Acoustic}}$ and $\widetilde{\omega}_{\text{Optical}}$, respectively [1]. In the above equations, at the point of qa = $\pm\pi$, the slope of the dispersion curve, namely, the velocity of the traveling wave, is equal to zero. This means the wave cannot propagate, similar to what happened at the bandgaps. This area is the first Brillouin zone's boundary. Hence, substituting qa = π and qa = 0 into Equations (10) and (11), and then solving these expressions, the starting and ending frequencies of the bandgaps for the 1DOF model are extracted [1, 20].

2.2. Two DOF Model of EMM

2.2.1. Two DOF Model: Mathematical Formulation. In this section, a model of two degrees of freedom of EMM is presented (see Figure 4). This model is an extended model of the first model discussed in the previous section. The unite cell of the model is made of rectangular frames with a rack-and-pinion inside it connected to a concentrated mass. As shown in Figure 5, the pinion and concentrated mass are joined to the rectangular frame by a linear spring with stiffness of k_2. In addition, the rectangular frames are connected to each other by a linear spring with stiffness of k_1 and create an integrated metastructure. Therefore, the governing equations of a unit cell can be described as follows:

$$\sum F_x = m_1\ddot{x}_n \Rightarrow -k_1(x_n - x_{n-1}) - k_1(x_n - x_{n+1}) - m_2\left(\ddot{x}_n + r\ddot{\theta}\right) - m_3(\ddot{x}_n + \ddot{x}) = m_1\ddot{x}_n, \tag{13}$$

$$\sum M_O = I_O\ddot{\theta} \Rightarrow -2k_2(r\theta)r + (k_2x)r - m_2(\ddot{x}_n)r = I_O\ddot{\theta}, \tag{14}$$

$$\sum F_x = m_3\ddot{x} \Rightarrow -m_3\ddot{x}_n - 2k_2x + k_2r\theta = m_3\ddot{x}, \tag{15}$$

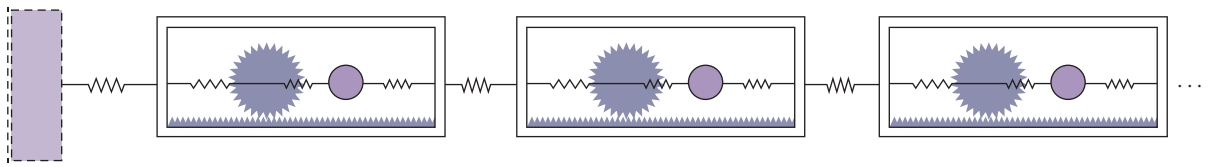

Figure 4: A schematic of the metamaterial arrangement of the 2DOF model.

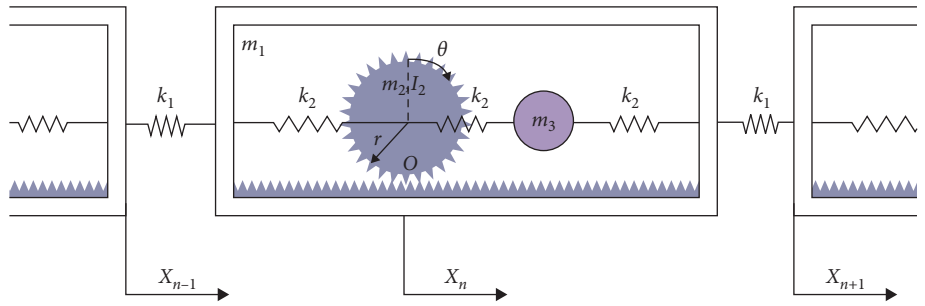

Figure 5: A schematic of a unite cell of 2DOF model.

where $m_3$is the concentrated mass, and x denotes the translational displacement of concentrated mass.

Now, Equations (13) to (15) are written in matrix form as follows:

$$\begin{bmatrix} m_1+m_2+m_3 & m_2 r & m_3 \\ m_2 r & I_O & 0 \\ m_3 & 0 & m_3 \end{bmatrix} \begin{bmatrix} \ddot{x}_n \\ \ddot{\theta} \\ \ddot{x} \end{bmatrix} + \begin{bmatrix} 2k_1 & 0 & 0 \\ 0 & 2k_2 r^2 & -k_2 r \\ 0 & -k_2 r & 2k_2 \end{bmatrix} \begin{bmatrix} x_n \\ \theta \\ x \end{bmatrix} + \begin{bmatrix} -k_1 (x_{n-1} + x_{n+1}) \\ 0 \\ 0 \end{bmatrix} = \begin{bmatrix} 0 \\ 0 \\ 0 \end{bmatrix}. \tag{16}$$

To express the problem in the dimensionless form, the following nondimensional parameters are defined for the 2DOF model:

$$\begin{aligned} \overline{m}_1 &= \frac{m_2 + m_3}{m_1}, \\ \overline{m}_2 &= \frac{m_2}{m_1}, \\ \overline{I} &= \frac{I_O}{m_2 r^2}, \\ \overline{K} &= \frac{k_2}{k_1}, \\ \omega_{n1} &= \sqrt{\frac{k_1}{m_1}} \\ \omega_{n2} &= \sqrt{\frac{2k_2}{m_3}}, \end{aligned}$$

$$\begin{aligned} r\overline{x}_n &= x_n, \\ r\overline{x} &= x, \\ \tau &= \omega t, \\ \overline{\omega}_1 &= \frac{\omega}{\omega_{n1}}, \\ \overline{\omega}_2 &= \frac{\omega}{\omega_{n2}}, \end{aligned} \tag{17}$$

where ω_{n1} and ω_{n2} stand for the natural local frequencies of the first and second modes, respectively, $\overline{m}_1$ and $\overline{m}_2$ are defined as the ratio of the total mass of the pinion and the concentrated mass to the mass of the rectangular frame and pinion-to-frame mass ratio, respectively, $\overline{I}, \overline{K}, \overline{x}_n, \overline{x}$, and τ are the dimensionless moment of inertia, stiffness, displacement for cell, displacement for concentrated mass, and dimensionless time, and $\overline{\omega}_1$ and $\overline{\omega}_2$ denote the first and second dimensionless frequencies, respectively. Using the introduced dimensionless parameters, Equation (16) can be rewritten in a dimensionless form as follows:

$$\begin{bmatrix} (1+\overline{m}_1)\overline{\omega}_1^2 & \overline{m}_2\overline{\omega}_1^2 & (\overline{m}_1-\overline{m}_2)\overline{\omega}_1^2 \\ \overline{\omega}_1^2 & \overline{I}\overline{\omega}_1^2 & 0 \\ \overline{\omega}_2^2 & 0 & \overline{\omega}_2^2 \end{bmatrix} \begin{bmatrix} \dfrac{d^2\overline{x}_n}{d\tau^2} \\ \dfrac{d^2\theta}{d\tau^2} \\ \dfrac{d^2\overline{x}}{d\tau^2} \end{bmatrix} + \begin{bmatrix} 2 & 0 & 0 \\ 0 & \dfrac{2\overline{K}}{\overline{m}_2} & -\dfrac{\overline{K}}{\overline{m}_2} \\ 0 & -\dfrac{1}{2} & 1 \end{bmatrix} \begin{bmatrix} \overline{x}_n \\ \theta \\ \overline{x} \end{bmatrix} + \begin{bmatrix} -(\overline{x}_{n-1}+\overline{x}_{n+1}) \\ 0 \\ 0 \end{bmatrix} = \begin{bmatrix} 0 \\ 0 \\ 0 \end{bmatrix}. \tag{18}$$

2.2.2. Two DOF Model: Dispersion Properties. In this section, the solutions corresponding to the harmonic wave for the 2DOF model are presented as follows for extracting the dispersion relations as well as the bandgap frequencies:

$$\begin{bmatrix} \overline{x}_n \\ \theta \\ \overline{x} \end{bmatrix} = \begin{bmatrix} \overline{x}_n^\circ \\ \theta^\circ \\ \overline{x}^\circ \end{bmatrix} e^{i(\mathrm{qa}.n+\tau)} + c.c, \qquad [\overline{x}_{n\pm1}] = [\overline{x}_{n\pm1}^\circ] e^{i(\mathrm{qa}.n+\tau)} + c.c. \tag{19}$$

Similar to the previous section, $\overline{x}_n^\circ$, θ°, and $\overline{x}^\circ$ represent the steady-state amplitude of the solutions. Substituting Equations (19) into (18), the new forms of the governing equations using matrix notation are given by

By simplifying Equation (1), the final form of the governing equations yields

$$\begin{bmatrix} (1+\overline{m}_1)\overline{\omega}_1^2 & \overline{m}_2\overline{\omega}_1^2 & (\overline{m}_1-\overline{m}_2)\overline{\omega}_1^2 \\ \overline{\omega}_1^2 & \overline{I}\overline{\omega}_1^2 & 0 \\ \overline{\omega}_2^2 & 0 & \overline{\omega}_2^2 \end{bmatrix} \begin{bmatrix} \overline{x}_n^\circ (-1)e^{i(\mathrm{qa}.n+\tau)} + c.c \\ \theta^\circ (-1)e^{i(\mathrm{qa}.n+\tau)} + c.c \\ \overline{x}^\circ (-1)e^{i(\mathrm{qa}.n+\tau)} + c.c \end{bmatrix}$$

$$+ \begin{bmatrix} 2 & 0 & 0 \\ 0 & \dfrac{2\overline{K}}{\overline{m}_2} & -\dfrac{\overline{K}}{\overline{m}_2} \\ 0 & -\dfrac{1}{2} & 1 \end{bmatrix} \begin{bmatrix} \overline{x}_n^\circ e^{i(\mathrm{qa}.n+\tau)} + c.c \\ \theta^\circ e^{i(\mathrm{qa}.n+\tau)} + c.c \\ \overline{x}^\circ e^{i(\mathrm{qa}.n+\tau)} + c.c \end{bmatrix} + \begin{bmatrix} -\left(\overline{x}_n^\circ e^{i\mathrm{qa}(n-1)}e^{i\tau} + \overline{x}_n^\circ e^{i\mathrm{qa}(n+1)}e^{i\tau} + c.c\right) \\ 0 \\ 0 \end{bmatrix} = \begin{bmatrix} 0 \\ 0 \\ 0 \end{bmatrix}. \tag{20}$$

$$\begin{bmatrix} -(1+\overline{m}_1)\overline{\omega}_1^2 + 2 - 2\cos(\mathrm{qa}) & -\overline{m}_2\overline{\omega}_1^2 & -(\overline{m}_1-\overline{m}_2)\overline{\omega}_1^2 \\ -\overline{\omega}_1^2 & -\overline{I}\overline{\omega}_1^2 + \dfrac{2\overline{K}}{\overline{m}_2} & -\dfrac{\overline{K}}{\overline{m}_2} \\ -\overline{\omega}_2^2 & -\dfrac{1}{2} & 1-\overline{\omega}_2^2 \end{bmatrix} \begin{bmatrix} \overline{x}_n^\circ \\ \theta^\circ \\ \overline{x}^\circ \end{bmatrix} e^{i(\mathrm{qa}.n+\tau)} + c.c = \begin{bmatrix} 0 \\ 0 \\ 0 \end{bmatrix}. \tag{21}$$

Dispersion relation for the 2DOF model can be then obtained by manipulating Equation (21). For a nonzero solution, the determinant of the coefficient matrix should be set to zero. Therefore, the dispersion relation is extracted as follows:

$$A\omega^6 + \left(B\omega_{n1}^2 + C\omega_{n2}^2\right)\omega^4 + \left(D\omega_{n1}^2\omega_{n2}^2 + E\omega_{n1}^4\right)\omega^2 + F = 0, \tag{22}$$

where

$$
\begin{aligned}
A &= 2\overline{m}_2\left(\overline{m}_2\overline{I} - 1 - \overline{I}\right),\\
B &= -2\overline{K}\left(2 + \overline{m}_2\right) + 4\overline{m}_2\overline{I}\left(1 - \cos\left(\mathrm{qa}\right)\right),\\
C &= \overline{m}_2\left(\overline{m}_2 + 2\overline{I}\right) + \overline{m}_1\overline{m}_2\left(1 + 2\overline{I}\right),\\
D &= 3\overline{K}\left(1 + \overline{m}_1\right) - 4\overline{m}_2\overline{I}\left(1 - \cos\left(\mathrm{qa}\right)\right),\\
E &= 8\overline{K}\left(1 - \cos\left(\mathrm{qa}\right)\right),\\
F &= -6\overline{K}\left(1 - \cos\left(\mathrm{qa}\right)\right)\omega_{n1}^4\omega_{n2}^2.
\end{aligned}
\tag{23}
$$

Similar to the explanations given for the one-degree-of-freedom model, Equation (22) shows the relationship between ω and qa. By plotting this equation, the dispersion curves are then available. By replacing $\mathrm{qa} = \pi$ in Equation (22), the expressions for the starting frequencies can be achieved as follows:

$$
\begin{aligned}
F_{s1} &= \sqrt{\frac{H}{3A} - \frac{1}{2}\left(\frac{C}{B} + B\right)},\\
F_{s2} &= \sqrt{\frac{H}{3A} + \left(\frac{C}{B} + B\right)}.
\end{aligned}
\tag{24}
$$

Now, by substituting $\mathrm{qa} = 0$ in Equation (22), the correlations between the system parameters and ending frequencies are given by

$$
\begin{aligned}
F_{e1} &= \frac{\sqrt{K - \sqrt{L}}}{2A},\\
F_{e2} &= \frac{\sqrt{K + \sqrt{L}}}{2A},
\end{aligned}
\tag{25}
$$

where

$$
\begin{aligned}
A &= 2\overline{m}_2^2\overline{I} + 2\overline{m}_2^2 + 2\overline{m}_2\overline{I},\\
B &= \left(E + \left(\left(E + D - F\right)^2 - C^3\right)^{1/2} + D - F\right)^{1/3},\\
C &= \frac{1}{3A}\left(\frac{H^2}{3A} + G\right),\\
D &= \frac{GH}{6A^2},\\
E &= \frac{H^3}{27A^3},\\
F &= \frac{6K\omega_{n1}^4\omega_{n2}^2}{A},\\
G &= 16K\omega_{n1}^4 + \left(3K + 3K\overline{m}_1 - 8\overline{m}_2\overline{I}\right)\omega_{n1}^2\omega_{n2}^2,\\
H &= \overline{m}_2\omega_{n2}^2\left(\overline{m}_2 + \overline{m}_1 + 2\overline{I} + 2\overline{m}_1\overline{I}\right) + \omega_{n1}^2\left(-4\overline{K} - 2\overline{K}\overline{m}_2 + 8\overline{m}_2\overline{I}\right),\\
I &= \overline{m}_1^2\overline{m}_2^2\left(2\overline{I} + 1\right)^2 + \left(2\overline{m}_1\overline{m}_2^3 + 4\overline{m}_1\overline{m}_2^2\overline{I}\right)\left(2\overline{I} + 1\right) + \left(2\overline{I}\overline{m}_2 + \overline{m}_2^2\right)^2,\\
J &= 4\overline{K}\overline{m}_1\overline{m}_2^2\left(4\overline{I} + 5\right) + 8\overline{K}\overline{m}_1\overline{m}_2\left(\overline{I} - 1\right) + 16\overline{K}\overline{m}_2^2\left(\overline{I} + 1\right) + 8\overline{K}\overline{m}_2\overline{I} - 4\overline{K}\overline{m}_2^3,\\
K &= H - 8\overline{m}_2\overline{I}\omega_{n1}^2,\\
L &= 16\overline{K}\left(\frac{\overline{m}_2^2}{4} + \overline{m}_2 + 1\right)\omega_{n1}^4 + I\omega_{n2}^4 + J\omega_{n1}^2\omega_{n2}^2.
\end{aligned}
\tag{26}
$$

3. The Integrity of One and Two DOF Models

To verify the results of this study extracted by mathematical modeling, both elastic metamaterials are modeled and simulated in MSC-ADAMS software under the assumption of rigid dynamics, as shown in Figures 6–9. Furthermore, the frequency response analysis (FRA) is performed for both models and frequency diagrams are then plotted. In the following section, the transient specifications of the system are expressed by parameter Π and the ratio of the fifth cell displacement to the displacement of the first cell and then compared with numerical solutions.

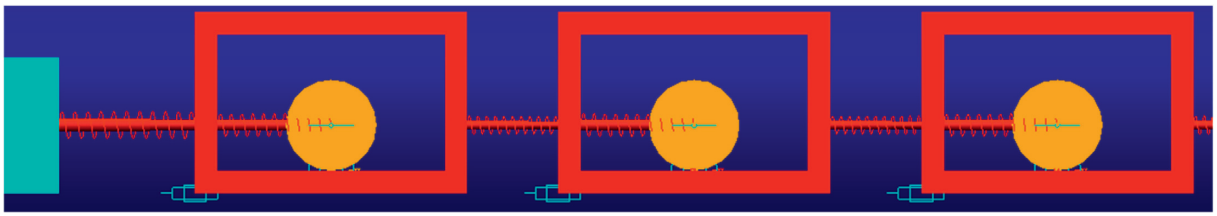

Figure 6: A schematic of the EMM arrangement of 1DOF model-MSC-ADAMS software.

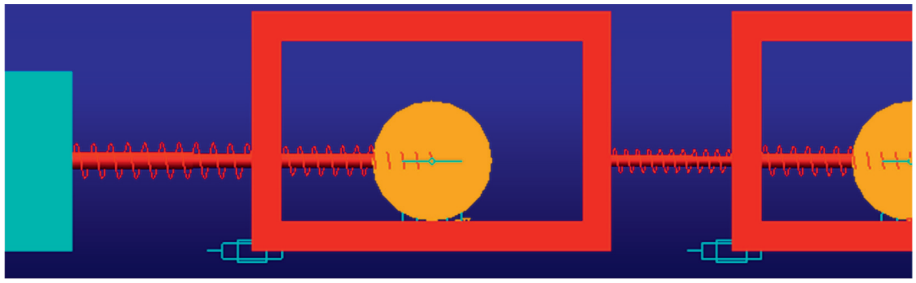

Figure 7: A schematic of a unite cell of 1DOF model-MSC-ADAMS software.

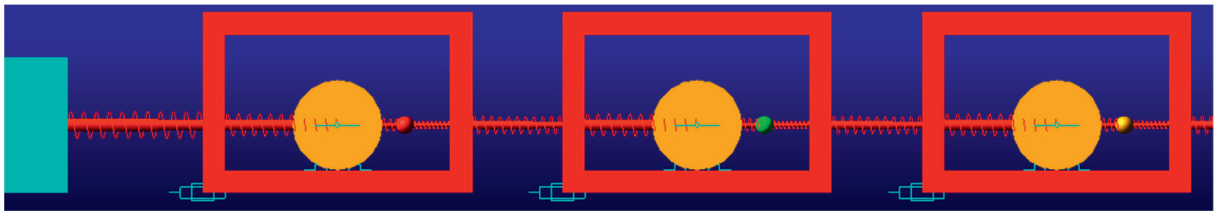

Figure 8: A schematic of the EMM arrangement of 2DOF model-MSC-ADAMS software.

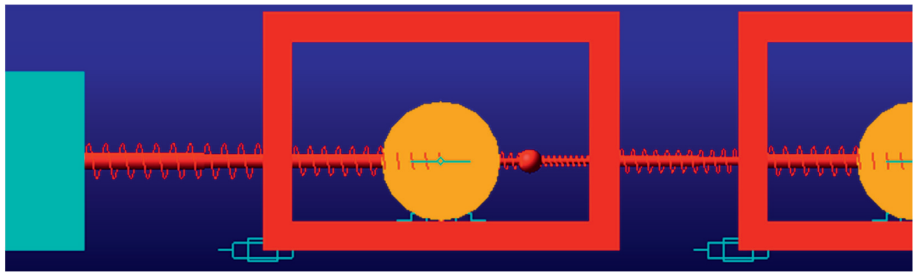

Figure 9: A schematic of a unite cell of 2DOF model-MSC-ADAMS software.

For numerical simulations, MATLAB/Simulink software is utilized, and the governing equations of proposed models are solved numerically. The block diagrams drawn by MATLAB/Simulink models are displayed in Figure 10. It is worth mentioning that each section in the diagram contains the equations governing the dynamics of a single cell.

For both models, the frequency response diagrams obtained from numerical solutions and simulations are plotted in Figures 11 and 12. As indicated, both analyses provide the same intervals for system bandgaps, demonstrating the satisfactory agreement between the results of both procedures which indicates the integrity of our mathematical modeling as well as numerical calculations.

4. Results and Discussion

After verifying the soundness of the numerical solutions, the dispersion characteristics and the effect of different system parameters on the bandgap intervals are comprehensively

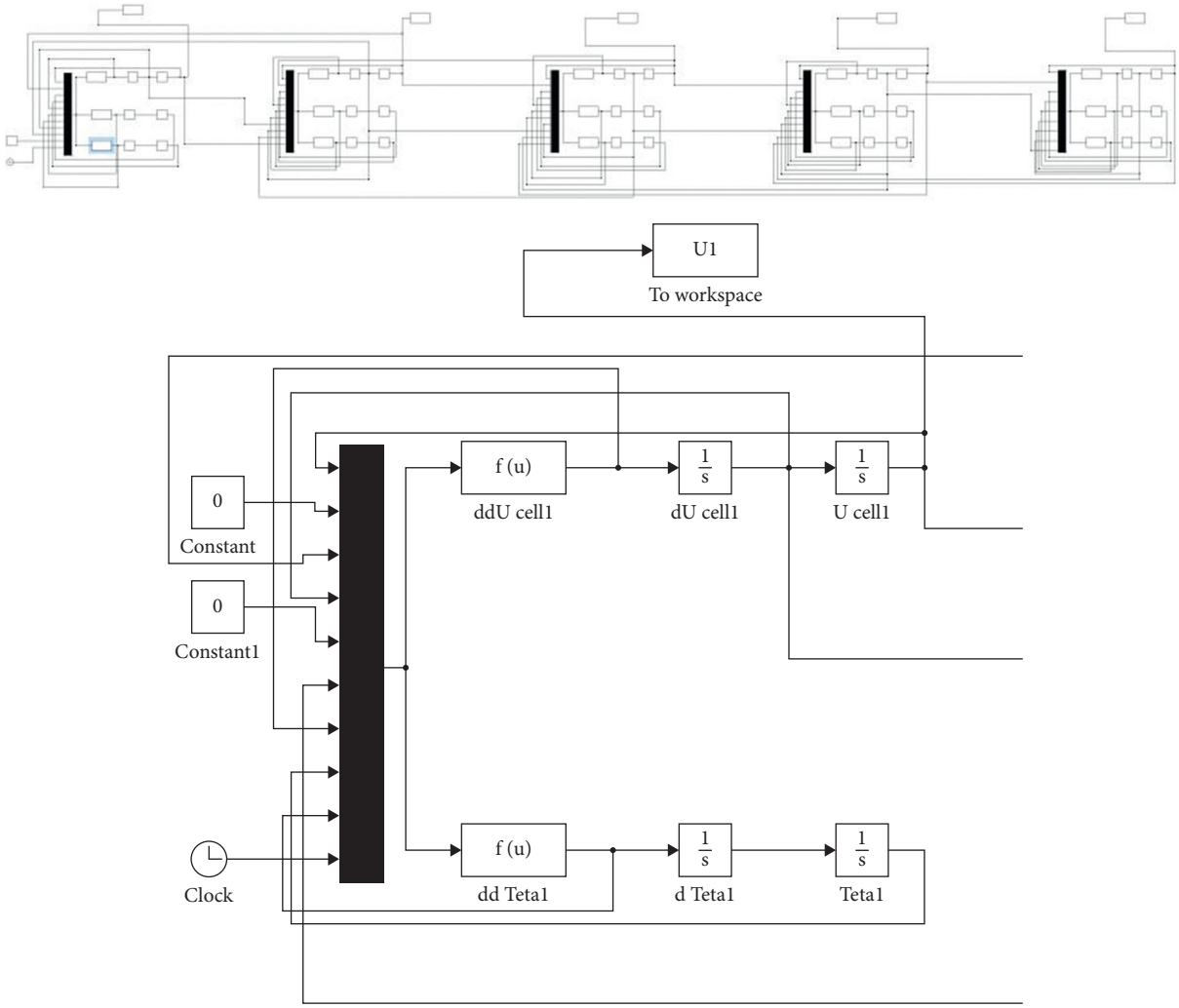

(a)

Figure 10: Continued.

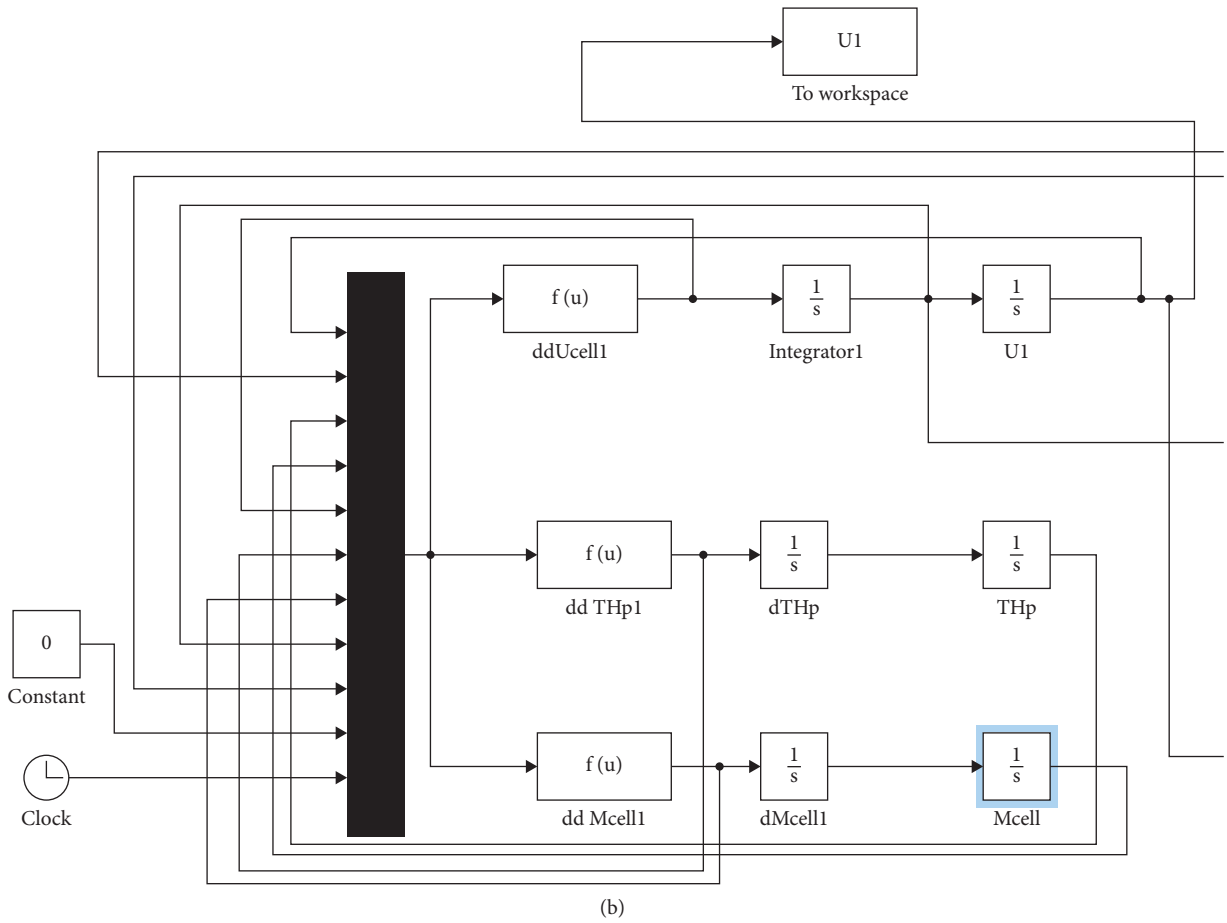

Figure 10: Block diagrams plotted in MATLAB/Simulink for the numerical solution of governing equations. (a) 1DOF model. (b) 2DOF model, array of cells (top) and a unit cell (bottom).

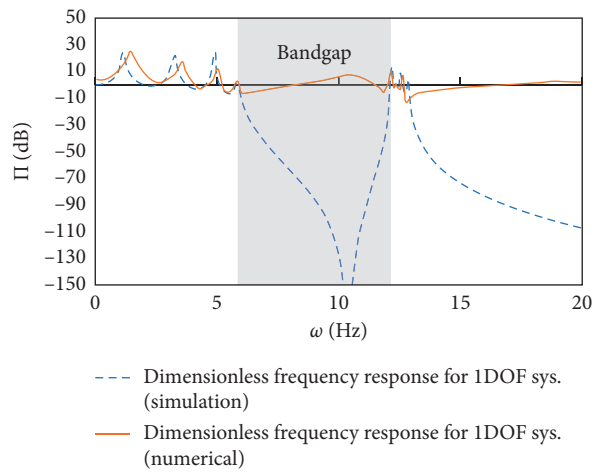

Figure 11: FRA for 1DOF model, comparison of numerical solution (MATLAB/Simulink) with simulation (MSC-ADAMS).

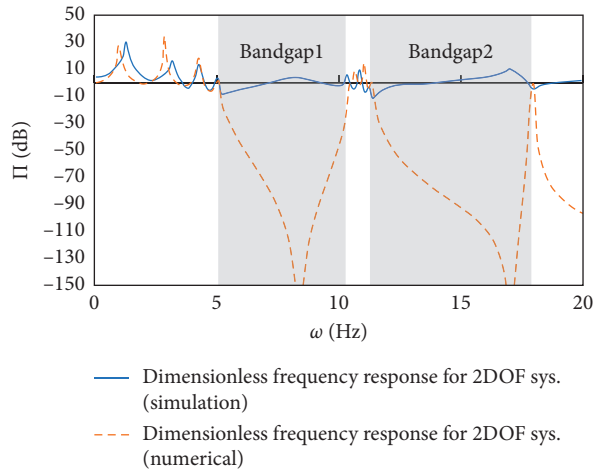

Figure 12: FRA for 2DOF model, comparison of numerical solution (MATLAB/Simulink) with simulation (MSC-ADAMS).

studied. In this section, it is aimed to examine the bandgaps of the introduced models and demonstrate in which conditions they can be extended or transmitted.

4.1. One DOF Model of EMM

4.1.1. Dispersion Curve for the 1DOF Model. Figure 2 shows the dispersion curves of the one-degree-of-freedom model, which shows the acoustic and optical wave modes as well as the bandgap interval. The values of the selected parameters are $M = 1.56, \widehat{I} = 1.5, \widehat{K} = 0.35$, and $\widehat{\omega}_n = 8.9$. Considering these parameters, the bandgap of the one-degree-of-freedom model is placed between the frequencies of 6.15 to 11.94 (Hz), which is the same as the frequency range obtained from Figure 11.

4.1.2. The Effect of System Parameters in the 1DOF Model. The surfaces drawn in Figure 13 exhibit the effect of different dimensionless parameters on the starting and ending frequencies of their corresponding bandgaps. The top and bottom surfaces indicate the starting and ending frequencies, respectively, and the distance between them indicates the bandgap interval of the 1DOF model. As can be seen in Figure 13, there is a direct relationship between the bandgap and the dimensionless stiffness, meaning that as the dimensionless stiffness increases, the bandgap is also enhanced. On the other hand, by increasing the dimensionless mass, the bandgap decreases. It is deduced that the stiffness parameter has a positive effect on the expansion of the bandgap and the effect of the mass parameter is to weaken the bandgap interval. Moreover, according to the illustrated results, in general, the dimensionless moment of inertia directly affects the bandgap range, which means that as the dimensionless moment of inertia increases, the bandgap of the model is also enlarged. Although the bandgap interval slightly decreases at the lower values, when the dimensionless moment of inertia takes the higher values, this interval is then enhanced satisfactorily.

4.2. 2DOF Model of EMM

4.2.1. Dispersion Curve for the 2DOF Model. In order to display the dispersion curves of the modified model with multiple resonators, one can solve Equation (22) for ω and extract the desired curves. The values of the selected parameters are $\overline{m}_1 = 1.04, \overline{m}_2 = 0.64, \overline{I} = 1.5$, and $\overline{K} = 2.86$, $\omega_{n1} = 4.2\,(\text{rad/s}), \omega_{n2} = 15.9\,(\text{rad/s})$. Considering the above parameters, the bandgap starting frequencies (F_{s1} and F_{s2}) are calculated by substituting qa = $\pm\,\pi$ in the acoustic and optical wave modes, respectively. The resulting plots are shown in Figure 14 by Ds(1) and Ds(2), respectively. In addition, the bandgap ending frequencies (F_{e1} and F_{e2}) are also extracted by replacing qa = 0 in two optical roots of Equation (22), respectively. The plotted results are illustrated in Figure 14 by Ds(2) and Ds(3), respectively. As indicated in Figure 14, the difference between the first starting frequency and the first ending frequency demonstrates the first bandgap, and the difference between the second starting frequency and the second ending frequency represents the second bandgap. According to the illustrated results in Figure 12, one can find that there is a small area between the first and second bandgaps. This consequence is also demonstrated in Figure 14 with a slight difference between the highest and lowest points of Ds(2). The slight difference leads to the flattening of the Ds(2) curve.

4.2.2. Comparison of Dispersion Curves for Two Models. As shown in Figure 15, by adding the concentrated mass and modifying the 1DOF model to a 2DOF model, two bandgaps are created in the dynamics of the new model, which allows us to reduce or suppress the vibrations of the modified system in more frequency ranges. From the comparison between the dispersion curves of both models, one can conclude that the first bandgap in the two-degree-of-freedom model starts and ends at lower frequencies than that of the one-degree-of-freedom model.

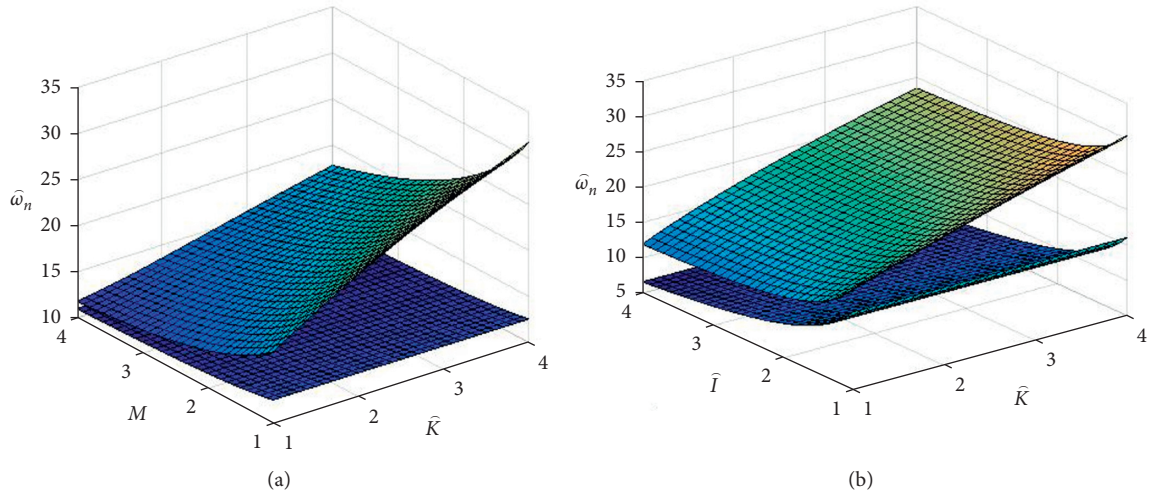

Figure 13: The effect of changing (a) $\widehat{K}$ and M and (b) $\widehat{K}$ and $\widehat{I}$ on the starting and ending frequencies of the bandgap for 1DOF model.

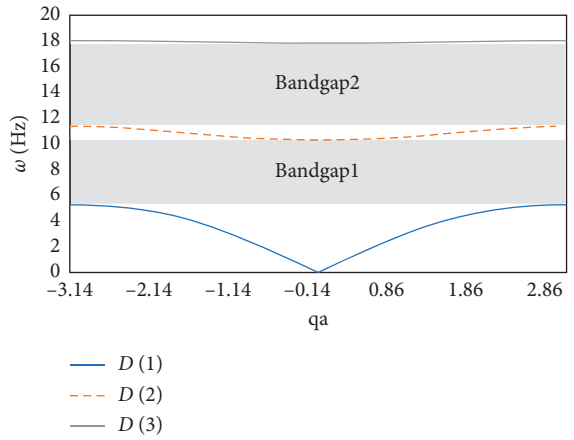

Figure 14: Dispersion curves for the 2DOF model.

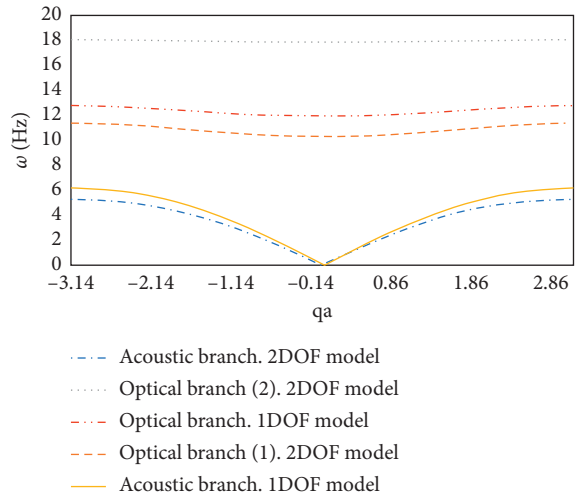

Figure 15: Comparison of dispersion curves in two models.

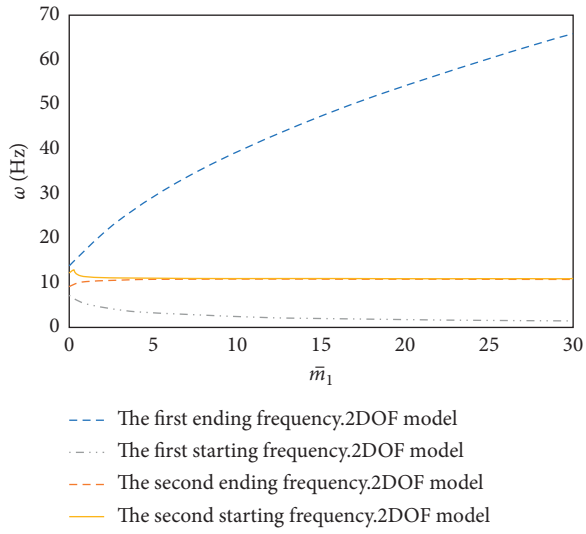

Figure 16: The effect of $\overline{m}_1$ parameter on bandgap for the 2DOF model.

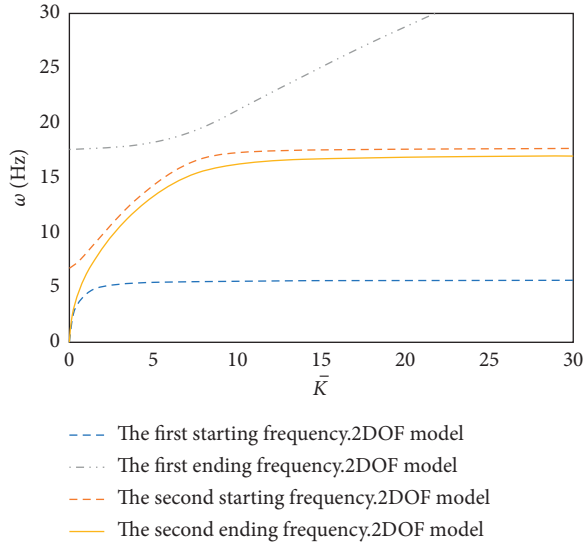

Figure 17: The effect of $\overline{K}$ parameter on bandgap for the 2DOF model.

4.2.3. The Effect of System Parameters in the 2DOF Model. Figure 16 displays well that when the parameter $\overline{m}_1$ shifts upward, the first starting frequency also increases and the first ending frequency reduces, which satisfactorily expands the first bandgap of the modified model. On the other hand, by increasing the first bandgap, the second one decreases and the starting and ending frequencies eventually reach a constant value.

With increasing the parameter $\overline{K}$, the first bandgap can be extended to cover a larger frequency range, as shown in Figure 17, although the first starting frequency will eventually approach a constant value. However, the change in the second bandgap of the model does not show the same trend, eventually converges to an almost constant value, and no longer changes significantly.

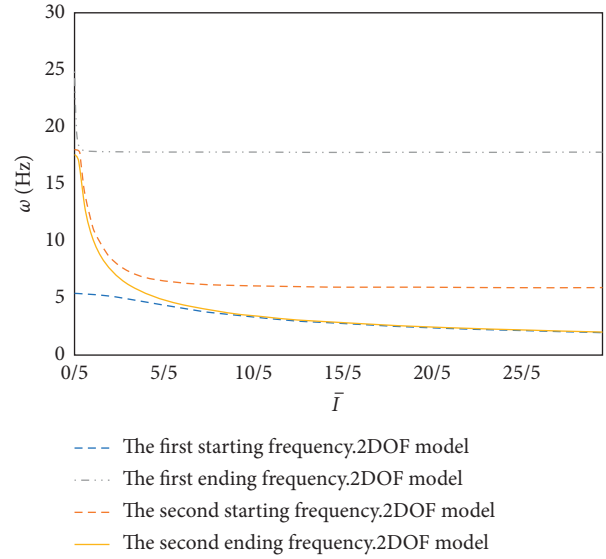

Figure 18: The effect of $\overline{I}$ parameter on bandgap for the 2DOF model.

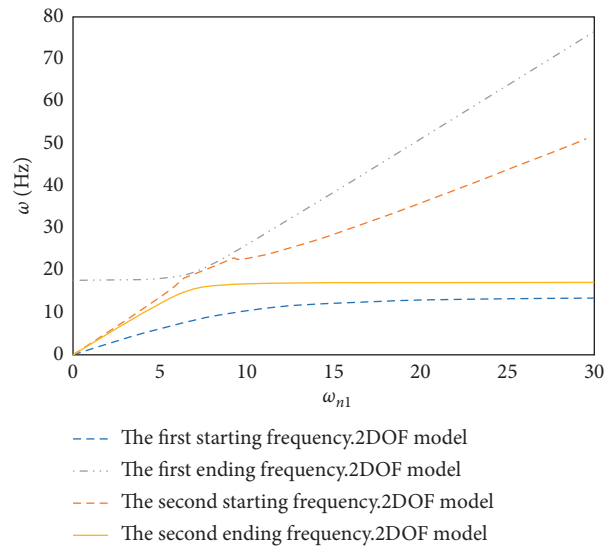

Figure 19: The effect of ω_{n1} parameter on bandgap for the 2DOF model.

For the sake of extending the first and second bandgaps of the modified model, the dimensionless moment of inertia $\overline{I}$ has to be increased. As indicated in Figure 18, by continuing the process of increasing the dimensionless moment of inertia, the first ending and the second starting frequencies will not change and take a constant value.

As the first and second local frequencies increase, the same behavior cannot be observed in the first bandgap of this model, although it decreases with small values and follows an increasing trend at higher values (see Figures 19 and 20). In general, it can be inferred that the first bandgap is expanded. Finally, it is found that with the increase of the first local frequency, the expansion of the second bandgap is not

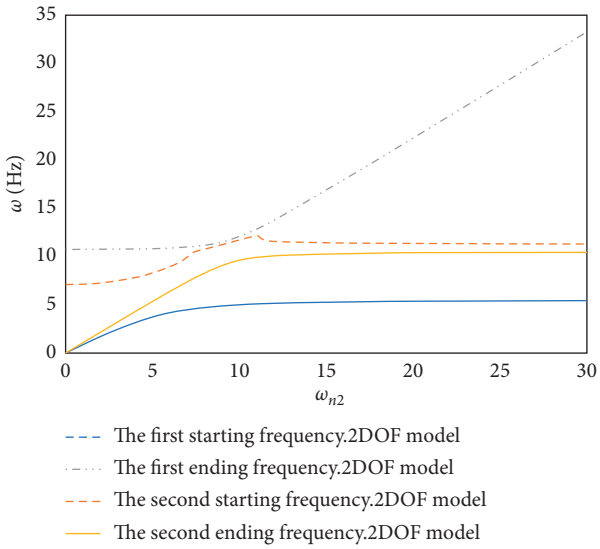

FIGURE 20: The effect of ω_{n2} parameter on bandgap for the 2DOF model.

uniform, although, in general, it becomes larger. Moreover, it should be pointed out that when the second local frequency increases, the second bandgap of the modified model is reduced.

5. Concluding Remarks

In this paper, at first, a new model of elastic metamaterials (1DOF model) involving a rack-and-pinion mechanism was presented. Then, by adding a concentrated mass, the model was modified by converting to a novel metastructure with multiple resonators in which more broadband bandgaps were produced. Different system parameters allow us to shift or expand the frequency ranges at which the system vibrations are reduced or eliminated by changing them. The influences of different system parameters on the bandgap intervals of the considered metamaterial are summarized as follows:

(i) By adding the concentrated mass and converting the model from 1DOF to 2DOF, two bandgaps are satisfactorily produced in the dynamics of the system

(ii) In the 1DOF model, in order to achieve the wider bandgap, in general, the dimensionless parameters $\widehat{I}$ and $\widehat{K}$should be increased or the dimensionless mass parameter M should be reduced

(iii) In the 2DOF model, the width of the first bandgap is enhanced by increasing the parameters $\overline{K}$, $\overline{I}$, $\overline{m}_1$, and ω_{n1} and decreasing ω_{n2}

(iv) In the 2DOF model, the width of the second bandgap is improved by increasing $\overline{I}$, ω_{n1}, and ω_{n2} or decreasing the parameter $\overline{m}_1$. No significant effect was demonstrated by varying the parameter $\overline{K}$

Data Availability

The data will be available upon request to the corresponding author.

Conflicts of Interest

The authors declare that they have no conflicts of interest.

Acknowledgments

H. M. Sedighi is grateful to the Research Council of Shahid Chamran University of Ahvaz for its financial support (Grant No. SCU.EM99.98).

References

[1] M. Gao, Z. Wu, and Z. Wen, "Effective negative mass nonlinear acoustic metamaterial with pure cubic oscillator," *Advances in Civil Engineering*, vol. 2018, Article ID 3081783, 15 pages, 2018.

[2] S. E. Mendhe and Y. P. Kosta, "Metamaterial properties and applications," *International Journal of Information Technology and Management*, vol. 4, no. 1, pp. 85–89, 2011.

[3] A. Valipour, M. H. Kargozarfard, M. Rakhshi, A. Yaghootian, and H. M. Sedighi, "Metamaterials and their applications: an overview," *Proceedings of the Institution of Mechanical Engineers, Part L: Journal of Materials: Design and Applications*, 2021.

[4] X. Zhou, J. Wang, R. Wang, and J. Lin, "Effects of relevant parameters on the bandgaps of acoustic metamaterials with multi-resonators multi-resonators," *Applied Physics A*, vol. 122, no. 4, pp. 1–8, 2016.

[5] H. Al Ba, D. DePauw, T. Singh, and M. Nouh, "Dispersion transitions and pole-zero characteristics of finite inertially amplified acoustic metamaterials," *Journal of Applied Physics*, vol. 123, pp. 1–12, 2018.

[6] S. Sang, "A new approach to generate local resonator for the application of acoustic metamaterials," *The Journal of the Acoustical Society of America*, vol. 142, 2017.

[7] H. H. Huang, C. T. Suna, and G. L. Huang, "On the negative effective mass density in acoustic metamaterials," *International Journal of Engineering Science*, vol. 47, no. 4, pp. 610–617, 2009.

[8] M. Nouh, O. Aldraihem, and A. Baz, "Metamaterial structures with periodic local resonances," *Health Monitoring of Structural and Biological Systems*, vol. 9064, pp. 1–11, 2014.

[9] A. H. Orta and C. Yilmaz, "Inertial amplification induced phononic band gaps generated by a compliant axial to rotary motion conversion mechanism," *Journal of Sound and Vibration*, vol. 439, pp. 329–343, 2019.

[10] B. S. Lazarov and J. S. Jensen, "Low-frequency band gaps in chains with attached non-linear oscillators," *International Journal of Non-Linear Mechanics*, vol. 42, no. 10, pp. 1186–1193, 2007.

[11] K. Wang, J. Zhou, D. Xu, and H. Ouyang, "Lower band gaps of longitudinal wave in a one-dimensional periodic rod by exploiting geometrical nonlinearity," *Mechanical Systems and Signal Processing*, vol. 124, pp. 664–678, 2019.

[12] J. S. Chen and I. Chien, "Dynamic behavior of a metamaterial beam with embedded membrane-mass structures," *Journal of Applied Mechanics*, vol. 84, no. 12, pp. 1–7, 2017.

[13] A. Casalotti, S. El-Borgi, and W. Lacarbonara, "Metamaterial beam with embedded nonlinear vibration absorbers," *International Journal of Non-Linear Mechanics*, vol. 98, pp. 32–42, 2018.

[14] X. Zhou, W. Jun, and R. Wang, "Band gaps in grid structure with periodic local resonator subsystems," *Modern Physics Letters B*, vol. 31, no. 25, 2017.

[15] G. L. Huang and C. T. Sun, "Band gaps in a multiresonator," *Journal of Vibration and Acoustics*, vol. 132, pp. 1–6, 2010.
[16] H. Sun, X. Du, and P. F. Pai, "Theory and experiment research of metamaterial beams for broadband vibration absorption," *Journal of Intelligent Material Systems and Structures*, vol. 21, no. 11, pp. 1085–1101, 2011.
[17] S. Xiao, T. Wang, T. Liu, C. Zhou, X. Jiang, and J. Zhang, "Active metamaterials and metadevices: a review," *Journal of Physics D: Applied Physics*, vol. 53, no. 50, Article ID 503002, 2020.
[18] Y. Y. Chen, M. V. Barnhart, J. K. Chen, G. K. Hu, C. T. Sun, and G. L. Huang, "Dissipative elastic metamaterials for broadband wave mitigation at subwavelength scale," *Composite Structures*, vol. 136, pp. 358–371, 2016.
[19] Z. Li, C. Wang, and X. Wang, "Modelling of elastic metamaterials with negative mass and modulus based on translational resonance," *International Journal of Solids and Structures*, vol. 162, pp. 271–284, 2019.
[20] A. H. Shirazi and H. M. Sedighi, "Physics of rack-and-pinion-inspired metamaterials with rotational resonators for broadband vibration suppression," *The European Physical Journal Plus*, vol. 135, no. 3, pp. 1–23, 2020.
[21] C. Comi and J.-J. Marigo, "Homogenization approach and bloch-floquet theory for band-gap prediction in 2D locally resonant metamaterials," *Journal of Elasticity*, vol. 139, no. 1, pp. 61–90, 2020.
[22] L. O'Faolain, "Photonic crystal cavities for optical interconnects," in *Optical Interconnects for Data Centers*, pp. 121–156, Woodhead Publishing, Cambridge, UK, 2016.

Hindawi
Advances in Condensed Matter Physics
Volume 2021, Article ID 9990673, 5 pages
https://doi.org/10.1155/2021/9990673

Research Article

Micropyramid Vertical Ultraviolet GaN/AlGaN Multiple Quantum Wells LEDs on Si(111)

Yuebo Liu,[1] **Honghui Liu**,[1] **Hang Yang**,[1] **Wanqing Yao**,[1] **Fengge Wang**,[1] **Yuan Ren**,[1] **Junyu Shen**,[1] **Minjie Zhang**,[1] **Zhisheng Wu**,[1,2] **Yang Liu**,[1,2] **and Baijun Zhang**[1,2]

[1]*State Key Laboratory of Optoelectronic Materials and Technologies, Sun Yat-sen University, Guangzhou 510275, China*
[2]*School of Electronics and Information Technology, Sun Yat-sen University, 510006 Guangzhou, China*

Correspondence should be addressed to Baijun Zhang; zhbaij@mail.sysu.edu.cn

Received 10 March 2021; Accepted 21 April 2021; Published 28 April 2021

Academic Editor: Shuyuan Xiao

Micropyramid vertical GaN-based ultraviolet (UV) light-emitting diodes (LEDs) on Si(111) substrate have been fabricated by selective area growth to reduce threading dislocations and the polarization effects. There is no-light emission at the bottom and six planes of the pyramid at lower current due to the leakage current and nonradiative recombination of the dislocation at the bottom and the 90° threading dislocations (TDs) at six planes of the pyramid, and the top of the pyramid is the high-brightness region. The micropyramid UV LED has a high optical output intensity under a small current injection, and the series resistance of unit area is only a quarter of the conventional vertical LEDs, so the micropyramid UV LED would have a high output power under the drive circuit. The reverse leakage current of a single micropyramid UV LED is 2 nA at −10 V.

1. Introduction

The III nitride-based light-emitting diodes (LEDs) have been paid extensive attention thanks to their potential applications such as solid-state lighting, communication, sterilization, disinfection, water or air purification, and biochemistry [1–7]. The GaN-based LEDs cover range the ultraviolet (UV), entire visible-light and near-infrared spectrum (6.2 eV ~ 0.7 eV), due to the different composition of indium or aluminium [2]. The marketization of GaN-based visible LEDs has been replaced by AlGaN UV LEDs as the next research hotspot. At present, heteroepitaxial technology is the adopted method for the fabrication of AlGaN UV LEDs by metal-organic chemical vapor deposition (MOCVD) system, but as a high-temperature heteroepitaxial method, it has problems of the lattice and thermal mismatch [2, 8, 9]. The high density of threading dislocations (TDs) in epitaxial layer is attributed to the material parameters step in interface [10]. Nonradiative recombination centers in TDs reduce the internal quantum efficiency (IQE), which evolves into thermal centers of damage the UV LEDs [8]. For lower TDs, two-step growth processes of predeposition AlN/AlGaN and selective area growth (SAG) were proposed [10]. Due to developments in crystal growth, chip processing, and packaging technologies, the external quantum efficiency (EQE) of NUV-LEDs of 365 nm, 385 nm, and 405 nm reaches 30%, 50%, and 60%, respectively [6]. However, the polarization effect of spacial separation of electron-hole wave function also greatly affects the IQE of LEDs [11]. The nonpolar plane reduces quantum-confined Stark effect (QCSE) from the spontaneous and piezoelectric polarization [12, 13]. Zhao et al. achieved IQE as high as 39% at 279 nm in a-plane AlGaN-based multiple quantum wells (MQWs) [14]. With the rapid development of crystal growth and the improvement of semiconductor manufacturing processes, micropyramid GaN-based UV LEDs on Si (111) can improve the EQE by SAG, which is ascribed to (1) high GaN crystal quality of lateral-growth [15], (2) semipolar plane of pyramid structure [12], and (3) larger emitting area of six planes of the pyramid. However, its related research work is rarely reported, especially single electrically driven GaN-based UV LED.

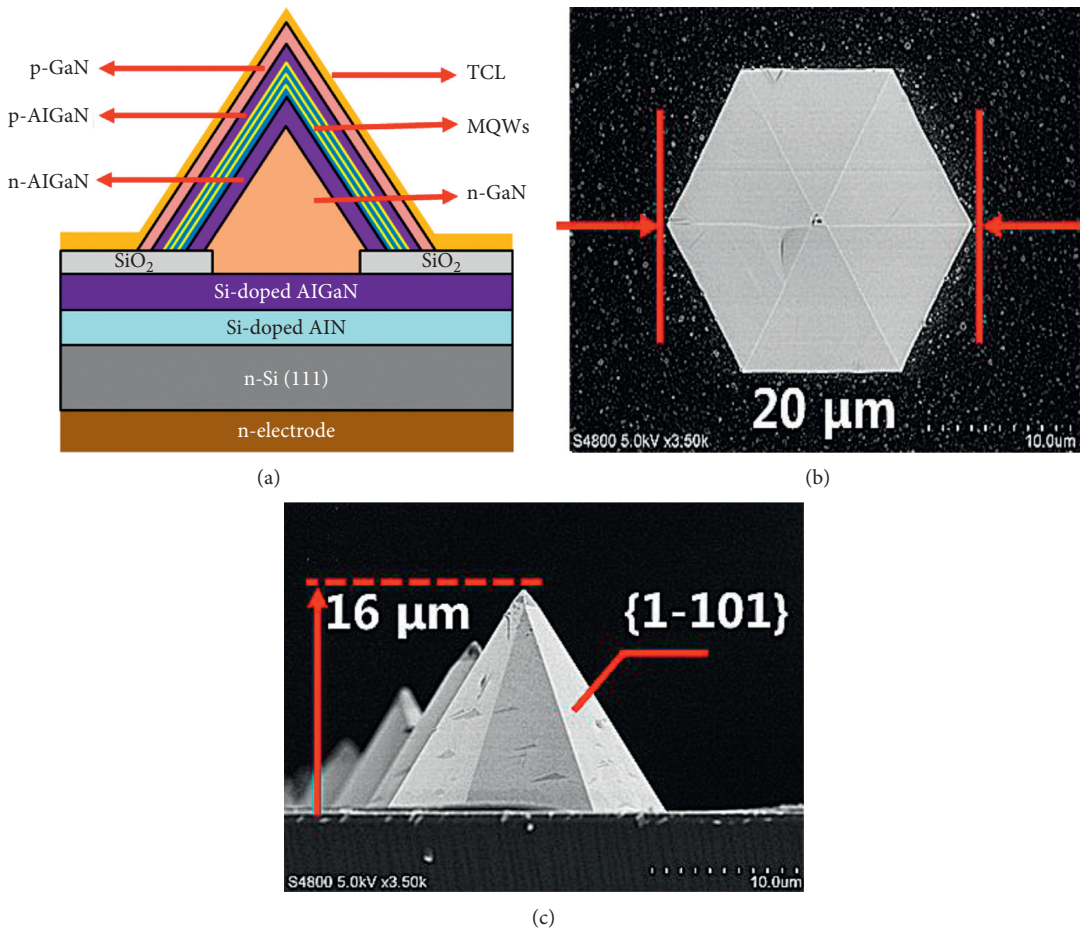

Figure 1: (a) Schematic diagram of the structure. (b) Top view and (c) front view SEM images of micropyramid UV LED of no-electrode.

Hence, in this work, micropyramid vertical GaN-based UV LED on Si (111) substrate has been fabricated by selective area growth. Six semipolar planes at the top of the pyramid greatly improve EQE due to lower the TDs and the lower polarization effects. The micropyramid UV LED has a high optical output intensity under a small current injection, and the series resistance of unit area is only a quarter of the conventional vertical LEDs. With features such as these, the micropyramid UV LED can be used as a subminiature UV light source, and it would have a high output power. The reverse leakage current of single electrically driven micropyramid UV LED is 2 nA at −10 V. The top of the micropyramid vertical GaN-based UV LED is a high-brightness region. However, the planes and bottom of the pyramid do not emit light due to leakage current, nonradiative recombination of the dislocation at the bottom, and the 90° TDs at six planes of the pyramid.

2. Experiments

Micropyramid UV LED growth was performed on 2 inch Si(111) by SAG in a low-pressure MOCVD system. Vertical structure was designed to reduce current crowding, as shown in Figure 1(a). The resistivity of n-type Si is less than 0.02 Ω·cm. Before epitaxial growth, to remove impurities and oxides on the Si(111) plane, the n-type Si was sequentially cleaned with $H_2SO_4 : H_2O_2 : H_2O = 3 : 1 : 1$, acetone solution, and isopropyl alcohol solution, respectively. A ~50/1000 nm thick n-AlGaN/AlN : Si film was grown on the Si substrate at 1095°C. Subsequently, a 100 nm thick amorphous SiO_2 layer was deposited on the AlGaN/AlN/Si by plasma-enhanced chemical vapor deposition (PECVD). Afterward, the mask of SiO_2 of 5.0-μm-diameter window openings with a 60 μm period was designed by wet-etching ($HF : H_2O = 1 : 10$). After cleaning, SiO_2/AlGaN/AlN/Si was again used in epitaxial grown for n-type GaN-based micropyramid. The growth of GaN in the SAG of the window area belonged in secondary epitaxy, and the GaN rapidly grew on the window since the window of the patterned SiO_2 mask exposes the AlGaN layer. Ga atoms did not stay on the amorphous SiO_2 mask due to high-temperature decomposition of Ga-O and the larger nucleation energy of heteroepitaxy. However, Ga atoms migrated laterally to the window area for lateral growth, eventually healed into a point on top and formed the n-type GaN-based pyramid structure. Three pairs of AlGaN/GaN MQWs were grown on the six semipolar planes $\{1\bar{1}01\}$ of the pyramid, and then the p-type AlGaN/GaN : Mg was grown. The elements of Ga, Al, and N were provided by trimethyl-gallium (TMGa) or triethyl-gallium (TEGa), trimethyl-aluminum (TMAl), and ammonia (NH_3), respectively.

Table 1: The growth condition of the micropyramid LED in window areas.

	TMGa (sccm)	TMAl (sccm)	TEGa (sccm)	Pressure (mBar)	Temperature (°C)	Time (min)
n-GaN	40	—	—	300	1095	20
n-AlGaN	40	10	—	100	1100	10
AlGaN barrier	—	10	170	200	880	5
GaN well	—	—	340	200	800	2
p-AlGaN	—	10	210	200	980	8
p-GaN	—	—	210	200	980	4

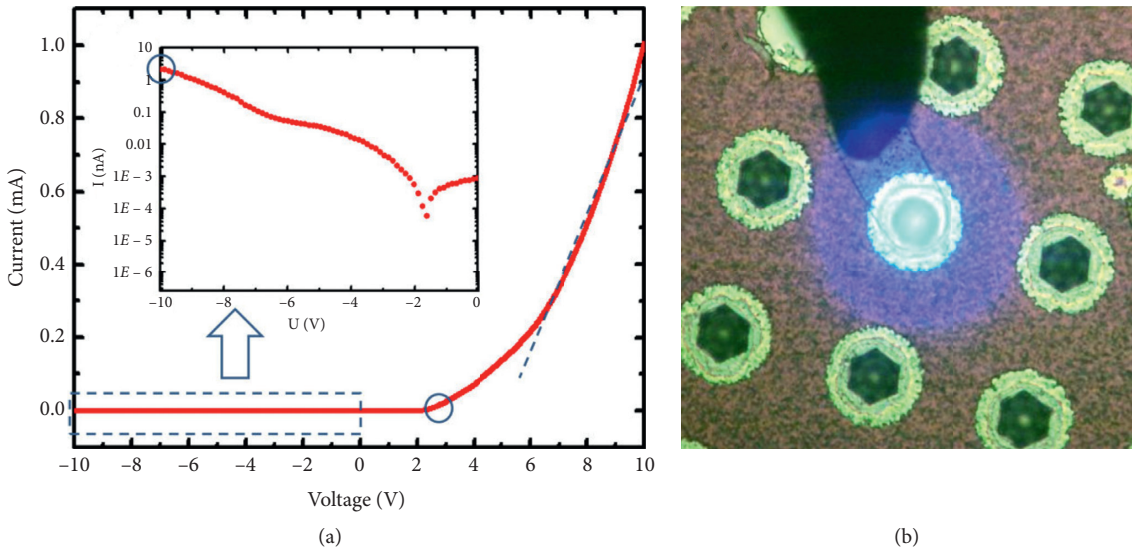

Figure 2: (a) I-V curve and (b) optical microscope photograph of micropyramid UV LED.

The detailed growth condition of the micropyramid LED in window areas are shown in Table 1.

The scanning electron microscopy (SEM) images of Figures 1(b) and 1(c) showed that the micropyramid of six semipolar planes were symmetrical and smooth. The bottom diameter (20 μm) of the micropyramid was much larger than the window of the mask due to the lateral growth. The angle between $\{1\bar{1}01\}$ and (0001) crystal plane was 62°. A 250 nm thick indium tin oxide (ITO) film was deposited on the micropyramid LED as a transparent conducting layer (TCL), followed by the thermal annealing at 550°C for 30 min in nitrogen (N_2) environment. A Ti/AuSb/Au (10 nm/20 nm/200 nm) metal was stacked on n-type Si by E-beam evaporation and rapid thermal annealing at 380°C for 35 seconds in nitrogen (N_2) environment. More detailed structure is shown in Figure 1(a). In this way, the single electrically driven micropyramid vertical GaN-based UV LED was manufactured.

3. Results and Discussion

In order to study the electrical performance of micropyramid UV LED, the current-voltage (I-V) characteristic has been measured by Agilent B1500A, and the I-V curve is shown in Figure 2(a). The curve shows the I-V characteristic of a typical p-n junction due to the micropyramidal n-GaN/n-AlGaN and p-AlGaN/p-GaN layers. The turn-on voltage and series resistance are ~2.5 V and $5.2 \times 10^3\ \Omega$, respectively. Series resistance of unit area is only a quarter of vertical LEDs [16]. This attribution virtually leads to the high optical output power. The doping in growth and high-quality ohmic contact results in a low resistance. The reverse leakage current of micropyramid UV LED is 2 nA at −10 V. There are few reverse leakage current channels in micropyramid UV LEDs because the micropyramid n-GaN releases partial stress from the lattice mismatch and the dislocation density is low. The working photograph is shown in Figure 2(b), and the single micropyramid UV LED is located at the centre of the high brightness region.

Figure 3 shows the electroluminescence (EL) spectra of micropyramid UV LED working at various currents from 2 to 7 mA. The micropyramid UV LED has a high optical output intensity under a small current injection.

Under positive bias, electrons cross the AlGaN/GaN MQWs layer and recombine with holes in the p-GaN layer by radiative recombination. The EL curves show 365 nm and 386 nm emission peaks, which come from the emission of the GaN/AlGaN MQWs and the p-GaN layer [8], respectively. The peak of 386 nm is higher than the peak of 365 nm because the Al composition in the barrier of $Al_{0.06}Ga_{0.94}N$/GaN MQWs is low and the p-GaN can absorb the 365 nm light [17].

The inset of Figure 3 shows the optical microscope photograph of the micropyramid UV LED when the injection current is 0.2 mA and 2 mA, respectively. The light of

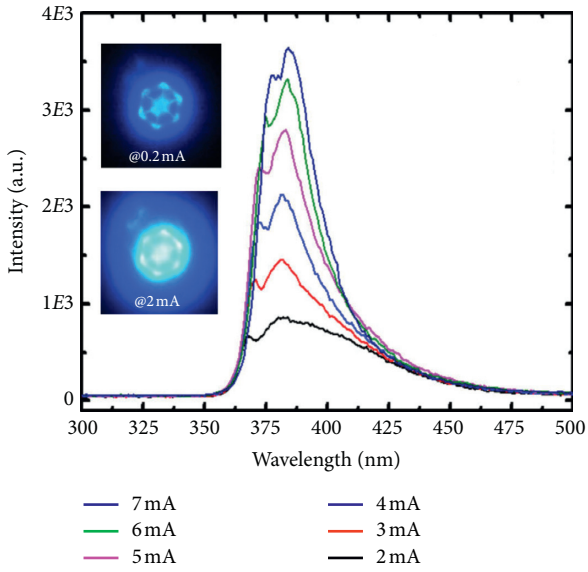

Figure 3: EL spectra of micropyramid UV LED working at various currents from 2 to 7 mA.

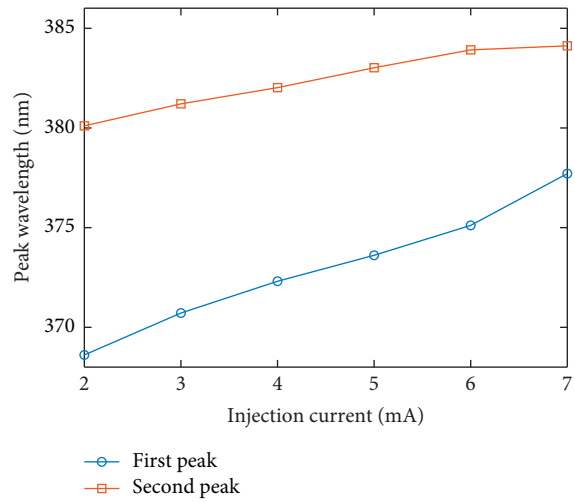

Figure 4: The relation between the positions of the first and second peaks and the injection current.

the micropyramid UV LED distributes on the top, six bottom corner and edges due to the high radiation recombination efficiency at the top of the pyramid [18–20]. The top of the pyramid is a high-brightness region due to the lower TDs, and the lower polarization effects and the larger emitting area of six semipolar planes. However, the bottom and six planes of the pyramid do not emit light at a low current due to the nonradiative recombination of the dislocation at the bottom and the 90° TDs at six planes of the pyramid. The light at the bottom and the six edges come from the emission of the top by waveguide of pyramid structure [21, 22]. As the injection current increases, the emission of top gradually spreads to the bottom.

In the EL spectra of micropyramid UV-LED, as shown in Figure 3, the peaks of the wavelengths of 365 nm and 386 nm show a red shift with increasing the injecting current. For an easier reference, the peak near the 365 nm and 386 nm is named as the first peak and the second peak, respectively. The relation between the peak positions and the injection current has been shown in Figure 4.

As shown in Figure 4, the wavelengths of two peaks increase with the strength of the injection current due to the heat effect of electric current.

In the temperature range of 200–800 K, the band gap of GaN can be expressed by the Varshni equation as follows [23, 24].

$$E_g(T) = E_g(0K) - \frac{\alpha T^2}{\beta + T}, \quad (1)$$

where $E_g(0\,K) = 3.495$ eV is the band gap of GaN at $T = 0\,K$; $\alpha = 0.94$ me V/K is the empirical constant; and $\beta = 791$ K is associated with the Debye temperature [24]. Equation (1) indicates the heat effect of electric current would result in the decrease of the band gap, which results in the red shift of the peaks in the EL spectra.

On the other hand, the state density of conduction band and the Fermi level increases with the strength of the injection current, and it would lead to the blue shift of the peaks in the EL spectra. The combined action of the two factors brings about the red shift of the peaks of the wavelengths of 365 nm and 386 nm.

4. Conclusion

In summary, micropyramid vertical GaN-based UV LED was fabricated on 2-inch n-Si (111) by SAG in a low-pressure MOCVD system. The top of the pyramid is the high-brightness region due to the lower TDs, the lower polarization effects, and the larger emitting area of six semipolar planes. However, no-light emission comes from the bottom and six planes of the pyramid at a low current due to the leakage current and nonradiative recombination of the dislocation at the bottom and the 90° TDs on six planes of the pyramid. The turn-on voltage, series resistance, and reverse leakage current of the single micropyramid UV LED are ~2.5 V, $5.2 \times 10^3\,\Omega$, and 2 nA at −10 V, respectively. The series resistance of unit area is only a quarter of the conventional vertical LEDs, and the micropyramid UV LED has a high optical output intensity under a small current injection. It means the micropyramid UV LED can be used as a subminiature UV light source, and it would have a high output power under a small current injection. In addition, the reason why the peaks of the wavelengths of 365 nm and 386 nm in the EL spectra show a red shift with increasing the injecting current has been explained.

Data Availability

The data used to support the findings of this study are available from the corresponding author upon request.

Conflicts of Interest

The authors declare that they have no conflicts of interest.

Acknowledgments

The work was partially supported by the Key-Area Research and Development Program of Guangdong Province, China (Grant nos. 2019B010132001 and 2019B010132003), the joint funding of the Nature Science Foundation of China (NSFC) and the Macao Science and Technology Development Fund (FDCT) of China (Grant no. 62061160368), the National Key Research and Development Program (Grant nos. 2016YFB0400105 and 2017YFB0403001), and the Zhuhai Key Technology Laboratory of Wide Bandgap Semiconductor Power Electronics, Sun Yat-sen University, China (Grant no. 20167612042080001).

References

[1] F. A. Ponce and D. P. Bour, "Nitride-based semiconductors for blue and green light-emitting devices," *Nature*, vol. 386, no. 6623, pp. 351–359, 1997.

[2] I. Vurgaftman, J. R. Meyer, and L. R. Ram-Mohan, "Band parameters for III-V compound semiconductors and their alloys," *Journal of Applied Physics*, vol. 89, no. 11, pp. 5815–5875, 2001.

[3] Y. Li, W. Wang, L. Huang et al., "High-performance vertical GaN-based near-ultraviolet light-emitting diodes on Si substrates," *Journal of Materials Chemistry C*, vol. 6, no. 42, pp. 11255–11260, 2018.

[4] J.-T. Oh, Y.-T. Moon, D.-S. Kang et al., "High efficiency ultraviolet GaN-based vertical light emitting diodes on 6-inch sapphire substrate using ex-situ sputtered AlN nucleation layer," *Optics Express*, vol. 26, no. 5, pp. 5111–5117, 2018.

[5] C. C. Li, J. L. Zhan, Z. Z. Chen et al., "Operating behavior of micro-LEDs on a GaN substrate at ultrahigh injection current densities," *Optics Express*, vol. 27, no. 16, pp. A1146–A1155, 2019.

[6] Y. Muramoto, M. Kimura, and S. Nouda, "Development and future of ultraviolet light-emitting diodes: UV-LED will replace the UV lamp," *Semiconductor Science and Technology*, vol. 29, no. 8, p. 084004, 2014.

[7] S. Xiao, T. Wang, T. Liu, C. Zhou, X. Jiang, and J. Zhang, "Active metamaterials and metadevices: a review," *Journal of Physics D: Applied Physics*, vol. 53, no. 50, p. 503002, 2020.

[8] M. A. Reshchikov and H. Morkǫ, "Luminescence properties of defects in GaN," *Journal of Applied Physics*, vol. 97, no. 6, p. 061301, 2005.

[9] D. Zubia and S. D. Hersee, "Nanoheteroepitaxy: the Application of nanostructuring and substrate compliance to the heteroepitaxy of mismatched semiconductor materials," *Journal of Applied Physics*, vol. 85, no. 9, pp. 6492–6496, 1999.

[10] H. Amano, N. Sawaki, I. Akasaki, and Y. Toyoda, "Metalorganic vapor phase epitaxial growth of a high quality GaN film using an AlN buffer layer," *Applied Physics Letters*, vol. 48, no. 5, pp. 353–355, 1986.

[11] H. P. Zhao, G. Y. Liu, J. Zhang, J. D. Poplawsky, V. Dierolf, and N. Tansu, "Approaches for high internal quantum efficiency green InGaN light-emitting diodes with large overlap quantum wells," *Optics Express*, vol. 19, no. 14, pp. A991–A1007, 2011.

[12] J. H. Ryou, P. D. Yoder, J. P. Liu et al., "Control of quantum-confined Stark effect in InGaN-based quantum wells," *IEEE Journal of Selected Topics in Quantum Electronics*, vol. 15, no. 4, pp. 1080–1091, 2009.

[13] E. T. Yu, X. Z. Dang, P. M. Asbeck, S. S. Lau, and G. J. Sullivan, "Spontaneous and piezoelectric polarization effects in III-V nitride heterostructures," *Journal of Vacuum Science & Technology B: Microelectronics and Nanometer Structures*, vol. 17, no. 4, pp. 1742–1749, 1999.

[14] J. Zhao, X. Zhang, J. He et al., "High internal quantum efficiency of nonpolar a-plane AlGaN-based multiple quantum wells grown on r-plane sapphire substrate," *ACS Photonics*, vol. 5, no. 5, pp. 1903–1906, 2018.

[15] S. Tanaka, Y. Kawaguchi, N. Sawaki, M. Hibino, and K. Hiramatsu, "Defect structure in selective area growth GaN pyramid on (111)Si substrate," *Applied Physics Letters*, vol. 76, no. 19, pp. 2701–2703, 2000.

[16] Y. B. Yang, Y. Lin, P. Xiang et al., "Vertical-conducting InGaN/GaN multiple quantum wells LEDs with AlN/GaN distributed Bragg reflectors on Si(111) substrate," *Applied Physics Express*, vol. 7, no. 4, p. 042102, 2014.

[17] N. Otsuka, A. Tsujimura, Y. Hasegawa, G. Sugahara, M. Kume, and Y. Ban, "Room temperature 339 nm emission from Al0.13Ga0.87N/Al0.10Ga0.90N double heterostructure light-emitting diode on sapphire substrate," *Japanese Journal of Applied Physics*, vol. 39, no. 5B, pp. L445–L448, 2000.

[18] B. Monemar, P. P. Paskov, J. P. Bergman et al., "Recombination of free and bound excitons in GaN," *Physica Status Solidi B*, vol. 245, no. 9, pp. 1723–1740, 2008.

[19] L. Liu, L. Wang, C. Lu et al., "Enhancement of light-emission efficiency of ultraviolet InGaN/GaN multiple quantum well light emitting diode with InGaN underlying layer," *Applied Physics A*, vol. 108, no. 4, pp. 771–776, 2012.

[20] A. E. Chernyakova, M. M. Soboleva, V. V. Ratnikova, N. M. Shmidta, and E. B. Yakimov, "Nonradiative recombination dynamics in InGaN/GaN LED defect system," *Superlattices & Microstructures*, vol. 45, no. 4-5, pp. 301–307, 2009.

[21] H. X. Jiang, J. Y. Lin, K. C. Zeng, and W. Yang, "Optical resonance modes in GaN pyramid microcavities," *Applied Physics Letters*, vol. 75, no. 6, pp. 763–765, 1999.

[22] A. David, C. Meier, R. Sharma et al., "Photonic bands in two-dimensionally patterned multimode GaN waveguides for light extraction," *Applied Physics Letters*, vol. 87, no. 10, p. 101107, 2005.

[23] N. M. Ravindra and V. K. Srivastava, "Temperature dependence of the energy gap in semiconductors," *Journal of Physics and Chemistry of Solids*, vol. 40, no. 10, pp. 791–793, 1979.

[24] N. Nepal, J. Li, M. L. Nakarmi, J. Y. Lin, and H. X. Jiang, "Temperature and compositional dependence of the energy band gap of AlGaN alloys," *Applied Physics Letters*, vol. 87, no. 24, p. 242104, 2005.